



UNIVERSITÀ  
DEGLI STUDI DI TRIESTE

XXIX CICLO DEL  
DOTTORATO DI RICERCA IN  
**NANOTECNOLOGIE**

SINGLE-LAYER GRAPHENE FOR BIOLOGY  
AND CHEMISTRY: FABRICATION AND  
APPLICATIONS

Settore Scientifico Disciplinare: FIS/03

**DOTTORANDA:**

Alessia Matruglio

*Alessia Matruglio*

**COORDINATORE:**

Lucia Pasquato

*Lucia Pasquato*

**SUPERVISORE DI TESI:**

Marco Lazzarino

*Marco Lazzarino*

**TUTOR:**

Simone Dal Zilio

*Simone Dal Zilio*

ANNO ACCADEMICO: 2015-2016



# Abstract

The huge graphene boom of the last decade led to its use in a very large number of application in different fields. In this thesis I explore single layer graphene properties to develop two main applications in chemistry and biology. First, the attention will be focused on graphene cleanness. A novel graphene transfer method, using graphene on copper grown via chemical vapour deposition, is developed. This involves the use of a thin titanium layer as graphene support during its transfer from the metal on the final substrate instead the common used polymer, avoiding residuals and contaminations.

Secondly, single layer graphene was used to fabricate sealed cell for liquid investigation. Graphene nanobubbles filled with water were fabricated on a  $\text{TiO}_2$  substrate and used for liquid analysis with different techniques, such as electron microscopy, Raman spectroscopy, and, more interesting, x-ray electron spectroscopy in ultra-high vacuum conditions. These sealed graphene liquid cells were used to follow two chemical reactions, the thermal-induced iron reduction in a  $\text{FeCl}_3$  solution and the photon-induced iron reduction in liquid Prussian Blue.

In the last part, a biological application will be presented; this involve the use of supported and suspended single layer graphene for rat hippocampal neuronal cells growth, demonstrating the big potential of this material for neuronal interfaces.



# Table of Contents

Introduction .....	9
--------------------	---

## Chapter 1

1.1 The discovery of graphene .....	11
1.2 Graphene structure.....	11
1.3 Graphene properties: the “wonder material” .....	13
1.3.1 Graphene impermeability .....	14
1.4 Synthesis methods .....	15
1.4.1 Mechanical exfoliation .....	16
1.4.2 Liquid phase exfoliation.....	17
1.4.3 Chemical Vapour Deposition .....	18
1.4.4 Epitaxial growth .....	20
1.5 Applications.....	21
1.5.1 Graphene field-effect transistors .....	21
1.5.2 Graphene FET for biosensing .....	24
1.5.3 Graphene for transparent membranes .....	25
1.5.4 Graphene for transparent and flexible electronics .....	26
1.5.5 Photovoltaic devices .....	27
1.5.6 Bioapplications .....	28
1.5.7 Patterning of graphene .....	29
1.6 Graphene transfer.....	32
1.6.1 Transfer by mechanical exfoliation.....	32
1.6.2 Wet transfer techniques .....	34
1.6.3 Dry transfer techniques .....	37
References .....	40

## Chapter 2

2.1 Residuals in graphene wet-transferred with polymers.....	49
--	----

2.2	A novel wet transfer method using titanium for polymer-free transfer .....	51
2.2.1	Fabrication of the samples .....	52
2.2.2	Characterization of the samples .....	58
2.2.3	Analysis of the metal residuals after titanium removal .....	64
2.2.4	Electrical characterization .....	68
	References.....	71

## Chapter 3

3.1	Transparent graphene membranes for ultra-high vacuum experiments in liquid.....	76
3.2	Graphene nanobubbles for transparent liquid cells .....	78
3.3	Graphene nanobubbles on TiO <sub>2</sub> for in situ electron spectroscopy of water.....	80
3.3.1	Fabrication of graphene nanobubbles.....	80
3.3.2	Characterization of graphene nanobubbles.....	83
3.3.3	Ultra-high vacuum measurements on graphene nanobubbles.....	87
3.4	Advantage in the use of graphene nanobubbles for in situ UHV analysis .....	92
	References.....	93

## Chapter 4

4.1	Graphene nanobubbles on TiO <sub>2</sub> for in situ electron spectroscopy of liquid-phase chemical reactions .....	98
4.2	In situ study of liquid-phase thermal reduction of FeCl <sub>3</sub> solution.....	99
4.2.1	Sample preparation .....	99
4.2.2	X-ray electron spectroscopy of FeCl <sub>3</sub> solution in graphene nanobubbles .....	100
4.2.3	X-ray electron spectroscopy of Fe reduction inside graphene nanobubbles .....	102
4.3	In situ study of liquid-phase UV reduction of Prussian Blue.....	106
4.3.1	Sample preparation .....	107
4.3.2	Photoreduction of Prussian Blue inside graphene nanobubbles .....	110
	References.....	118

## Chapter 5

5.1	Graphene nanostructures as neuronal interfaces.....	122
5.2	Growth of neuronal cells on supported and suspended graphene .....	123
5.2.1	Fabrication of the substrates .....	124
5.2.2	Neuronal cultures.....	126
5.2.3	Morphology of neuronal cells on different substrates: SEM characterization .....	127
5.2.4	Immunofluorescence experiments .....	129
5.2.5	Electrophysiology.....	133
	References .....	136

	Conclusions and outlook.....	139
--	------------------------------	-----

	Appendix.....	143
--	---------------	-----

1.	A novel approach in the free-electron laser diagnosis based on a pixelated phosphor detector.....	144
2.	Toward an integrated device for spatiotemporal superposition of free-electron lasers and laser pulses .....	153

	Contributions to international conferences .....	161
--	--	-----

	Accepted Beamtimes .....	162
--	--------------------------	-----

	List of publications .....	163
--	----------------------------	-----





# Introduction

George Beylerian, the founder and current head of Material ConneXion, a global materials supplier to designers and industry, which hosts one of the largest physical libraries of advanced materials in the world, once said “The world seems to expect a never-ending supply of new material option”.

Since prehistoric times, materials have played a key role in the development of society. In the Stone Age, the progress was determined by the availability of materials, like wood and stone, able to foster technological innovations. At the end of the eighteenth century, the development of new materials, such as steel, has resulted in the creation of structures impossible to achieve before. If earlier the introduction of new technologies was determined by the availability of existing materials, in the last centuries there has been a change of direction: new materials with desired physical and chemical properties were developed thanks a continuous improvement of the scientific knowledge.

The discovery of graphene in 2004 is leading to the explosion of a new era, immediately recognized by the Nobel prize committee who awarded the prize in 2010 to Andre Geim and Konstantin Novoselov, who isolated the first monolayer of graphene exfoliating a piece of graphite. Much has been done so far, but still negligible compared to the great potential of this material.

This thesis analyzes the key aspects of this amazing material, and exhibits some innovative applications in the chemical and biological field. In particular, the Chapter 1 is an overview of properties, application and synthesis method, up to the description of the main transfer methods which represent the “bridge” between graphene production and applications. The Chapter 2 analyzes the problem of contaminants common to transfer methods involving the use of a polymer; it presents an alternative method that I developed at IOM-CNR laboratory in Trieste which involves the use of a titanium sacrificial layer instead of polymer; the method demonstrates the achievement of a clean and efficient transfer technique suitable for supported and suspended graphene. The Chapter 3 analyzes the great impact of graphene in transparent membrane, describing a novel type of graphene liquid cell obtained with nanobubbles containing water between graphene and a TiO<sub>2</sub> substrate; the Chapter shows the possibility to use this nanobubbles as cell for *in situ* electron spectroscopy of liquid in

ultra-high vacuum conditions. The Chapter 4 presents the same cells for the analysis and monitoring of two chemical reactions: the thermal reduction of Fe in  $\text{FeCl}_3$  solution, and the photoreduction of  $\text{Fe}_7(\text{CN})_{18}$  promoted by UV light. The reactions are studied using x-rays photoelectron spectroscopy and other techniques, demonstrating the possibility to use the nanobubbles as cells to follow chemical reactions for *in situ* electron spectroscopy in ultra-high vacuum. Finally, the Chapter 5 shows the use of clean graphene for a biological application: the possibility to grow primary hippocampal neurons of suspended graphene is discussed, and the increased results of neuronal activity compared to controls or to supported graphene are shown.

To conclude, the appendix reports two different works carried out in parallel and in collaboration with FERMI at Elettra in the field of x-ray free electron laser: they involve the development and fabrication of a pixelated phosphor detector for the precise characterization of the free-electron laser beam, and another device for the simultaneous characterization and fast spatial and temporal overlapping of two beams in the pump and probe experiments.

# Chapter 1

## 1.1 The discovery of graphene

The first graphene flake has been isolated in 2004 by Andre Geim and Konstantin Novoselov in the University of Manchester [1]. They exfoliated a piece of graphite using an ordinary adhesive tape, and isolated a single graphene sheet depositing it on a SiO<sub>2</sub>/Si substrate. They fabricated a field effect transistor (FET) with graphene as channel which could be switched between 2D electron and hole gases by changing the gate voltage. The graphene discovery and its characterization led to the assignment of the Nobel Prize in Physics in 2010 to Geim and Novoselov and opened the way to a great line of study that still continues today.

## 1.2 Graphene structure

Graphene is a single layer of carbon atoms arranged in a honeycomb structure. Carbon has four valence electrons, three of which are  $sp^2$  hybridized and participate in  $\sigma$ -bonding with their neighbors; these bonds maintain the interatomic distance of 0.142 nm and are responsible of graphene mechanical properties. The fourth electron occupies the not completely filled  $p_z$  orbital perpendicular to the one dimensional sheet, creating a delocalized  $\pi$ -bonding and is responsible of the weaker interplane interaction in graphite. When only a single plane exists, these electrons are delocalized on the full plane and are responsible of the electron conduction properties of graphene. A cartoon of the honeycomb structure and atoms bonding is shown in Fig. 1.1.

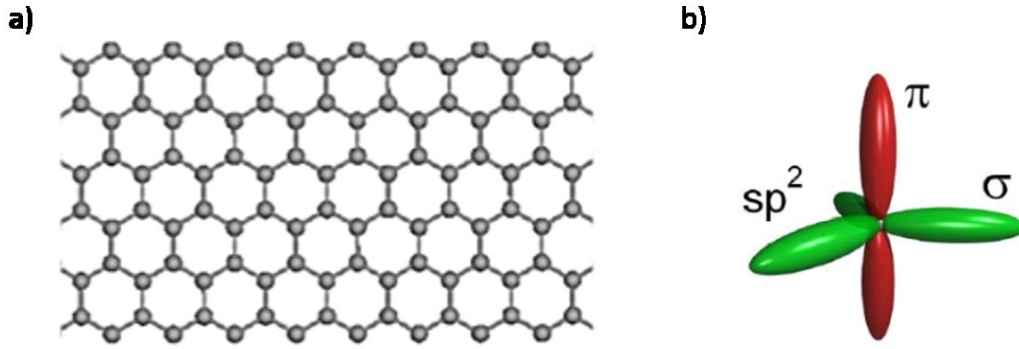


Fig 1.1: a) honeycomb structure of graphene lattice; b) scheme of the  $\sigma$ -bonding and  $\pi$ -bonding of the carbon atoms [2].

The atoms of graphene structure do not correspond to the points of a Bravais lattice; the primitive cell can be combined by two triangular sublattices, indicated in Fig. 1.2a and labelled “A” in blue (Fig. 1.2a) and “B” in yellow (Fig. 1.2b). The lattice vectors are defined by the (1.1):

$$a_1 = \frac{a}{2}(3, \sqrt{3}), \quad a_2 = \frac{a}{2}(3, -\sqrt{3}) \quad (1.1)$$

Where  $a = 1.42 \text{ \AA}$  is the length of graphene C-C bond. Fig. 1.2b shows the cell in the reciprocal space, in which vectors are described by the (1.2):

$$b_1 = \frac{2\pi}{3a}(1, \sqrt{3}), \quad b_2 = \frac{2\pi}{3a}(1, -\sqrt{3}) \quad (1.2)$$

The point indicated as  $\Gamma$ , M, K and K' are the center, edge and corners of the Brillouin zone, respectively.

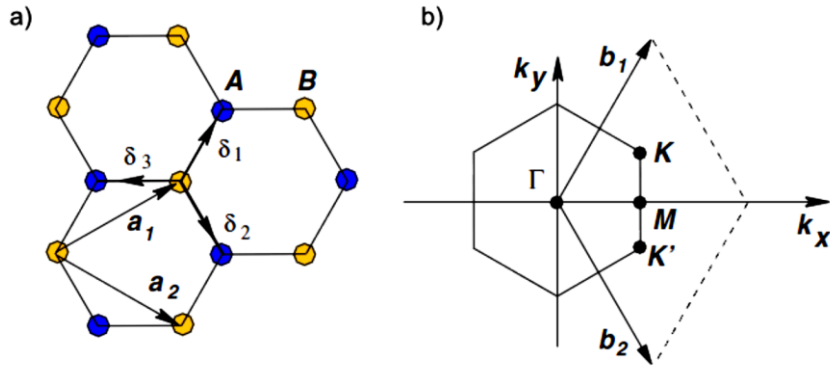


Fig. 1.2: a) The graphene lattice [3]. A and B are the two sublattices with vectors  $a_1$  and  $a_2$  and three nearest neighbors  $\delta_1$ ,  $\delta_2$ ,  $\delta_3$ ; b) reciprocal space with vectors  $b_1$  and  $b_2$ .

### 1.3 Graphene properties: the “wonder material”

Since the isolation of the first flake, graphene has attracted great interest because of its unique properties. It is called “the wonder material” for its supreme characteristics. First of all, presents very high room-temperature electron mobility, equal to  $2.5 \times 10^5 \text{ cm}^2 \text{ V}^{-1} \text{ s}^{-1}$  (100 times higher than silicon) [3]. These remarkable electronic properties derive from the graphene band structure: it is a zero bandgap semiconductor with two linearly dispersing bands that touch in six points of two different equivalences K and K', the so-called Dirac points. These points are the corners of the first Brillouin zone, as shown in Fig. 1.3.

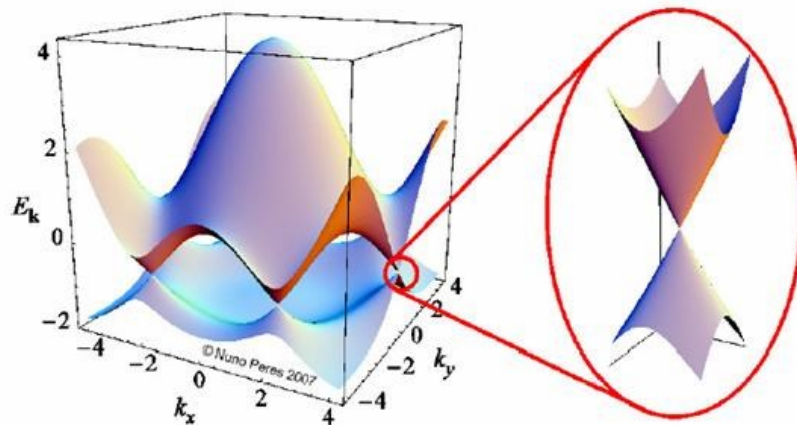


Fig. 1.3: electronic dispersion in the honeycomb lattice. The zoom indicate the energy bands close to one of the Dirac points [3].

The energy dispersion close to the Dirac points is linear with the momentum and can be described from the equation (1.3):

$$E = \hbar k v_F \quad (1.3)$$

Where  $k$  is the wave vector and  $v_F$  is Fermi velocity equal to  $v_F \approx c/300$ , ( $c$  is the velocity of light in vacuum). Electrons and holes have zero effective mass close to the Dirac points and their speed is higher than all known materials ( $10^6$  m/s) with a carrier charge density of  $10^{13} \text{cm}^{-2}$  [1]. This is the reason of the graphene extremely impressive high mobility. As already discussed, since graphene monolayer exhibits a linear dispersion, half-integer quantum Hall effect is observed [4], instead of the integer one, that is usually observed in 2D materials. This is due to graphene quasiparticles which behave as massless Dirac fermions and there is a zero energetic state.

Graphene  $\sigma$  orbitals form a strong bond and give great stability to the structure. For this reason, some interesting mechanical properties are present, such as the Young's modulus close to 1 TPa (the strongest material ever discovered) [4], and an intrinsic strength of 130 GPa (compared to 400 MPa for A26 structural steel or 375 MPa for Kevlar) [5].

Moreover, graphene presents other impressive properties, such as high thermal conductivity equal to  $3000 \text{ WmK}^{-1}$  (10 times higher than copper) [6], impermeability to liquid and gas [7], optical absorption coefficient of 2.3% (50 times higher than gallium arsenide) [8], chemical stability [9], super flexibility [10] and biocompatibility [11].

### 1.3.1 Graphene impermeability

Graphene is impermeable to all molecules and gases. In fact, graphene's  $\pi$ -orbitals form a dense, delocalized electronic cloud that screens the gap within its aromatic rings. Berry's theoretical calculation [12] indicated that there are no holes in the electron-density inside the aromatic rings to allow molecules to pass. If the actual electronic radius of the carbon atoms is considered, the geometric pore size of graphene would decrease from 0.246 to 0.064 nm, which is smaller than the diameter of the smaller molecules like helium (0.28 nm) and hydrogen (0.314 nm) [12]. Fig. 1.4 shows a scheme of the geometric pore of graphene.

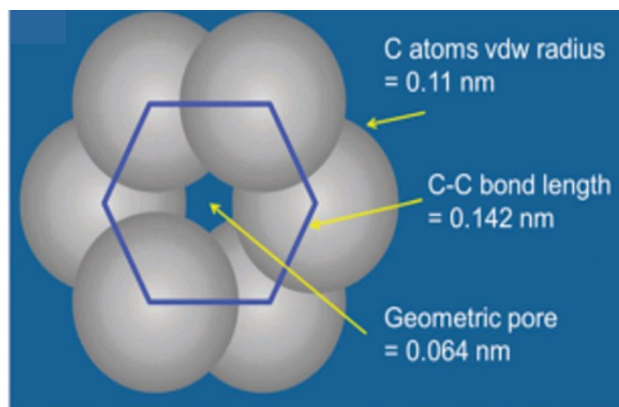


Fig. 1.4: theoretical calculation of geometric pore of graphene, vdw: Van der Waals [12].

It was demonstrated that impermeable graphene on mica can trap crystalline adlayers of water at room temperature, and this allows the measurements of the size of these adlayers on mica surface [13]. In the experimental Chapter 4 and 5, graphene impermeability will be used to trap several liquids on a  $\text{TiO}_2$  surface, in order to create sealed liquid cell for different analysis.

## 1.4 Synthesis methods

Since the first discovery in 2004 through mechanical exfoliation of graphite, different methods have been developed for graphene production: chemical vapour deposition (CVD), liquid phase exfoliation or epitaxial growth on silicon carbide (SiC), only to cite a few. Each technique shows advantages and but also disadvantages of the produced graphene. The scheme in Fig. 1.5 shows the relation between the most common production methods and graphene quality. These techniques are described in detail in next sections.

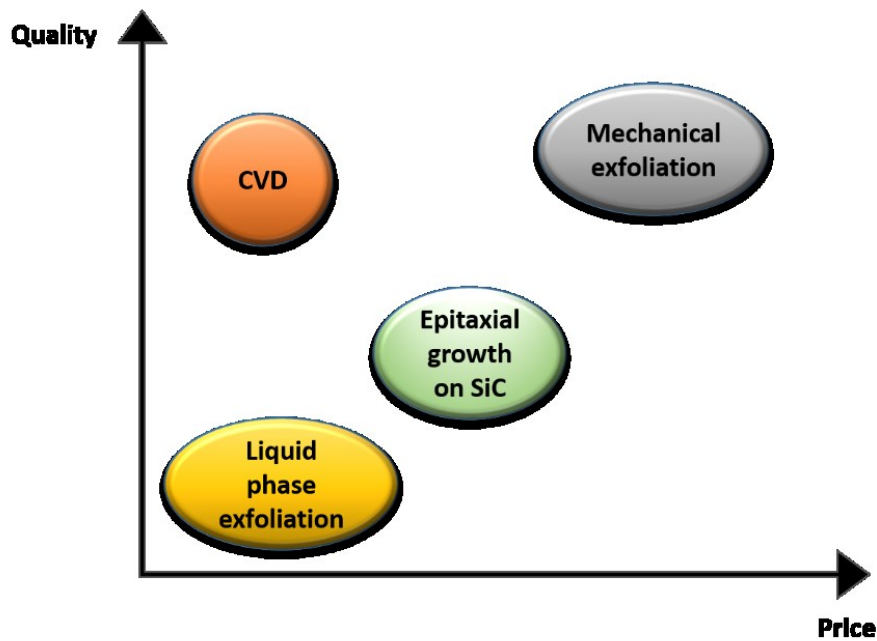


Fig. 1.5: different synthesis method in relation with price and quality.

#### 1.4.1 Mechanical exfoliation

The mechanical exfoliation technique, or scotch tape technique, is based on the cleavage of graphite with the use of a tape. The van der Waals bonds between graphite planes are of the order of  $2 \text{ eV/nm}^2$ , so the force to separate  $1 \mu\text{m}^2$  of graphite peeling the sheet is  $300 \text{ nN}$ , assuming the graphene substrate friction coefficient equal to 1 [14]. Using a common tape, it is possible to cleave few graphite sheets and transfer them on a substrate just pressing the tape and peeling the sheet when the tape is removed. Graphene remains attached to the substrate due to van der Waals forces (i.e. for  $\text{SiO}_2$  the adhesion strength is  $0.45 \text{ J/m}$  [15]). Usually, highly oriented pyrolytic graphite (HOPG) is used for this purpose because is highly pure and ordered and the individual crystallites are well aligned to each other. In Fig 1.6 the different steps of the process are shown:



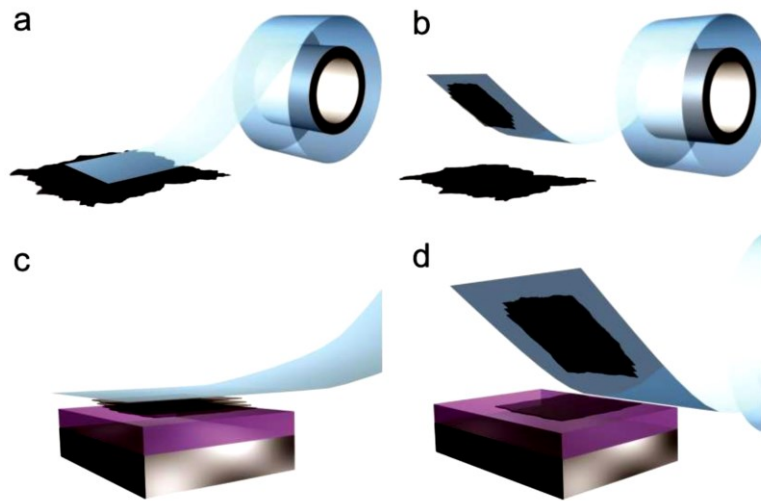


Fig. 1.6: mechanical exfoliation process: (a) tape is pressed against the HOPG surface; (b): HOPG sheets are peeled with the removing of the tape, resulting in few crystals of layered materials; (c) the tape is pressed against the desired substrate and (d) peeling off the tape, the bottom sheet is left on the substrate [16].

Mechanical exfoliation is a fast, handle technique and produces the highest graphene quality but presents several important disadvantages. First of all is not reproducible and the production of flakes with single carbon layer is merely a matter of chance; second, the flakes are not homogeneously distributed on the surface, the majority of them are graphene multilayer while the number of monolayers is limited; finally, the size of the obtained flakes is usually tens of micron, so is not useful when large-area graphene is needed.

#### 1.4.2 Liquid phase exfoliation

The liquid phase exfoliation involves the use of a reactant for the separation of graphite planes. Usually hydrogen peroxide, sulfuric acid or acetic acid [17] are used; graphite is immersed in the liquid and exfoliated by ultrasonication. The result is graphene oxide flakes suspended in a colloidal solution. These flakes can be reduced to form graphene flakes, using hydrogen plasma or alkaline solutions. An example of the process taken from the ref. [18] is shown in Fig. 1.7.

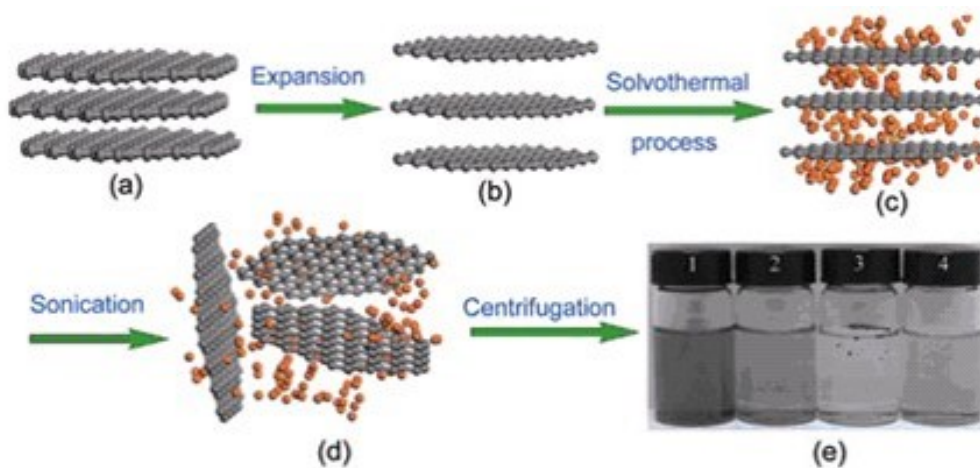


Fig. 1.7: Scheme of liquid phase exfoliation: (a) pristine graphite; (b) expanded graphite; (c) insertion of acetonitrile molecules into the interlayers of the expanded graphite; (d) exfoliated graphene planes dispersed in acetonitrile; (e) samples under different conditions: solvothermal process (1) 600 rpm, 90 min; (2) 2000 rpm, 90 min; solvothermal-free process (3) 600 rpm, 90 min; (4) 2000 rpm, 90 min [18].

Usually the method is used to produce graphene nanoribbons with lateral size  $< 10$  nm [19]. The advantage of the technique is the low cost and the ease in handling. It is possible to control the size of the graphene flakes controlling the time of sonication step: the longer is the sonication time, the smaller is the size of the flakes because fragmentation occurs [20]; on the other hand, graphene  $sp^2$  bonds are degraded to  $sp^2$ - $sp^3$  bonds and this results in a degradation of quality and purity of flakes. Nevertheless, this method is suitable for many applications, such as the production of graphene based inks or as a source of a component of composite materials.

### 1.4.3 Chemical Vapour Deposition

The most popular approach to obtain large-area graphene is chemical vapour deposition (CVD). Molecules of a hydrocarbon gas such as methane ( $CH_4$ ), ethylene ( $C_2H_6$ ), acetylene ( $C_2H_2$ ) are used as precursor; generally, these molecules are decomposed at 900-1000 °C in a range of pressure from 100 Pa to  $10^5$  Pa. At these temperatures, the molecules in contact with the surface decompose; the carbon atoms stick to the substrate with the formation of

graphene layers, while other volatile species are desorbed. In case of  $\text{CH}_4$ , for instance, the occurred reaction is described in (1.4):



Different metals have been used as a substrate for graphene growth, such as platinum, cobalt, iron, iridium [21] but at present the most used are nickel (Ni) and copper (Cu). A general scheme of the process which involves the decomposition of  $\text{CH}_4$  is shown in Fig. 1.8.

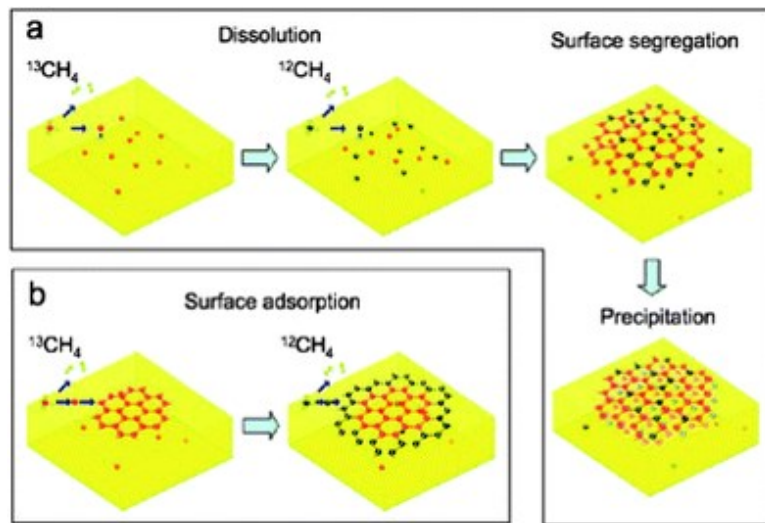


Fig. 1.8: scheme of the CVD graphene growth process: a) carbon segregation/precipitation mechanism and b) the surface growth mechanism [22].

A precise control of the process parameters is necessary to form graphene monolayer with high quality. Cu seems to be the most appropriate metal substrate: it enhances the decomposition of hydrocarbon molecules because its electronic configuration [23]; graphene starts to nucleate in specific sites and when the surface is fully covered, the process is self-limited [24]. An important step is the treatment of the substrate before the carbon deposition; because Cu is covered with native oxide which can reduce the catalytic effect, it is usually treated with acetic acid [25] or annealed in  $\text{H}_2$  to remove the oxide. This process can be used also to remove oxidative carbon which suppresses the graphene flake nucleation [26].

Ni surface are usually used to obtain few layer graphene formation.  $\text{CH}_4\text{-H}_2$  mixture at  $T \geq 1000$  °C is used for the decomposition of  $\text{CH}_4$  that creates a concentration gradient between surface and bulk and causes the diffusion of carbon atoms into the metal. After the

saturation, graphite is formed on the surface and graphene is formed with cooling. The  $\text{CH}_4/\text{H}_2$  ratio is an important parameter: a poor quantity of  $\text{H}_2$  results in oxidized metal layers which lead to a disordered graphene formation; an excess of  $\text{H}_2$ , on the contrary, lead to graphene etching.

CVD method is one of the most used for graphene production, because offers the possibility to grow large-area graphene foils. For instance, the production of 35-inch of CVD grown graphene has been achieved [27].

#### 1.4.4 Epitaxial growth

It is possible to epitaxially grow graphene on SiC wafer at high temperature ( $\sim 1500\text{ }^\circ\text{C}$ ) in ultra-high vacuum (UHV) ( $5 \times 10^9\text{ mbar}$ ); in this conditions, silicon at the surface is sublimated and carbon atoms reorganize themselves and grafitization is achieved [28]. A schematic illustration of the process is shown in Fig. 1.9.

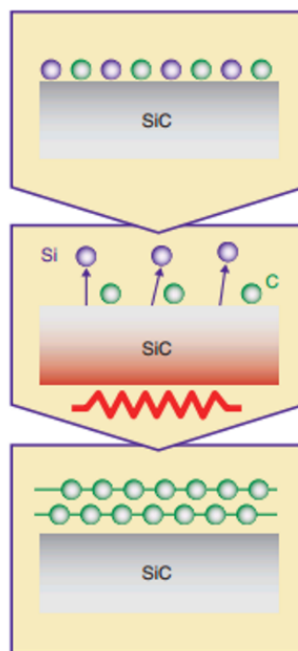


Fig. 1.9: schematic illustration of the epitaxially growth of graphene on a SiC substrate [29].

As first disadvantage, the size of the SiC wafer limits the size of the grown graphene. Secondly, the quality of the obtained graphene is poor if compared with the one fabricated

with mechanical exfoliation or CVD process. However, epitaxial growth process is quite handy, and is largely used in semiconductor industries for the fabrication of electronic devices.

## 1.5 Applications

The remarkable properties of graphene quickly exploded in a large number of application in almost every sector of research and industry: electronic, materials, optics, biomedical, just to cite a few. A complete list would require a separate study and goes beyond the scope of this thesis. However, because of the great impact they had in both research and market, the most important applications will be overviewed in the next sections.

### 1.5.1 Graphene field-effect transistors

The International Technology Roadmap for Semiconductors (ITRS), which is sponsored by the world's top integrated circuit manufacturing companies, has forecasted the end of CMOS-based technology in 2022 [30]. Nowadays, the progress in digital logic is going to the down scaling CMOS devices, with the requirement of more and more low voltage, low power and high performances. However, this demand is approaching fundamental limits due to various factors, such as decreased power density, leakage currents and production costs. For this reason, semiconductor industry is searching new classes of materials which can substitute silicon and meet the new demand at the same time.

Graphene seems to be the perfect candidate to be integrated in electronic devices, due to its very large field-effect mobility, ballistic transport properties and the zero band gap. The first graphene-based FET (G-FET) was reported by Novoselov *et al.* in 2004 [1]. Fig. 1.10 shows optical and atomic force microscopy (AFM) images of the few layer graphene used for the G-FET fabrication (Fig. 1.10 a,b and c). In Fig. 1.10e and 1.10d a scheme and a scanning electron microscope (SEM) image of the final device are shown.

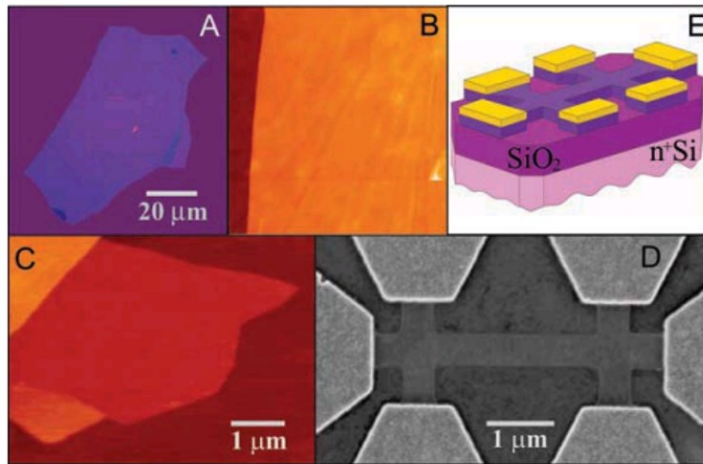


Fig. 1.10: a) optical image of a multilayer graphene flake transferred on SiO<sub>2</sub> wafer; b) AFM image of 2 μm x 2 μm area of the flake near its edge; c) AFM image of single-layer graphene on SiO<sub>2</sub> surface; d) SEM image of the experimental device with few layer of graphene; e) schematic of the final device [1].

Because of the zero bandgap, the  $I_{on}/I_{off}$  current of G-FETs is quite low ( $I_{on}/I_{off} < 30$  at 300 K) [1] and limits the graphene use in digital switching devices. However, it is possible to modify the graphene band structure opening a bandgap in different ways: by constraining large-area graphene in one dimension to form graphene nanoribbons, by biasing bilayer graphene or by applying a strain [31].

Starting from the first G-FET, many others have been fabricated and tested. The first graphene top-gate MOSFET was reported in 2007 [32], and later top gated graphene MOSFETs have been produced by mechanical exfoliation [33], carbon segregation [34] and CVD graphene grown on metal [35].

## Fabrication of a G-FET at IOM-CNR

### (i) Fabrication of the substrate:

- fabrication of the circular cavity on Si/SiO<sub>2</sub> by optical lithography using optical resist S1813 1.5 μm-thick; this is used like mask for the following wet etching in Buffered Oxide Etch of the SiO<sub>2</sub> (thickness 300 nm);
- production of electrodes: optical lithography on a layer of SU-8 1.6 μm-thick spin coated on the substrate, thermal evaporation of the metal (Cr:Au 20:20 nm), and subsequent lift-off in order to obtain the electrodes.

### (ii) Transfer of graphene on the fabricated substrate:

- graphene is obtained with mechanical exfoliation of HOPG. The exfoliated flakes are transferred through slight pressure on a Si/SiO<sub>2</sub> substrate previously covered by a film of water soluble polyvinyl alcohol (PVA) 50 nm-thick and a thin film of poly(methyl methacrylate) (PMMA) 300 nm-thick. The recognition of graphene sheets is carried out with optical microscopy inspection. The evaluation of graphene thickness is achieved by a custom written Matlab program, which analyzes the absorbance of the optical image. After graphene identification, the PVA-PMMA membrane is cut to form a closed loop that contains the monolayer. The sample is placed in a container at an angle of about 45 degrees from the table surface and water is slowly injected into the container via a syringe, so as to allow water to penetrate under the PMMA, which is insoluble, and to dissolve the PVA. The PMMA-graphene membrane floating on water is picked up through a silicon holder with circular hole. The transfer of the PMMA-graphene membrane on the prepatterned Si/SiO<sub>2</sub> substrate is achieved using a micropositioning system; after the drying of the membrane, PMMA is stripped in MF 322 developer;
- to avoid the graphene detachment from the substrate, a layer of SU-8 photoresist 500 nm-thick is spin coated on the graphene and patterned with optical lithography.

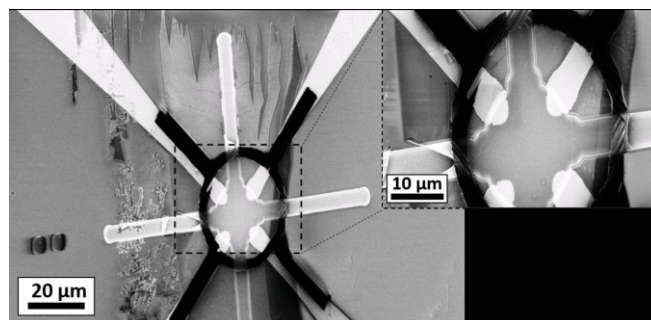


Fig. 1.11: SEM image of the obtained G-FET. The inset shows a zoom on the suspended graphene flake on the hole [Hussein *et al.*, unpublished].

## 1.5.2 Graphene FET for biosensing

Graphene field effect transistors (G-FETs) have received a lot of attention due to their high sensitivity and low noise. The 2D structure of graphene constitutes an absolute maximum of the surface to volume ratio, so there is no distinction between the surface sites and the bulk material; every tiny amounts of deposited atoms determine a fraction of the total coverage and so every absorption event is significant. In a typical G-FET, graphene is used as conductive channel between drain and source electrodes. The gate potential is applied on a back-gate or a top-gate. The adsorbed molecule changes the carrier concentration of graphene and this leads to a changing in the electrical graphene conductivity. A suitable chemical functionalization of graphene allows the use of G-FETs in biosensing field, with the absorption of a large variety of molecules. Graphene biosensors are able to measure change of coverage of the order of  $10^{-6}$  fg [36] approaching to the detection of a single molecule. Biomolecules such as proteins, cells or DNA have been detected. For instance, G-FET was successfully used for detection of protein in bovine serum albumin buffer in the nanomolar scale [37] or for detection of signal from living cells [38], or even epitaxially grown graphene was used as channel to detect DNA with single-base-mismatch sensitivity [39]. Fig. 1.12 shows the first selective bio-molecule G-FET in which a flake of graphene is functionalized with an aptamer-antibody reaction in order to have a selective sensing of protein [40]:

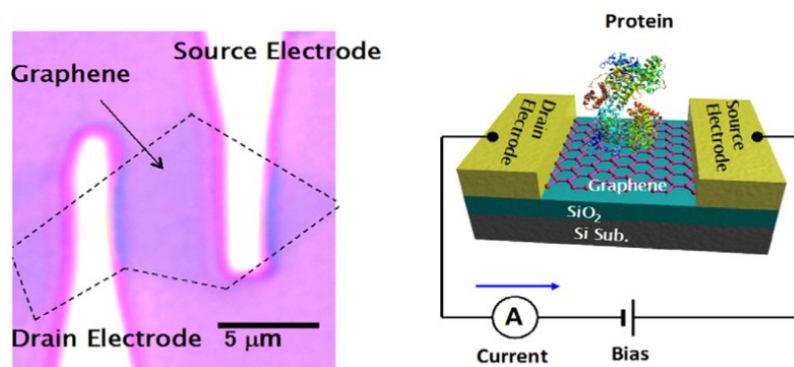


Fig. 1.12: optical microscope image of the device with source and drain electrodes and graphene channel (left) and a schematic image the G-FET (right) [40].



### 1.5.3 Graphene for transparent membranes

Membranes are used in different fields, from chemistry to biology, from cellular compartmentalization to mechanical pressure sensing. Generally, a membrane is used to separate two different environments, but maintaining the possibility to transfer information from one environment to the other, which can be of a physical, chemical or a mechanical nature. Graphene is the ultimate limit for the concept itself of a solid membrane: only one atom-thick, but electrically conductive, impermeable to ions and molecules and stronger than steel. A schematic of a graphene micro-chamber is shown in Fig. 1.13a and b, obtained transferring mechanical exfoliated graphene on a SiO<sub>2</sub> substrate [41].

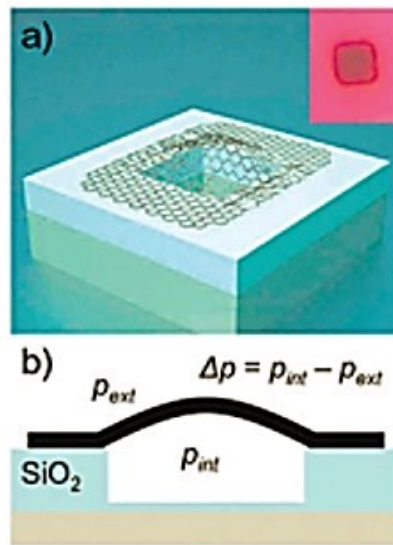


Fig. 1.13: (a) Schematic of a graphene sealed microchamber. In the red insert, an optical image of a single atomic layer graphene drumhead on 440 nm of SiO<sub>2</sub> is shown. The sizes of the microchamber are 4.75 mm 4.75 mm 380 nm. (b) Side view schematic of the graphene sealed microchamber [41].

Graphene membrane can be used as sensor in probing pressure changes associated to chemical reaction or photon detection [42], can allow spectroscopic studies probing the permeability of gases through atomic vacancies in single layers of atoms and defects [43] and can act as selective barriers for ultrafiltration [44].

The molecular impermeability of graphene, joined with its ultrahigh electron transmittivity in a wide electron range [45] and high electrical conductivity, make graphene an ideal

material for in situ environmental electron microscopy. Graphene and graphene oxide (GO) can be well implemented in the realization of environmental-cells (E-cells) for SEM, transmission electron microscopy (TEM) and x-ray electron spectroscopy. The Chapters 3 and 4 will present three experimental applications developed in our laboratory which use graphene as transparent membranes for x-ray electron spectroscopy and this topic will be treated in details.

#### 1.5.4 Graphene for transparent and flexible electronics

Until now, the most used material for the realization of flexible electronics was indium tin oxide (ITO), a n-doped semiconductor composed of  $\sim 90\%$   $\text{In}_2\text{O}_3$ , and  $\sim 10\%$   $\text{SnO}_2$  [46]. ITO is commercially available with transmittance (T) of  $\sim 80\%$  and sheet resistance ( $R_s$ ) of  $\sim 60$ - $300 \Omega/\square$  on polyethylene terephthalate (PET) [47]. Despite its flexibility and transparency, the amount in nature of indium and tin is poor and consequently the cost is growing [48].

Graphene could be a perfect substitute of ITO, for three main reasons: there is carbon abundance, the monoatomic structure and the mechanical properties allow dramatic mechanical deformation [49], and it can be folded without breaking.

The use of graphene in transparent electrodes has been demonstrated in different flexible optoelectronic devices, such as touch-screen sensors [27], organic light-emitting diodes [50], and organic photovoltaic devices [51]. In 2010, SKKU and Samsung collaborated to produce the first roll-to-roll 30-inch graphene transparent conductors [27], with low  $R_s$  and  $T=90\%$ . Fig. 1.14 shows a graphene-based touch panel (Fig. 1.14a) and a touch screen panel connected with a computer (Fig. 1.14b).

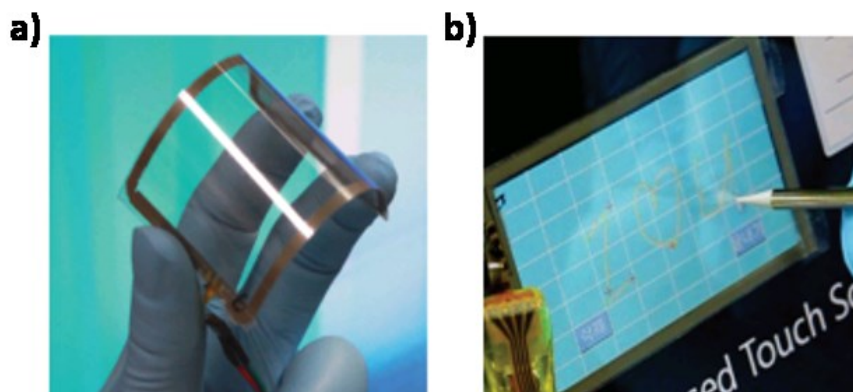


Fig. 1.14: a) an assembled graphene/PET touch panel showing outstanding flexibility; b) graphene-based touch-screen panel connected to a computer with control software [27].

### 1.5.5 Photovoltaic devices

The majority of solar cells available in the market are composed of silicon-based materials [52]. However, the research is heading to address materials with high flexibility and low manufacturing cost, to produce organic photovoltaic cells (OPVs) [53] and dye sensitized solar cells (DSSCs) [54], that are substituting the silicon-based ones. In the last decade, the power conversion efficiency of OPVs and DSSCs has reach the 9% [55] and 15% [56], respectively. The most common material used in this kind of cells is the ITO for its flexibility and transparency. In spite of the ITO advantages described in the previous section, for the application in solar cells it presents a series of disadvantages; for instance, its poor transparency in the near infrared region, which restricts its use in a wider range of solar energy. As for flexible screens, new materials are entering in this field for ITO replacement and graphene is the one most promising. The optical transmittance of a monolayer or a few-layer graphene grown by CVD is superior to that of ITO and the sheet resistance of graphene films is comparable to that of ITO because of graphene's high carrier mobility ( $> 10^3 \text{ cm}^2 \text{ V}^{-1} \text{ s}^{-1}$ ) and high carrier density ( $> 10^{12} \text{ cm}^{-2}$  for doped samples). Graphene films of 4, 12 and 22 nm exhibit transparencies of 90, 80 and 66%, respectively at a wavelength of 500 nm [48], so it can be well used in organic solar cell as electrodes [57], electron transporters/acceptors [58] and hole transporters [59]. Fig. 1.15 show an example of reduced GO thin film used as transparent electrode in an inorganic-organic solar cell.

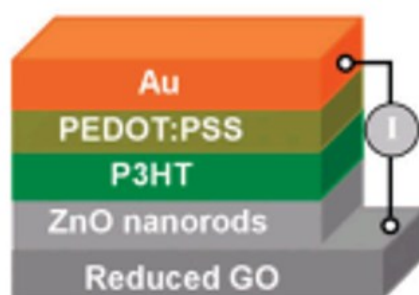


Fig. 1.15 Schematic illustration of a reduced GO thin film used as the transparent electrode in a layered structure of quartz/rGO/ZnO NRs/P3HT/PEDOT:PSS/Au hybrid solar cell [57].

The best performances were achieved to date has efficiency  $\approx 1.2\%$  using CVD graphene as the transparent conductor with  $R_s = 230 \Omega/\square$  and  $T = 72\%$  [60]. Further optimization is possible, considering that graphene-hybrid structure has shown even better results ( $R_s = 20 \Omega/\square$ ,  $T = 90\%$ ) [61].

### 1.5.6 Bioapplications

Graphene properties make it suitable also for biological applications, because of its large surface area, unique mechanical properties, non-toxicity, and the wide range of chemical modifications than can be adopted in biofunctionalization processes, which are essential for biological recognition. Applications range from regenerative medicine [62], incorporation in scaffold materials to improve strength, elasticity and selectivity [63], carriers for drug delivery [64] or gene therapy [65], antibacterial agents [62] up to bioimaging probes.

As mentioned before, graphene can be covalent modified to impart specific biological activity. For instance, a covalent modifications consisting in an oxidation process known as “Hummers method” can be used to fabricate GO starting from graphite [66]. While pristine graphene is hydrophobic (water contact angle of  $90^\circ$ ), GO surface is partially hydrophilic, (water contact angle of  $40 - 50^\circ$  [67]) and presents carboxylate groups with negative charges on edge sites [68]; for this reason, graphene can promote biochemical reaction primarily at the edge or defect sites, while GO promotes the reaction on all the carboxylated groups.

Another interesting approach is the application of graphene in molecular probes that use fluorescence or fluorescence quenching [69]. For instance, polyethylene glycole and GO have been used as a platform for covalent attachment of fluorophores for in vivo and in vitro cellular imaging [70]. The mechanical properties of graphene such as high elasticity, flexibility, and adaptability to flat or irregular surfaces allow graphene use also for the structural reinforcement of biocompatible films, hydrogels, and other scaffold materials used for tissue engineering. For instance, hydrogel composites have been used as scaffolds or cell-encapsulating fillers to generate or repair tissues such as skin, bladder, cartilage, and bone [71], due to their resemblance to soft tissue. Moreover, the use of a graphene-based nanomaterial for the design of hybrid nanofibrous scaffolds was used to guide neural stem cell (NSCs) differentiation into oligodendrocytes [72]: polymeric nanofibers composed of polycaprolactone (PCL) generated using electrospinning were coated with GO and seeded

with neural stem cells (NSCs). These cells show enhanced differentiation into oligodendrocyte lineage cells. In Fig. 1.16 a scheme of the process (left) and the results (right) are presented.

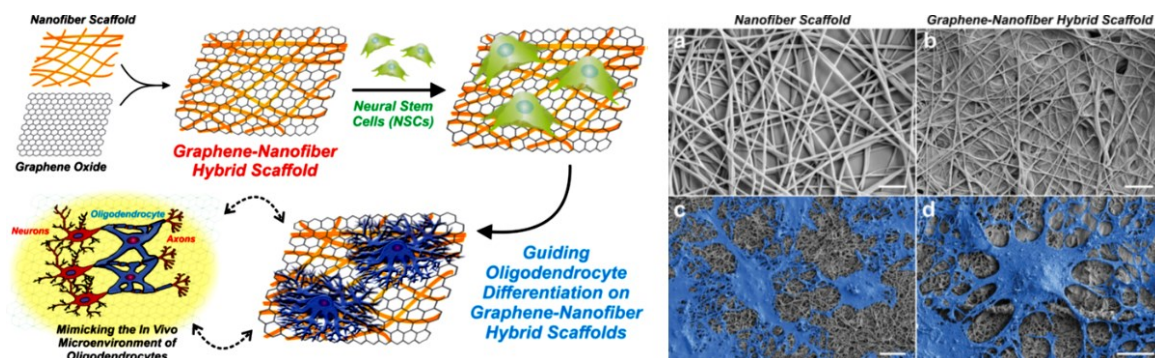


Fig. 1.16: Left. Scheme of the fabrication and application of graphene-nanofiber hybrid scaffolds. Right. SEM images of: a) PCL nanofibers, (b) and PCL nanofibers coated with GO. Scale bars: 2  $\mu\text{m}$ . c,d) SEM of nanofiber scaffolds (c) differentiated NSCs cultured on PCL/graphene nanofiber hybrid scaffolds (d) after six days of culture. Scale bars: 10  $\mu\text{m}$  [72].

In the last decade, graphene has been explored as substrate for neuronal interfacing [73]. Mouse hippocampal cells were cultured on a graphene substrate to analyze neural functions. The results revealed high biocompatibility, low toxicity and an increase of neuronal number respect to controls. In the experimental Chapter 5 the neuronal functions of primary cultures of hippocampal mouse on supported and suspended graphene will be presented.

### 1.5.7 Patterning of graphene

For a precise control of size and electronic properties, graphene can be patterned to obtain the desired configuration. Different methods can be used to generate the pattern, such as optical lithography [74], e-beam lithography [75], or solid-phase laser direct writing [76], just to cite a few. Optical lithography is one of the most used because of its accessibility: a conventional negative photoresist is spin coated on graphene and irradiated with UV light; after exposure, the photoresist acts as protective pattern to the subsequently exposition to

oxygen plasma [77]. The unprotected portion of graphene is chemically removed upon the attack by the reactive plasma and carried into the vapour phase.

I used the latter protocol to realize different graphene geometries; Fig. 1.17 shows some examples of suspended graphene patterned with lines of different length. In synthesis, I fabricated a grating of micrometric lines in a bulk silicon substrate with optical lithography and dry etching techniques. Commercially CVD on Cu graphene purchased from Graphenea S.A. [78] is covered with a thin layer of optical resist and exposed to UV light through a photomask. The final pattern is obtained exposing the graphene to an oxygen plasma to remove the unprotected parts. Cu is etched in a diluted  $\text{FeCl}_3$  metal etching solution before the graphene wet transfer. Critical point drying (CPD) is performed to avoid the collapse of the suspended structures. Details about the fabrication process will be provided in the experimental Chapter 2.

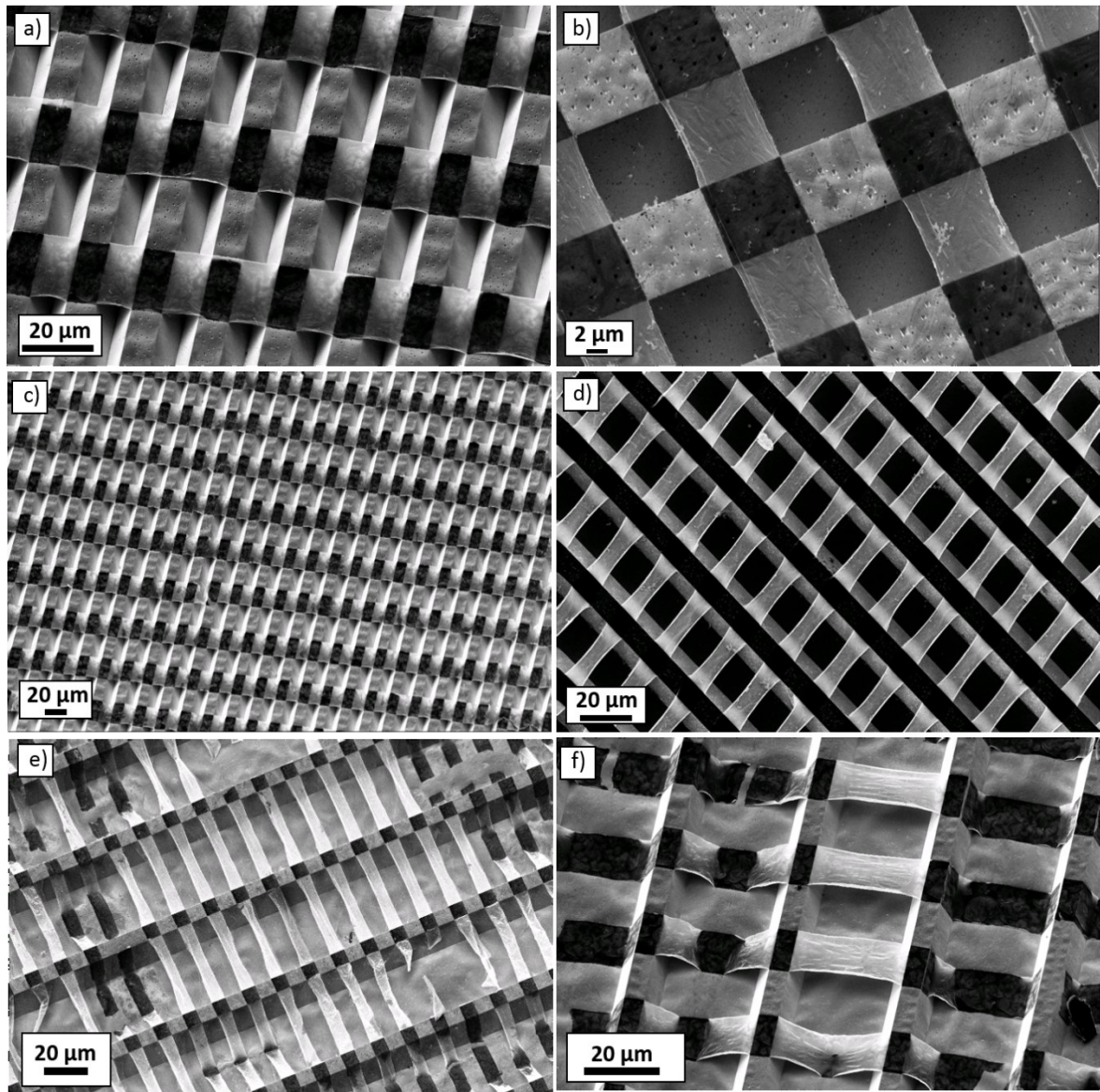


Fig. 1.17: SEM images of different configurations of suspended graphene pattern obtained in our laboratory: a) grating of lines in bulk silicon with length and periodicity of 10  $\mu\text{m}$  and 20  $\mu\text{m}$  respectively. Graphene is patterned in lines with length and periodicity of 10  $\mu\text{m}$  and 20  $\mu\text{m}$  , respectively; b) same geometrical factors of a) obtained on a silicon substrate covered with 50 nm of gold deposited with thermal evaporation; c) graphene lines of 10  $\mu\text{m}$  and 25  $\mu\text{m}$  of length and period, respectively, obtained on a bulk silicon covered with 50 nm of gold; d) same configuration of c) but on silicon substrate; e) graphene lines of 10  $\mu\text{m}$  and 50  $\mu\text{m}$  of length and period, respectively obtained in bulk silicon; f) same configuration of e) in which are zoomed some graphene structures collapsed [Matruglio *et al.*, unpublished].

Another approach to obtain the desired shape and form of the graphene is pre-pattern the substrate and then grown graphene on the top. For instance, graphene film on pre-patterned Ni substrate was demonstrated [79]; after the growth, graphene can be transferred to another substrate with conventional transfer methods. Smaller size graphene pattern can be obtained with direct writing using focused ion beam lithography (FIB) [80] or e-beam lithography (EBL) [81] which can provide nanometric size of the patterned structures. Also scanning tunneling lithography has been used to cut graphene nanoribbons from 2.5 nm to 120 nm [82]. Moreover, graphene nanoribbons have been fabricated by local anodic oxidation lithography using tapping mode AFM [83].

## **1.6 Graphene transfer**

Although researches are looking for the improvement of all parameters in graphene synthesis to obtain a uniform, high quality, low defected graphene, it is important to observe that there is a critical step in which graphene is degraded and defected: the transfer. In fact, in order to integrate graphene to functional devices, usually it should be transferred from the growth substrate to the device one. In 90's Ruoff and coworkers transferred islands of graphite on Si(001) flat substrates by rubbing the HOPG surface against the silicon surface [84]. Anyway, it is only in 2004 that Geim and Novoselov isolated a single layer graphene from graphite and transferred it by scotch tape technique on an oxidized silicon wafer [1]. Several methods have been developed so far; in the next sections the main techniques are listed.

### **1.6.1 Transfer by mechanical exfoliation**

As shown in the section 1.4.1, mechanical exfoliation from graphite is one of the most used method to obtain high-quality graphene flakes. Graphite is peeled using tape and graphite flakes are transferred on a substrate, pressing and peeling the tape. The products are flakes of different thickness. The identification of the single layer can be obtained by different techniques, such as Raman spectroscopy, AFM or optical microscopy. Raman spectra exhibit typical features based on the number of present layer [85]; AFM is able to identify the thickness of the deposited layer and so to measure the number of the layers of each flake.



[86]; optical microscopy takes advantage from the modulation of reflection at the air-graphene-substrate interface, so a thickness evaluation is detectable by visual inspection [87]. Examples of the application of these three approaches are shown in Fig. 1.18.

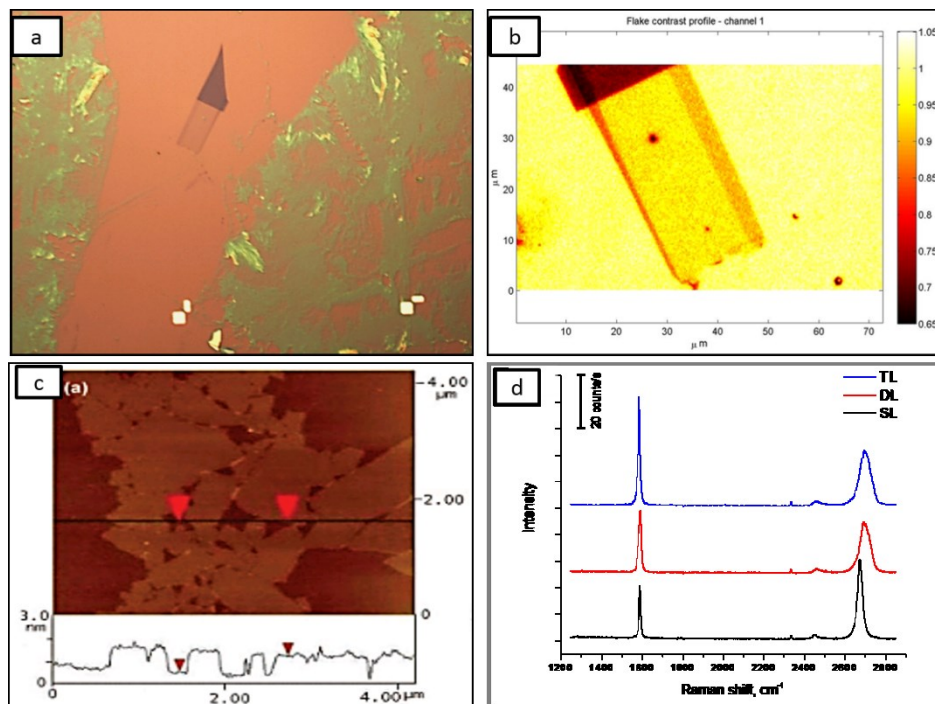


Fig. 1.18: a) optical image a graphene flake on SiO<sub>2</sub> which I obtained by mechanical exfoliation of HPOG [Matruglio *et al.*, unpublished]; b) recognition of the same flake with a custom written Matlab program which allows the recognition of the thickness through the analysis of the absorbance of the optical image; c) AFM image of graphene oxide sheets on cleaved mica; the height difference between two arrows is 1 nm, indicating a single graphene oxide sheet [88]; d) Raman spectra of mechanical exfoliated graphene transferred on SiO<sub>2</sub> obtained with 532 nm excitation laser: single layer (black spectrum), double layer (red spectrum) and three layer (blue spectrum) [Naumenko *et al.*, unpublished].

Mechanical exfoliation can be used also for transfer graphene grown on SiC. For instance, a bilayer of gold and polyimide [89] or platinum and polyimide [90] can be gently lifted from the SiC and delivered to the desired substrate, but a high number of defects are introduced. Another approach involves the use of thermal release tape to peel of graphene from SiC [91] but electrical properties highly decrease because of defects and contaminants due to the tape.

Although mechanical exfoliation is a low-cost and handle technique, it presents a series of disadvantages: the quantity of contaminant due to tape glue is not negligible (as also evident in Fig. 1.17a, green residuals). Furthermore, the size of the graphene sheet is random and usually reach tens of micron at best; moreover, the shape is irregular and the orientation of the lattice is not controllable. For these reasons, the method is not suitable when large area and regular sheets are required and have limited relevance in industrial applications.

### 1.6.2 Wet transfer techniques

In the CVD synthesis, the metal substrate is used for catalytic purposes and usually is eliminated in order to transfer graphene on the desired device. Since a single layer of graphene is extremely fragile and is prone to fold on itself, break and tear, a polymeric supporting layer is usually deposited before etching the metallic substrate. The polymer is deposited by spin-coating on the top of graphene and the polymer/graphene/metal layer is immersed in an etching solution in order to etch metal from the bottom. Ni and Cu substrate can be etched in different solutions, such as  $\text{FeCl}_3$ ,  $\text{Fe}(\text{NO}_3)_3$ ,  $(\text{NH}_4)_2\text{S}_2\text{O}_8$ . After the rinsing in deionized (DI) water, the polymer/graphene layer is transferred on the desired substrate. Finally, the polymer is removed with a specific solvent, graphene is washed in DI water and then dried. Several polymers can be used for wet transfer, such as poly(bisphenol A carbonate) (PC) [92] removed in chloroform, or polyisobutylene (PIB) [93], which could be removed in decane, hexane or squalene. Because of its low viscosity and flexibility, the most common used polymer is poly(methyl)metacrylate (PMMA), usually removed in acetone. A general transfer method with involves the use of PMMA is shown in Fig. 1.19.

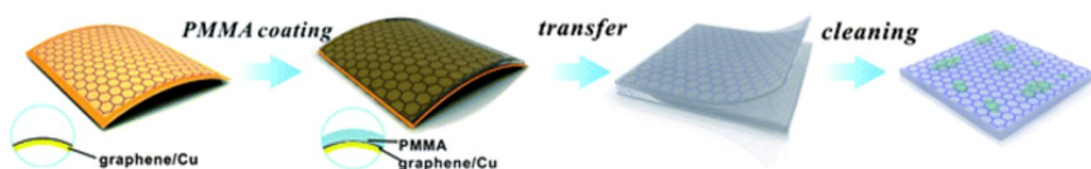


Fig. 1.19: general procedure involving the use of PMMA in graphene transfer [94].

Removal of residuals is a demanding step; impurities tend to *p*-dope graphene and to cause carrier scattering, leading to the degradation of electrical and physical properties. Residuals are hard to remove with solvents, or with very harsh protocols such as annealing at high temperature. The problem will be well analyzed in Chapter 2 and an experimental, novel technique for residual reduction will be presented.

Despite residuals problem, PMMA is used as supporting layer also in case of electrochemical delamination of graphene grown by CVD [95]. In detail, the PMMA/graphene/metal is used as cathode and a glassy carbon as anode in an aqueous solution; a voltage is applied and there is a formation of hydrogen bubbles that emerge at the graphene-metal interfaces and delaminated the graphene from the metal substrate starting from the edges. After the delamination, PMMA is dissolved with acetone as in a typical wet transfer protocol. An image of the electrochemical cell used for graphene delamination which I performed in our laboratory is shown in Fig. 1.20.

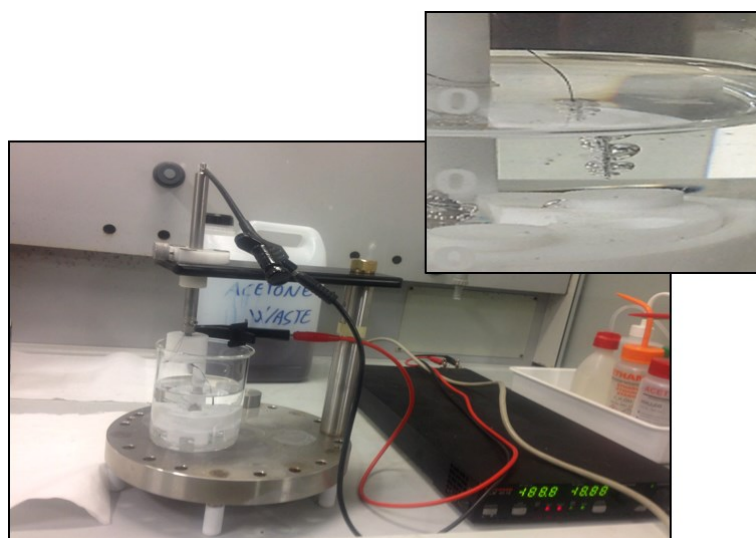


Fig. 1.20: pictures of the electrochemical cell used for PMMA-covered graphene detachment from a Cu substrate. The inset shows a zoom on the sample, in which bubbles formation is evident.

As alternative to PMMA, an interesting approach was demonstrated with the use of polydimethylsiloxane (PDMS), for CVD graphene transfer [96]. PDMS is unreactive, solvent resistant and has low surface energy; it can be stamped onto a substrate with the desired shape, deposited on the graphene for supporting during the metal etching and transferred on the desired substrate. After transfer, PDMS is peeled away leaving graphene

on the new substrate. An example of the use of a PDMS stamp for graphene transfer is shown in Fig. 1.21.

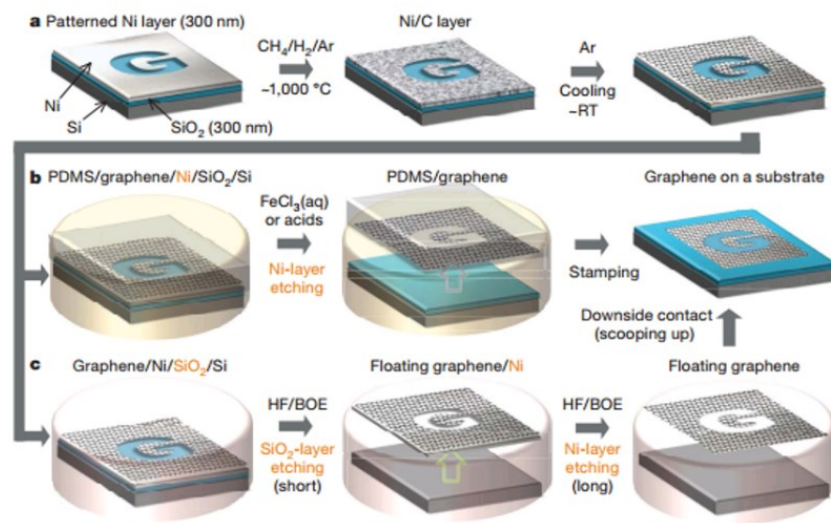


Fig. 1.21: synthesis, etching and transfer processes for the largescale and patterned graphene films. a) synthesis of patterned graphene films on thin nickel layers; b) etching using  $\text{FeCl}_3$  (or acids) and transfer of graphene films using a PDMS stamp; c) etching using buffered oxide etch (BOE) or hydrogen fluoride (HF) solution and transfer of graphene films; RT is room temperature ( $\sim 25^\circ\text{C}$ ) [96].

Despite the large use of polymer as supporting layer in graphene transfer, some works show the possibility to make it without the use of any polymer [97] using, for instance, a graphite holder (as show in Fig. 1.22) and a mixed solution to reduce the surface tensions.

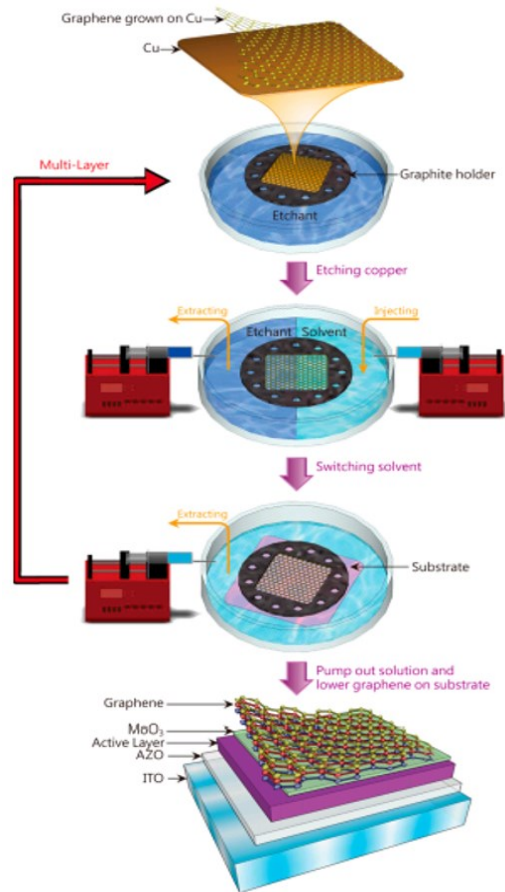


Fig. 1.22: schematic illustration of the polymer-free graphene transfer process [97].

Avoiding the use of polymer, residuals are eliminated, but this method is dangerous because single layer graphene is prone to break, and the percentage of failure can be high.

### 1.6.3 Dry transfer techniques

The dry transfer techniques do not use wet solution for graphene transfer. The most famous method to transfer very large-area CVD graphene is the *roll-to-roll* technique [27]: it consists in the use of a thin polymer film coated with a thermal release tape attached onto the graphene on metal, obtained passing through two rollers; metal is etched with electrochemical reaction in an aqueous solution of  $(\text{NH}_4)_2\text{S}_2\text{O}_8$ . Finally, graphene is attached on the desired substrate with the help of the two rolls and the tape is removed by heating. The possibility to transfer 30-inch graphene layer with this technique was demonstrated,

opening the availability for industrial applications. A scheme of the roll-to-roll method and the realization of the 30-inch graphene layer are shown in Fig. 1.23.

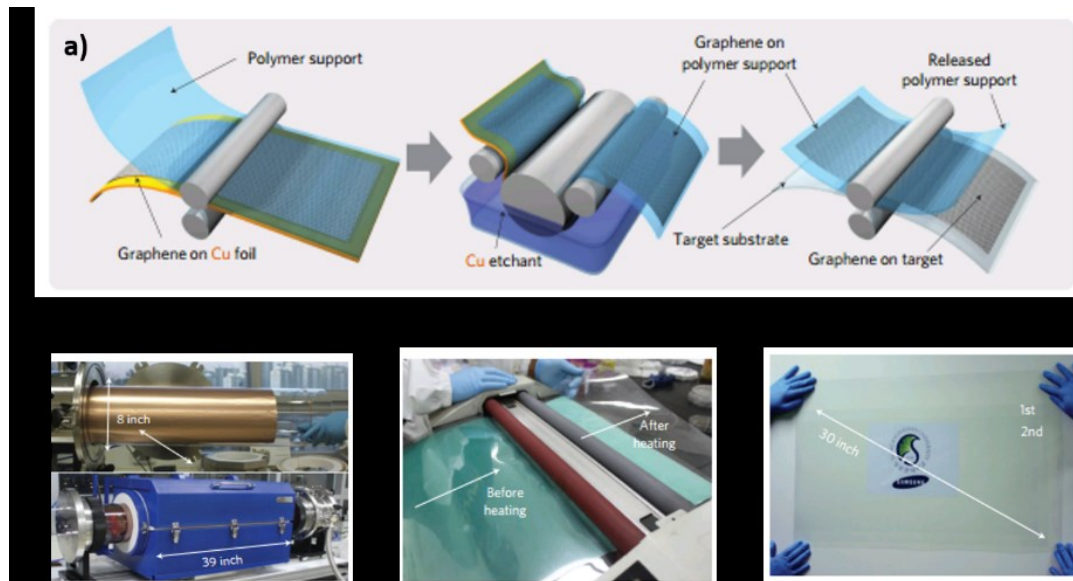


Fig. 1.23: a) schematic of the roll-to-roll based production of graphene films grown on a Cu foil. The process includes adhesion of polymer supports, Cu etching, rinsing and dry transfer-printing on a target substrate. A wet-chemical doping can be carried out using a set-up similar to that used for etching; b) c) d) photographs of the roll-based production of graphene films: a) Cu foil wrapping around a 7.5 inch quartz tube to be inserted into an 8 inch quartz reactor. The lower image shows the stage in which the Cu foil reacts with  $\text{CH}_4$  and  $\text{H}_2$  gases at high temperatures; b) roll-to-roll transfer of graphene films from a thermal release tape to a PET film at  $120\text{ }^\circ\text{C}$ ; c) a transparent ultralarge-area graphene film transferred on a 35-inch PET sheet [27].

The disadvantages on this technique are thermal stress and mechanical defects which can be induced during the procedure, in particular if graphene is transferred on a rigid substrate. Nevertheless, it is promising for industrial applications because of the large graphene area which can be produced.

Another interesting dry etching approaches has been demonstrated with the use of a nanoimprinter assisted by a polymer (i.e. polystyrene) for CVD graphene, to separate graphene from metal [98]. Another similar method was developed with the use of a layer of epoxy to peel off the graphene from the metal [99]. The advantages of these kind of

techniques are the industrial scalability and the possibility to reuse the underlying metal which is not etched.

## References

- [1] Novoselov, K.S., Geim, A.K., Morozov, S.V., Jiang, D., Zhang, Y., Dubonos, S.V., Grigorieva, I.V., Firsov, A.A. *Electric field in atomically thin carbon films* (2004) *Science*, 306 (5696), pp. 666-669.
- [2] Lemme, M.C. *Current status of graphene transistors* (2009) *Solid State Phenomena*, 156-158, pp. 499-509.
- [3] Castro Neto, A.H., Guinea, F., Peres, N.M.R., Novoselov, K.S., Geim, A.K. *The electronic properties of graphene* (2009) *Reviews of Modern Physics*, 81 (1), pp. 109-162.
- [4] Zhang, Y., Tan, Y.-W., Stormer, H.L., Kim, P. *Experimental observation of the quantum Hall effect and Berry's phase in graphene* (2005) *Nature*, 438 (7065), pp. 201-204.
- [5] Lee, C., Wei, X. D., Kysar, J. W. & Hone, J. *Measurement of the elastic properties and intrinsic strength of monolayer graphene*. *Science* 321, 385–388 (2008).
- [6] Balandin, A. A. *Thermal properties of graphene and nanostructured carbon materials*. *Nature Mater.* 10, 569–581 (2011).
- [7] Bunch, J. S. et al. *Impermeable atomic membranes from graphene sheets*. *Nano Lett.* 8, 2458–2462 (2008).
- [8] Nair, R.R., Blake, P., Grigorenko, A.N., Novoselov, K.S., Booth, T.J., Stauber, T., Peres, N.M.R., Geim, A.K. *Fine structure constant defines visual transparency of graphene* (2008) *Science*, 320 (5881), p. 1308.
- [9] Geim, A.K. *Graphene: Status and prospects* (2009) *Science*, 324 (5934), pp. 1530-1534.
- [10] Wei, N., Xu, L., Wang, H.-Q., Zheng, J.-C. *Strain engineering of thermal conductivity in graphene sheets and nanoribbons: A demonstration of magic flexibility* (2011) *Nanotechnology*, 22 (10), art. no. 105705.
- [11] Pinto, A.M., Gonçalves, I.C., Magalhães, F.D. *Graphene-based materials biocompatibility: A review* (2013) *Colloids and Surfaces B: Biointerfaces*, 111, pp. 188-202.
- [12] Berry, V. *Impermeability of graphene and its applications* (2013) *Carbon*, 62, pp. 1-10.
- [13] Xu, K., Cao, P., Heath, J.R. *Graphene visualizes the first water adlayers on mica at ambient conditions*. *Science* 2010;329(5996):1188–91.
- [14] Zhang, Y., Small, J.P., Pontius, W.V., Kim, P. *Fabrication and electric-field-dependent transport measurements of mesoscopic graphite devices* (2005) *Applied Physics Letters*, 86 (7), art. no. 073104, pp. 1-3.



- [15] Yoon, T., Shin, W.C., Kim, T.Y., Mun, J.H., Kim, T.-S., Cho, B.J. *Direct measurement of adhesion energy of monolayer graphene as-grown on copper and its application to renewable transfer process* (2012) *Nano Letters*, 12 (3), pp. 1448-1452.
- [16] Novoselov, K.S., Castro Neto, A.H. *Two-dimensional crystals-based heterostructures: Materials with tailored properties* (2012) *Physica Scripta*, (T146), art. no. 014006.
- [17] Singh, V., Joung, D., Zhai, L., Das, S., Khondaker, S.I., Seal, S. *Graphene based materials: Past, present and future* (2011) *Progress in Materials Science*, 56 (8), pp. 1178-1271.
- [18] Qian, W., Hao, R., Hou, Y., Tian, Y., Shen, C., Gao, H., Liang, X. *Solvothermal-assisted exfoliation process to produce graphene with high yield and high quality* (2009) *Nano Research*, 2 (9), pp. 706-712.
- [19] Wang, H., Robinson, J.T., Li, X., Dai, H. *Solvothermal reduction of chemically exfoliated graphene sheets* (2009) *Journal of the American Chemical Society*, 131 (29), pp. 9910-9911.
- [20] Li, X., Wang, X., Zhang, L., Lee, S., Dai, H. *Chemically derived, ultrasoft graphene nanoribbon semiconductors* (2008) *Science*, 319 (5867), pp. 1229-1232.
- [21] Batzill, M. *The surface science of graphene: Metal interfaces, CVD synthesis, nanoribbons, chemical modifications, and defects* (2012) *Surface Science Reports*, 67 (3-4), pp. 83-115.
- [22] Li, X., Cai, W., Colombo, L., Ruoff, R.S. *Evolution of graphene growth on Ni and Cu by carbon isotope labeling* (2009) *Nano Letters*, 9 (12), pp. 4268-4272.
- [23] Mattevi, C., Kim, H., Chhowalla, M. *A review of chemical vapour deposition of graphene on copper* (2011) *Journal of Materials Chemistry*, 21 (10), pp. 3324-3334.
- [24] Li, X., Cai, W., Colombo, L., Ruoff, R.S. *Evolution of graphene growth on Ni and Cu by carbon isotope labeling* (2009) *Nano Letters*, 9 (12), pp. 4268-4272.
- [25] Levendorf, M.P., Ruiz-Vargas, C.S., Garg, S., Park, J. *Transfer-free batch fabrication of single layer graphene transistors* (2009) *Nano Letters*, 9 (12), pp. 4479-4483.
- [26] Kraus, J., Böbel, M., Günther, S. *Suppressing graphene nucleation during CVD on polycrystalline Cu by controlling the carbon content of the support foils* (2016) *Carbon*, 96, pp. 153-165.
- [27] Bae, S., Kim, H., Lee, Y., Xu, X., Park, J.-S., Zheng, Y., Balakrishnan, J., Lei, T., Ri Kim, H., Song, Y.I., Kim, Y.-J., Kim, K.S., Özyilmaz, B., Ahn, J.-H., Hong, B.H., Iijima, S. *Roll-to-roll production of 30-inch graphene films for transparent electrodes* (2010) *Nature Nanotechnology*, 5 (8), pp. 574-578.

- [28] Berger, C., Song, Z., Li, T., Li, X., Ogbazghi, A.Y., Feng, R., Dai, Z., Alexei, N., Conrad, M.E.H., First, P.N., De Heer, W.A. *Ultrathin epitaxial graphite: 2D electron gas properties and a route toward graphene-based nanoelectronics* (2004) *Journal of Physical Chemistry B*, 108 (52), pp. 19912-19916.
- [29] Hibino, H., Kageshima, H., Nagase, M. *Graphene growth on silicon carbide* (2010) *NTT Technical Review*, 8 (8).
- [30] <http://www.itrs2.net>
- [31] Schwierz, F. *Graphene transistors* (2010) *Nature Nanotechnology*, 5 (7), pp. 487-496.
- [32] Lemme, M.C., Echtermeyer, T.J., Baus, M., Kurz, H. *A graphene field-effect device* (2007) *IEEE Electron Device Letters*, 28 (4), pp. 282-284.
- [33] Meric, I., Han, M.Y., Young, A.F., Ozyilmaz, B., Kim, P., Shepard, K.L. *Current saturation in zero-bandgap, top-gated graphene field-effect transistors* (2008) *Nature Nanotechnology*, 3 (11), pp. 654-659.
- [34] Lin, Y.-M., Dimitrakopoulos, C., Jenkins, K.A., Farmer, D.B., Chiu, H.-Y., Grill, A., Avouris, Ph. *100-GHz transistors from wafer-scale epitaxial graphene* (2010) *Science*, 327 (5966), p. 662.
- [35] Kedzierski, J., Hsu, P.-L., Reina, A., Kong, J., Healey, P., Wyatt, P., Keast, C. *Graphene-on-insulator transistors made using C on Ni chemical-vapor deposition* (2009) *IEEE Electron Device Letters*, 30 (7), pp. 745-747.
- [36] Lavrik, N.V., Datskos, P.G. *Femtogram mass detection using photothermally actuated nanomechanical resonators* (2003) *Applied Physics Letters*, 82 (16), pp. 2697-2699.
- [37] Reiner-Rozman, C., Kotlowski, C., Knoll, W. *Electronic biosensing with functionalized rGO FETs* (2016) *Biosensors*, 6 (2), art. no. 17.
- [38] Hess, L.H., Jansen, M., Maybeck, V., Hauf, M.V., Seifert, M., Stutzmann, M., Sharp, I.D., Offenhäusser, A., Garrido, J.A. *Graphene transistor arrays for recording action potentials from electrogenic cells* (2011) *Advanced Materials*, 23 (43), pp. 5045-5049.
- [39] Huang, Y., Yang, H.Y., Ai, Y. *DNA Single-Base Mismatch Study Using Graphene Oxide Nanosheets-Based Fluorometric Biosensors* (2015) *Analytical Chemistry*, 87 (18), pp. 9132-9136.
- [40] Matsumoto, K., Maehashi, K., Ohno, Y., Inoue, K. *Recent advances in functional graphene biosensors* (2014) *Journal of Physics D: Applied Physics*, 47 (9), art. no. 094005.

- [41] Bunch, J.S., Verbridge, S.S., Alden, J.S., Van Der Zande, A.M., Parpia, J.M., Craighead, H.G., McEuen, P.L. *Impermeable atomic membranes from graphene sheets* (2008) *Nano Letters*, 8 (8), pp. 2458-2462.
- [42] Jiang, C., Markutsya, S., Pikus, Y., Tsukruk, V.V. *Freely suspended nanocomposite membranes as highly sensitive sensors* (2004) *Nature Materials*, 3 (10), pp. 721-728.
- [43] Hashimoto, A., Suenaga, K., Gloter, A., Urita, K., Iijima, S. *Direct evidence for atomic defects in graphene layers* (2004) *Nature*, 430 (7002), pp. 870-873.
- [44] Rose, F., Debray, A., Martin, P., Fujita, H., Kawakatsu, H. *Suspended HOPG nanosheets for HOPG nanoresonator engineering and new carbon nanostructure synthesis* (2006) *Nanotechnology*, 17 (20), art. no. 025, pp. 5192-5200.
- [45] Meyer, J.C., Geim, A.K., Katsnelson, M.I., Novoselov, K.S., Booth, T.J., Roth, S. *The structure of suspended graphene sheets* (2007) *Nature*, 446 (7131), pp. 60-63.
- [46] Hamberg, I., Granqvist, C.G. *Evaporated Sn-doped In<sub>2</sub>O<sub>3</sub> films: Basic optical properties and applications to energy-efficient windows* (1986) *Journal of Applied Physics*, 60 (11), pp. R123-R160.
- [47] Granqvist, C.G. *Transparent conductors as solar energy materials: A panoramic review* (2007) *Solar Energy Materials and Solar Cells*, 91 (17), pp. 1529-1598.
- [48] Novoselov, K.S., Fal'ko, V.I., Colombo, L., Gellert, P.R., Schwab, M.G., Kim, K. *A roadmap for graphene* (2012) *Nature*, 490 (7419), pp. 192-200.
- [49] Lee, C., Wei, X., Kysar, J.W., Hone, J. *Measurement of the elastic properties and intrinsic strength of monolayer graphene* (2008) *Science*, 321 (5887), pp. 385-388.
- [50] Han, T.-H., Lee, Y., Choi, M.-R., Woo, S.-H., Bae, S.-H., Hong, B.H., Ahn, J.-H., Lee, T.-W. *Extremely efficient flexible organic light-emitting diodes with modified graphene anode* (2012) *Nature Photonics*, 6 (2), pp. 105-110.
- [51] Kim, K., Bae, S.-H., Toh, C.T., Kim, H., Cho, J.H., Whang, D., Lee, T.-W., Özyilmaz, B., Ahn, J.-H. *Ultrathin organic solar cells with graphene doped by ferroelectric polarization* (2014) *ACS Applied Materials and Interfaces*, 6 (5), pp. 3299-3304.
- [52] Brennan, L.J., Byrne, M.T., Bari, M., Gun'ko, Y.K. *Carbon nanomaterials for dye-sensitized solar cell applications: A bright future* (2011) *Advanced Energy Materials*, 1 (4), pp. 472-485.
- [53] Arias, A.C., MacKenzie, J.D., McCulloch, I., Rivnay, J., Salleo, A. *Materials and applications for large area electronics: Solution-based approaches* (2010) *Chemical Reviews*, 110 (1), pp. 3-24.

- [54] O'Regan, B., Grätzel, M. *A low-cost, high-efficiency solar cell based on dye-sensitized colloidal TiO<sub>2</sub> films* (1991) *Nature*, 353 (6346), pp. 737-740.
- [55] He, Z., Zhong, C., Su, S., Xu, M., Wu, H., Cao, Y. *Enhanced power-conversion efficiency in polymer solar cells using an inverted device structure* (2012) *Nature Photonics*, 6 (9), pp. 591-595.
- [56] Burschka, J., Pellet, N., Moon, S.-J., Humphry-Baker, R., Gao, P., Nazeeruddin, M.K., Grätzel, M. *Sequential deposition as a route to high-performance perovskite-sensitized solar cells* (2013) *Nature*, 499 (7458), pp. 316-319.
- [57] Yin, Z., Wu, S., Zhou, X., Huang, X., Zhang, Q., Boey, F., Zhang, H. *Electrochemical deposition of ZnO nanorods on transparent reduced graphene oxide electrodes for hybrid solar cells* (2010) *Small*, 6 (2), pp. 307-312.
- [58] Yu, D., Yang, Y., Durstock, M., Baek, J.-B., Dai, L. *Soluble P3HT-grafted graphene for efficient bilayer-heterojunction photovoltaic devices* (2010) *ACS Nano*, 4 (10), pp. 5633-5640.
- [59] Li, S.-S., Tu, K.-H., Lin, C.-C., Chen, C.-W., Chhowalla, M. *Solution-processable graphene oxide as an efficient hole transport layer in polymer solar cells* (2010) *ACS Nano*, 4 (6), pp. 3169-3174.
- [60] Gomez De Arco, L., Zhang, Y., Schlenker, C.W., Ryu, K., Thompson, M.E., Zhou, C. *Continuous, highly flexible, and transparent graphene films by chemical vapor deposition for organic photovoltaics* (2010) *ACS Nano*, 4 (5), pp. 2865-2873.
- [61] Zhu, Y., Sun, Z., Yan, Z., Jin, Z., Tour, J.M. *Rational design of hybrid graphene films for high-performance transparent electrodes* (2011) *ACS Nano*, 5 (8), pp. 6472-6479.
- [62] Hu, W., Peng, C., Luo, W., Lv, M., Li, X., Li, D., Huang, Q., and Fan, C. *Graphene-based antibacterial paper* (2010) *ACS Nano* 4, 4317–4323.
- [63] Sanchez, V. C., Weston, P., Yan, A., Hurt, R. H., and Kane, A. B. *A 3-dimensional in vitro model of epithelioid granulomas induced by high aspect ratio nanomaterials* (2011) *Part. Fibre Toxicol.* 8, 17.
- [64] Sun, X., Liu, Z., Welsher, K., Robinson, J. T., Goodwin, A., Zaric, S., and Dai, H. *Nano-graphene oxide for cellular imaging and drug delivery* (2008) *Nano Res.* 1, 203–212.
- [65] Feng, L., Zhang, S., and Liu, Z. *Graphene based gene transfection* (2001) *Nanoscale* 3, 1252–1257.
- [66] Hummers Jr., W.S., Offeman, R.E. *Preparation of graphitic oxide* (1958) *Journal of the American Chemical Society*, 80 (6), p. 1339.

- [67] Hasan, S. A., Rigueur, J. L., Harl, R. R., Krejci, A. J., Gonzalo-Juan, I., Rogers, B. R., and Dickerson, J. H. *Transferable graphene oxide films with tunable microstructures* (2010) ACS Nano 4, 7367–7372.
- [68] Cote, L. J., Kim, F., and Huang, J. *Langmuir-Blodgett assembly of graphite oxide single layers* (2009) J. Am. Chem. Soc. 131, 1043– 1049.
- [69] Pang, Y., Cui, Y., Ma, Y., Qian, H., Shen, X. *Fluorescence quenching of cationic organic dye by graphene: Interaction and its mechanism* (2012) Micro and Nano Letters, 7 (7), pp. 608-612.
- [70] Xu, G.-Q., Xu, P.-W., Shi, D.-J., Chen, M.-Q. *Preparation and cellular imaging of PEG grafted graphene oxide* (2014) Chinese Journal of Inorganic Chemistry, 30 (9), pp. 1994-1999
- [71] Shao, Y., Wang, J., Wu, H., Liu, J., Aksay, I. A., and Lin, Y. *Graphene based electrochemical sensors and biosensors: a review* (2010) Electroanalysis 22, 1027– 1036.
- [72] Shah, S., Yin, P.T., Uehara, T.M., Chueng, S.-T.D., Yang, L., Lee, K.-B. *Guiding stem cell differentiation into oligodendrocytes using graphene-nanofiber hybrid scaffolds* (2014) Advanced Materials, 26 (22), pp. 3673-3680.
- [73] Li, N., Zhang, X., Song, Q., Su, R., Zhang, Q., Kong, T., Liu, L., Jin, G., Tang, M., Cheng, G. *The promotion of neurite sprouting and outgrowth of mouse hippocampal cells in culture by graphene substrates* (2011) Biomaterials, 32 (35), pp. 9374-9382.
- [74] Liu, L.-H., Zorn, G., Castner, D.G., Solanki, R., Lerner, M.M., Yan, M. *A simple and scalable route to wafer-size patterned graphene* (2010) Journal of Materials Chemistry, 20 (24), pp. 5041-5046.
- [75] Fischbein, M.D., Drndić, M. *Electron beam nanosculpting of suspended graphene sheets* (2008) Applied Physics Letters, 93 (11), art. no. 113107.
- [76] Xiong, W., Zhou, Y.S., Hou, W.J., Jiang, L.J., Gao, Y., Fan, L.S., Jiang, L., Silvain, J.F., Lu, Y.F. *Direct writing of graphene patterns on insulating substrates under ambient conditions* (2014) Scientific Reports, 4, art. no. 4892.
- [77] Childres, I., Jauregui, L.A., Tian, J., Chen, Y.P. *Effect of oxygen plasma etching on graphene studied using Raman spectroscopy and electronic transport measurements* (2011) New Journal of Physics, 13, art. no. 025008.
- [78] [www.graphenea.com](http://www.graphenea.com)

- [79] Reina, A., Jia, X., Ho, J., Nezich, D., Son, H., Bulovic, V., Dresselhaus, M.S., Jing, K. *Large area, few-layer graphene films on arbitrary substrates by chemical vapor deposition* (2009) *Nano Letters*, 9 (1), pp. 30-35.
- [80] Bell, D.C., Lemme, M.C., Stern, L.A., Williams, J.R., Marcus, C.M. *Precision cutting and patterning of graphene with helium ions* (2009) *Nanotechnology*, 20 (45), art. no. 455301.
- [81] Han, M.Y., Özyilmaz, B., Zhang, Y., Kim, P. *Energy band-gap engineering of graphene nanoribbons* (2007) *Physical Review Letters*, 98 (20), art. no. 206805.
- [82] Tapasztó, L., Dobrik, G., Lambin, P., Biró, L.P. *Tailoring the atomic structure of graphene nanoribbons by scanning tunnelling microscope lithography* (2008) *Nature Nanotechnology*, 3 (7), pp. 397-401.
- [83] Masubuchi, S., Ono, M., Yoshida, K., Hirakawa, K., MacHida, T. *Fabrication of graphene nanoribbon by local anodic oxidation lithography using atomic force microscope* (2009) *Applied Physics Letters*, 94 (8), art. no. 082107.
- [84] Lu, X., Yu, M., Huang, H., Ruoff, R.S. *Tailoring graphite with the goal of achieving single sheets* (1999) *Nanotechnology*, 10 (3), pp. 269-272.
- [85] Ferrari, A.C., Basko, D.M. *Raman spectroscopy as a versatile tool for studying the properties of graphene* (2013) *Nature Nanotechnology*, 8 (4), pp. 235-246.
- [86] Nemes-Incze, P., Osváth, Z., Kamarás, K., Biró, L.P. *Anomalies in thickness measurements of graphene and few layer graphite crystals by tapping mode atomic force microscopy* (2008) *Carbon*, 46 (11), pp. 1435-1442.
- [87] Roddaro, S., Pingue, P., Piazza, V., Pellegrini, V., Beltram, F. *The optical visibility of graphene: Interference colors of ultrathin graphite on SiO<sub>2</sub>* (2007) *Nano Letters*, 7 (9), pp. 2707-2710.
- [88] Si, Y., Samulski, E.T. *Synthesis of water soluble graphene* (2008) *Nano Letters*, 8 (6), pp. 1679-1682.
- [89] Unarunotai, S., Murata, Y., Chialvo, C.E., Kim, H.-S., MacLaren, S., Mason, N., Petrov, I., Rogers, J.A. *Transfer of graphene layers grown on SiC wafers to other substrates and their integration into field effect transistors* (2009) *Applied Physics Letters*, 95 (20), art. no. 202101
- [90] Unarunotai, S., Koepke, J.C., Tsai, C.-L., Du, F., Chialvo, C.E., Murata, Y., Haasch, R., Petrov, I., Mason, N., Shim, M., Lyding, J., Rogers, J.A. *Layer-by-layer transfer of multiple, large area sheets of graphene grown in multilayer stacks on a single SiC wafer* (2010) *ACS Nano*, 4 (10), pp. 5591-5598.

- [91] Caldwell, J.D., Anderson, T.J., Culbertson, J.C., Jernigan, G.G., Hobart, K.D., Kub, F.J., Tadjer, M.J., Tedesco, J.L., Hite, J.K., Mastro, M.A., Myers-Ward, R.L., Eddy Jr., C.R., Campbell, P.M., Gaskill, D.K. *Technique for the dry transfer of epitaxial graphene onto arbitrary substrates* (2010) ACS Nano, 4 (2), pp. 1108-1114.
- [92] Lin, Y.-C., Jin, C., Lee, J.-C., Jen, S.-F., Suenaga, K., Chiu, P.-W. *Clean transfer of graphene for isolation and suspension* (2011) ACS Nano, 5 (3), pp. 2362-2368.
- [93] Song, J., Kam, F.-Y., Png, R.-Q., Seah, W.-L., Zhuo, J.-M., Lim, G.-K., Ho, P.K.H., Chua, L.-L. *A general method for transferring graphene onto soft surfaces* (2013) Nature Nanotechnology, 8 (5), pp. 356-362.
- [94] Han, Y., Zhang, L., Zhang, X., Ruan, K., Cui, L., Wang, Y., Liao, L., Wang, Z., Jie, J. *Clean surface transfer of graphene films via an effective sandwich method for organic light-emitting diode applications* (2014) Journal of Materials Chemistry C, 2 (1), pp. 201-207.
- [95] ang, Y., Zheng, Y., Xu, X., Dubuisson, E., Bao, Q., Lu, J., Loh, K.P. *Electrochemical delamination of CVD-grown graphene film: Toward the recyclable use of copper catalyst* (2011) ACS Nano, 5 (12), pp. 9927-9933.
- [96] Kim, K.S., Zhao, Y., Jang, H., Lee, S.Y., Kim, J.M., Kim, K.S., Ahn, J.-H., Kim, P., Choi, J.-Y., Hong, B.H. *Large-scale pattern growth of graphene films for stretchable transparent electrodes* (2009) Nature, 457 (7230), pp. 706-710.
- [97] Lin, W.-H., Chen, T.-H., Chang, J.-K., Taur, J.-I., Lo, Y.-Y., Lee, W.-L., Chang, C.-S., Su, W.-B., Wu, C.-I. *A direct and polymer-free method for transferring graphene grown by chemical vapor deposition to any substrate* (2014) ACS Nano, 8 (2), pp. 1784-1791.
- [98] Lock, E.H., Baraket, M., Laskoski, M., Mulvaney, S.P., Lee, W.K., Sheehan, P.E., Hines, D.R., Robinson, J.T., Tosado, J., Fuhrer, M.S., Hernández, S.C., Walton, S.G. *High-quality uniform dry transfer of graphene to polymers* (2012) Nano Letters, 12 (1), pp. 102-107.
- [99] Yoon, T., Shin, W.C., Kim, T.Y., Mun, J.H., Kim, T.-S., Cho, B.J. *Direct measurement of adhesion energy of monolayer graphene as-grown on copper and its application to renewable transfer process* (2012) Nano Letters, 12 (3), pp. 1448-1452.





# Chapter 2

## 2.1 Residuals in graphene wet-transferred with polymers

Polymer supported transfer methods are largely used for graphene transfer, especially for CVD graphene. The metal substrate, which is used as catalyst during the synthesis, typically is not desired for the final application and has to be removed. During this step, graphene has to be supported to avoid breakage. As seen in the previous Chapter, there are several polymers used for this purpose, but PMMA is the most diffused because of the easy handling and processing. Unfortunately, due to the high molecular weight and high viscosity, PMMA residuals remain on graphene after its removal. This represents an unsolved problem [1], because residuals bind covalently on graphene defects and remain after removal in solvents or after thermal processes [2]. Graphene defects sites facilitate the adsorption of carboxyl functional groups and oxidation, as observed also for others carbon-based materials, such as carbon nanotubes (CNTs) [3]. These contaminants affect the electrical properties of transferred graphene, with p-doping effect [4] and impurity scattering [5], which reduces mobility.

Thermal processes such as annealing are largely used for removing of PMMA residuals [6], but a complete removal of covalently bound polymeric residues remains limited. Other techniques, such as chemical cleaning have been proposed: chloroform can be used as solvent to replace acetone for PMMA removal [7], but causes spontaneous intercalation of chloroform beneath the graphene basal plane and leads to strong graphene hole doping. Moreover, mechanical cleaning by AFM tip has been introduced [8], but is extremely time consuming because it is based on the scratch of several hundred nm of polymer only moving the AFM tip. Furthermore, low-density, inductively coupled plasma (ICP) could also be used to remove polymeric residues [9], but there is the risk to create large defects or holes during plasma processing.

It should also consider that graphene before transfer is not perfectly flat, rather it replicates the morphology of the growth substrate. Therefore, the transfer on a much flatter substrate, like a silicon wafer, results in a partial adhesion and the unattached regions are keener to break when the polymer is dissolved. In order to prevent cracks, the use of a second layer of

PMMA has been proposed [10] but the thermal treatment of PMMA leads to the creation of defects and in addition the residues are not completely eliminated [11].

I tested graphene wet transfer with PMMA in different configurations: supported graphene transferred on several substrates (silicon, silicon dioxide, titania), and suspended graphene (continuous or patterned). CVD graphene on Cu foil is purchased by Graphenea S.A. [12]. After the transfer, all the fabricated samples are annealed in UHV at 250 °C for 1 hour to remove as much as possible PMMA residuals. In Fig. 2.1 the different tested configurations are shown.

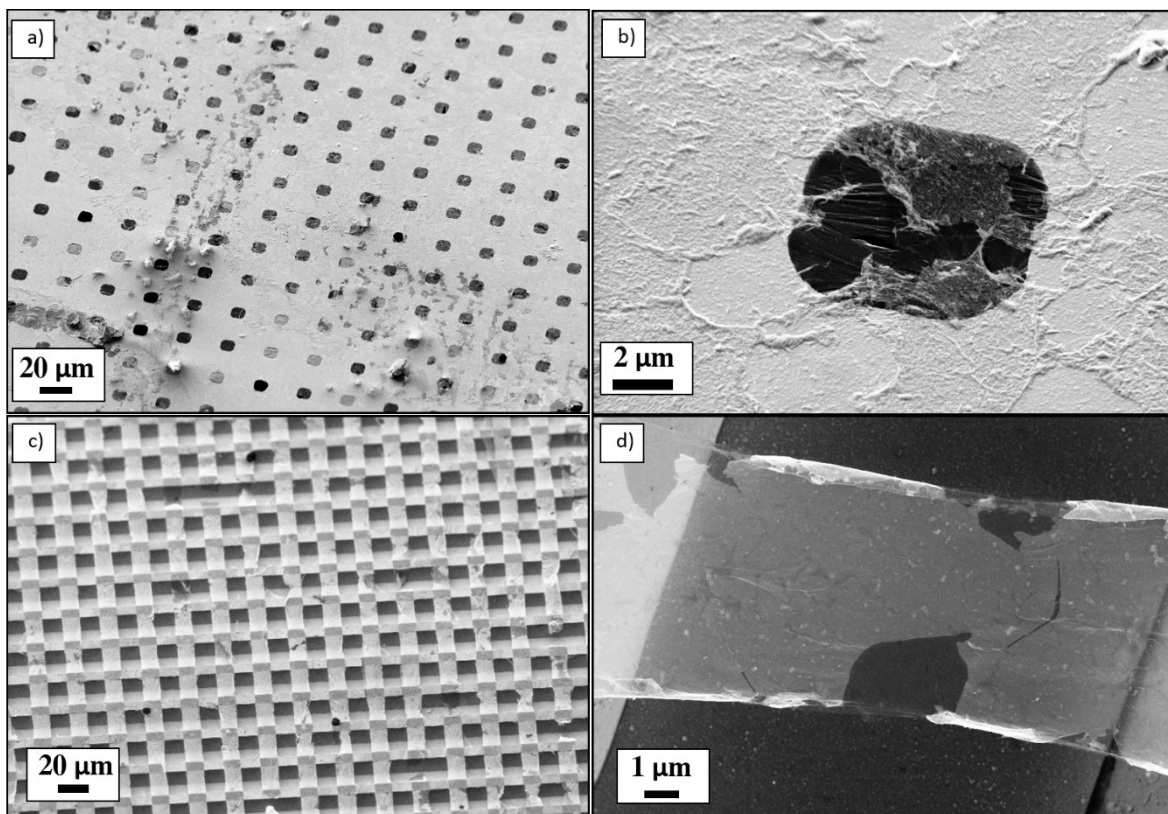


Fig. 2.1: SEM images of different configurations of graphene transferred with PMMA: a) suspended graphene on cavities obtained in a  $\text{Si}_3\text{N}_4$  membrane 200 nm-thick. Darker holes are not covered by graphene because it breaks during transfer or PMMA removal; b) detail of one of the cavities shown in a) in which PMMA residuals are clearly visible; c) suspended graphene patterned with plasma oxygen in lines with length and periodicity of 10  $\mu\text{m}$  and 20  $\mu\text{m}$ , respectively, and transferred on an array of lines fabricated in a bulk silicon substrate; d) one of the graphene lines shown in c). All the images are obtained detecting secondary electrons with primary electron energy set at 3 kV, except for d) which is obtained at 10 kV. [Matruglio *et al.*, unpublished].

The contaminations decrease the electron transparency of graphene layers. In fact, Fig. 2.1a and b shows clear polymer residuals that persist after PMMA removal and temperature treatment. In Fig. 2.1c the transparent regions suggest a good removal of the polymer, but the major part of the surface is not transparent, suggesting polymer contamination. As shown in Fig. 2.1d, these contaminants seem to attach the back side of the graphene stripe and this is probably originated during the polymer removal. The solvent removes the polymer from graphene and due to the geometry of the substrate, which is patterned with open lines, the solvent can diffuse in the cavities and some residuals can reattach on the back side of the suspended graphene.

## **2.2 A novel wet transfer method using titanium for polymer-free transfer**

Several metals have been investigated as alternative materials to polymers for graphene transfer support. In particular, palladium [13] and gold [14] have been used to transfer epitaxially grown graphene from SiC, but the number of introduced defect is very high and the electrical properties poor. Gold has been also used for the transfer of CVD graphene for the fabrication of G-FETs [15] but doping effect has been observed. Recently, an interesting approach to improve the cleaning of the surface has been provided by the use of a sacrificial titanium (Ti) layer deposited between graphene and PMMA [16]; the thin layer is deposited via e-beam evaporation and then removed in a hydrofluorhydric acid (HF) solution. The Ti coating avoids the direct contact of PMMA with the graphene. Graphene characterization (Raman spectroscopy and x-ray photoelectron spectroscopy) shows a clean and not damaged graphene after transfer and after PMMA and Ti removal. However, the Ti layer can be applied only to the exposed graphene side, while the side in contact with the growth substrate remains unprotected: this results in big limitations when suspended graphene structures are required, because the back side should be contaminated during the solvent assisted PMMA removal.

To solve the problem, I developed a clean, polymer-free transfer method for commercial CVD graphene suitable for both supported and suspended graphene structures. The method involves the deposition of a 15 nm-thick layer of Ti then dissolved in a HF solution, avoiding the use of any polymer, preventing contamination on the back graphene side due to its dissolution in case of suspended structures. In the next sections details about the novel

method will be provided, with particular attention on the microfabrication processes and on the characterization of the produced samples.

### 2.2.1 Fabrication of the samples

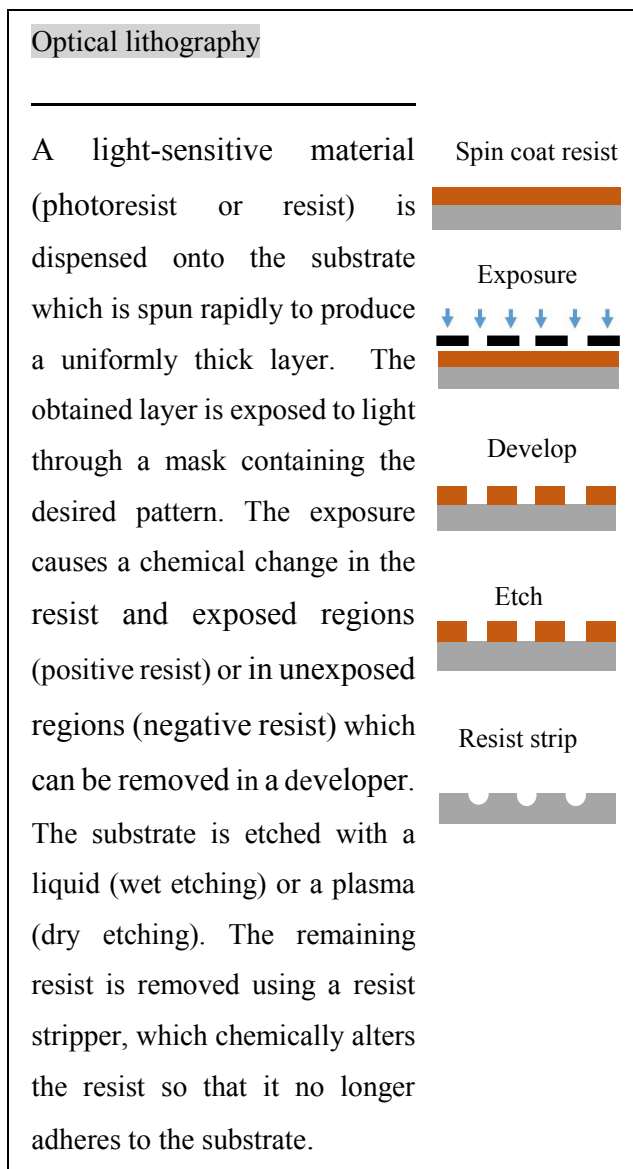
In order to obtain suspended graphene structures, I produced several microstructured silicon substrates in which micrometric gratings are fabricated.

In details, a clean bulk silicon substrate has been patterned by classical optical lithography technique.

MICROPOSIT® S1803 photoresist is patterned with lines of width and periodicity of 10  $\mu\text{m}$  and 20  $\mu\text{m}$ , respectively. The grooves are deep etched in order to ensure full access to the etching solutions. Inductively coupled plasma-reactive ion etching (ICP-RIE) is used to transfer the pattern in the bulk silicon; ICP BOSCH® like process (gases:  $\text{SF}_6$ ,  $\text{C}_4\text{F}_8$ , Ar) is set to obtain a depth of 10  $\mu\text{m}$ , followed by  $\text{O}_2$  plasma so as to remove the resist mask. Piranha solution for 15 minutes ( $\text{H}_2\text{SO}_4:\text{H}_2\text{O}_2$  7:3 ratio in volume) allows removing any carbon residuals from the substrate.

Commercial CVD grown graphene on Cu foils is used for all the prepared

samples [12]. SEM images of the as-grown graphene are shown in Fig. 2.2.



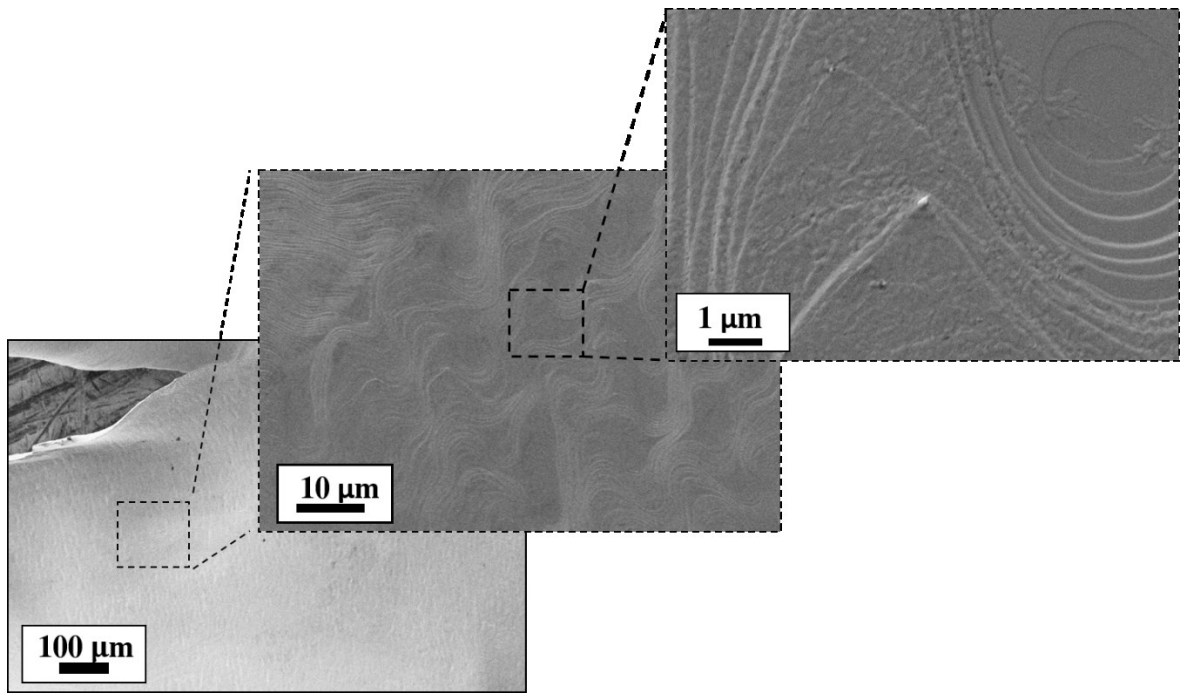


Fig. 2.2: SEM images of graphene as-received. The two zooms show magnified views in which Cu steps are visible.

Fig. 2.2 show a Cu foil not perfectly flat and steps are clearly visible. Graphene follows the copper surface morphology when growing on Cu. From the product datasheet, the grain size is up to 10  $\mu\text{m}$  [17].

**BOSCH® process**

Etch process cycles between etch and deposition steps, to achieve vertical etch profiles. Sulphur hexafluoride ( $\text{SF}_6$ ) is used to provide fluorine for silicon etching. This molecule will readily break up in high-density plasma to release free radical fluorine. The sidewall passivation and mask protection is provided by octafluorocyclobutane ( $\text{C}_4\text{F}_8$ ) that breaks open to produce  $\text{CF}_2$  and longer chain radicals in the high-density plasma. These readily deposit as fluorocarbon polymer on the samples being etched.

In order to verify the method, I compared two transfer protocols: a conventional one involving the use of a thermoplastic polymer (mr-I 7020) and a second one using Ti. The selection of mr-I 7020 instead of the commonly used PMMA is motivated by its higher solubility in acetone that allows, in my experience, the production of cleaner graphene surfaces. In effect, Fig. 2.3a shows a SEM image of graphene layer transferred with a 250 nm-

thick sacrificial layer of PMMA (Ar- P669.04, ALLRESIST GmbH) on a SiO<sub>2</sub>/Si substrate. Graphene is patterned by classical UV lithography and dry etching techniques via oxygen plasma in line of width and periodicity of 10 μm and 20 μm, respectively.

The SEM characterization is performed after the removal of PMMA in cold acetone for 5 minutes and after annealing at 250 °C for 1 hour. In comparison, Fig.2.3b shows a continuous graphene layer transferred with a 250 nm-thick sacrificial layer of mr-I 7020 on SiO<sub>2</sub>/Si substrate patterned with the same grating of the previous sample. After the transfer, mr-I 7020 is removed in cold acetone for 5 minutes and annealed at 250 °C for 1 hour as before.

#### Oxygen plasma etching

Used to remove layers of materials to create patterns on the surface. A resist is used as etching mask for the plasma. High power radio waves are applied in a vacuum chamber and oxygen is channeled into it. The low pressure of the vacuum chamber causes the oxygen molecules to ionize, forming plasma. The plasma etches the graphene and does not etch the surface below the mask.

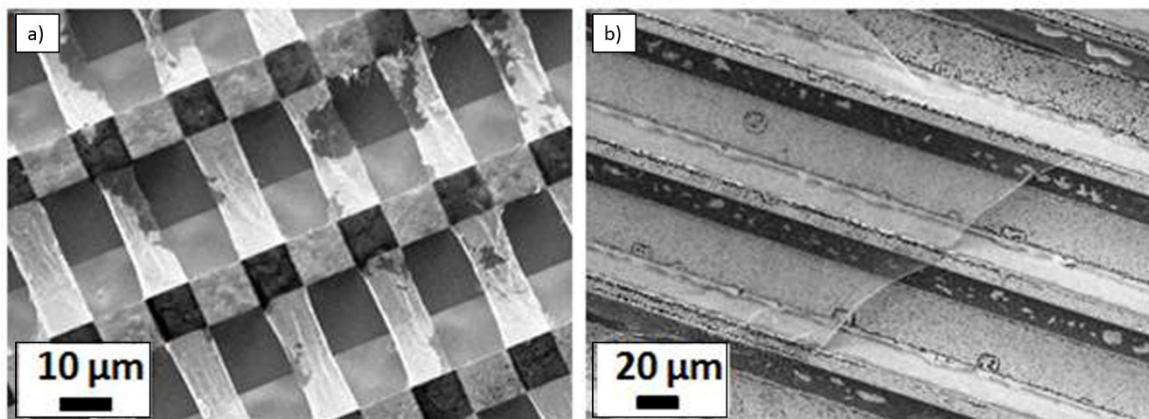


Fig. 2.3: SEM images of graphene transferred on SiO<sub>2</sub>/Si substrate with: a) PMMA; b) mr-I 7020. Both the images are obtained with a secondary electron detector at 5 kV of energy.

As shown in Fig. 2.3a, PMMA is only partially removed and some redeposits can be seen. The transparent regions are the only portions in which PMMA is totally removed and graphene results nearly transparent to the electrons; on the contrary, white parts are heavily contaminated by PMMA residuals. I observed that even by increasing of the stripping time, PMMA residues are present. On the other hand, Fig. 2.3b shows a graphene layer homogeneous and transparent with no evident signs of contamination, leading to state that the mr-I 7020 is the best polymer for my purposes.

To develop the two protocols, I started from the same graphene/Cu foil in order to use graphene in the same initial condition. For the first sample, labeled PG (Polymer-Graphene), a layer of 250 nm of mr-I 7020 (Micro Resist technology GmbH) is spin coated on graphene. The Cu foil is subsequently etched overnight in a Cu etching solution ( $\text{FeCl}_3\text{:H}_2\text{O}$  3:7 ratio in volume). After the etching process, graphene is rinsed in DI water several times; the graphene transfer is performed by fishing graphene into the water directly on the patterned substrate. Water is left to evaporate at room temperature for 2 h and mr-I 7020 is dissolved in cold acetone for 5 min. Critical point drying (CPD) is performed in order to avoid the collapse of suspended graphene structures. Fig. 2.4 shows three pictures taken during the etching process of Cu.

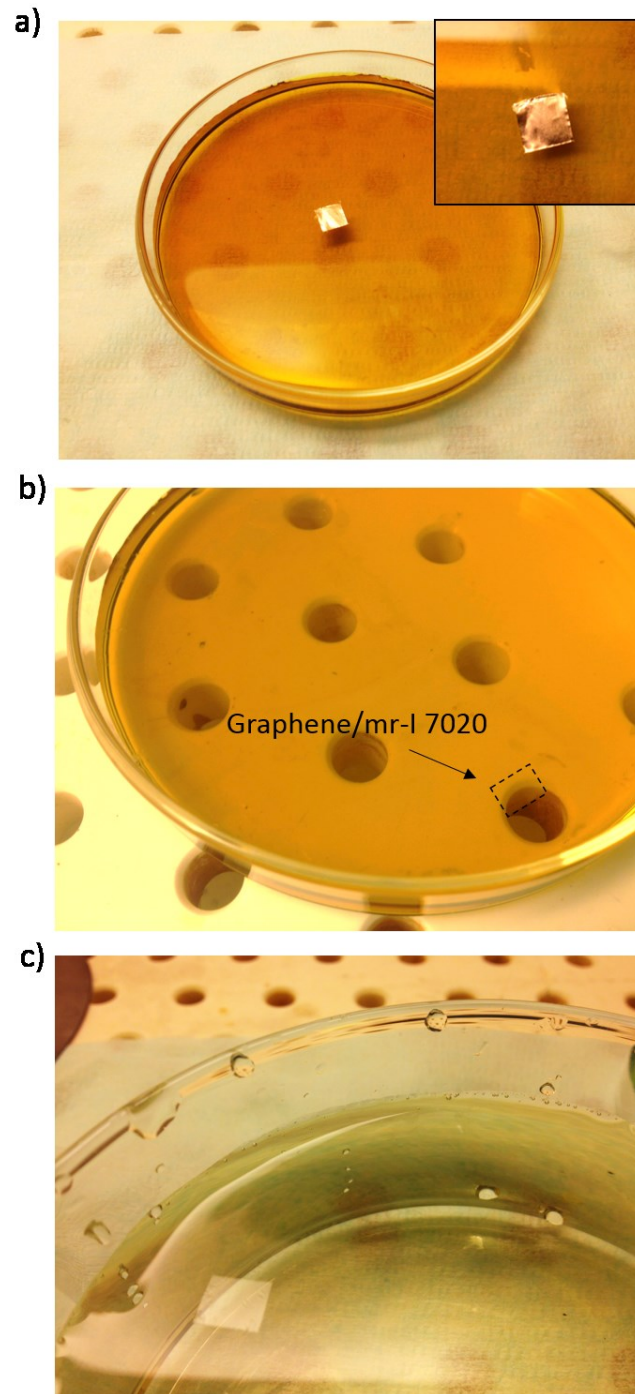


Fig. 2.4: Cu etching process: a) the mr-I 7020/graphene/Cu membrane floating on Cu etching solution; the inset shows a magnification in which the piece is clearly visible; b) after etching of the metal, polymer/graphene membrane is transparent to human eye; c) polymer/graphene floating on DI water for washing.



For the second sample, labeled MG (Metal-Graphene), I used a novel approach involving the deposition via electron-beam evaporation of a 15 nm-thick Ti layer on graphene with rate of 2 nm/s: the thickness was selected to be sufficient for supporting the graphene monolayer and preventing breakage. A scheme of the process is shown in Fig. 2.5. The transfer is leaded following the same protocol of the previous sample. Ti layer is removed in 1:10 HF:DI water solution for 2 min. CPD is performed also in this case in order to avoid the collapse of the suspended graphene structures.

### Critical point drying

Compounds at the critical point can be converted into the liquid or gaseous phase without crossing the liquid/gas interfaces, avoiding the damaging effects of surface tension forces. Dehydration of samples using the critical point of water is not feasible since it lies at 373 °C and 228 bar. Water can be replaced with liquid CO<sub>2</sub>, whose critical point lies at 31°C and 74.

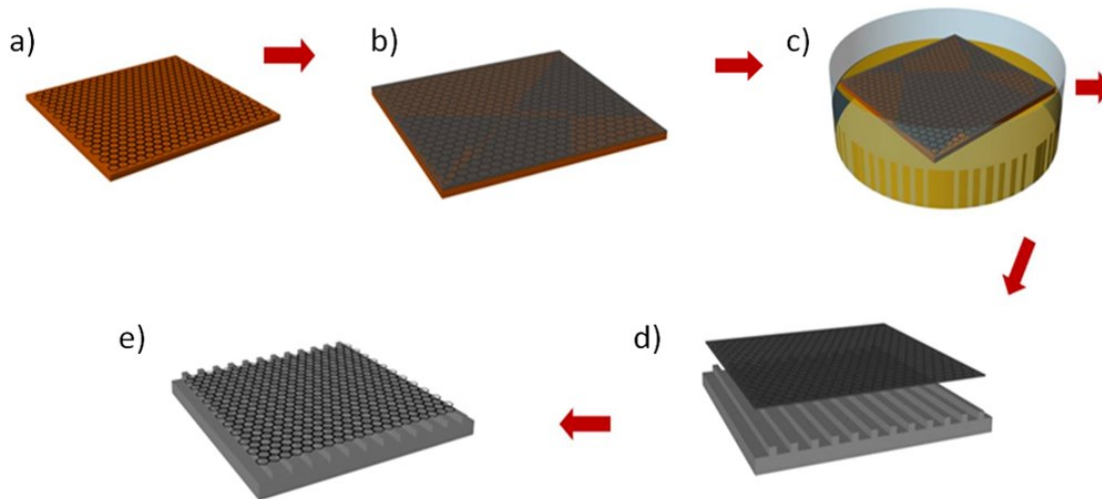
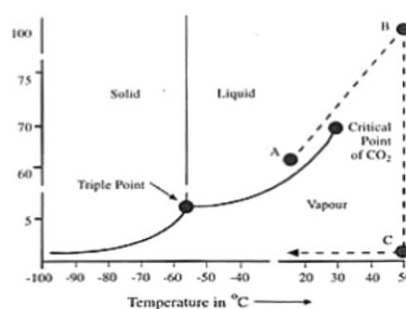


Fig. 2.5: Scheme of Ti-supported graphene transfer. a) CVD graphene on Cu foil; b) e-beam evaporation of 15 nm of Ti layer; c) wet etching of Cu; d) Gr/Ti transfer on Si substrate; e) graphene on Si substrate after Ti etching.

### 2.2.2 Characterization of the samples

To have a first indication of the graphene cleanliness after transfer, SEM characterization of both samples has been performed and images are shown in Fig. 2.6.

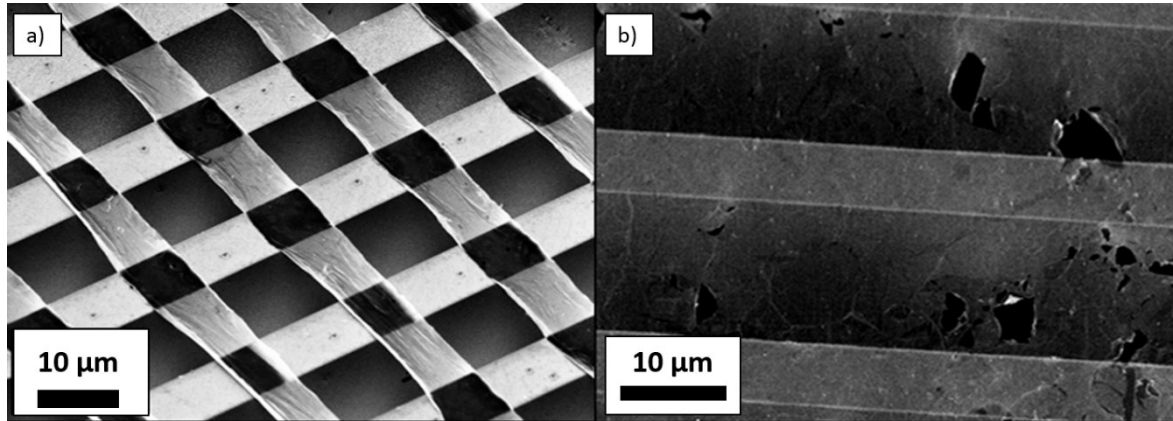


Fig. 2.6: SEM images of suspended graphene of: (a) PG method using mr-I 7020 obtained with a secondary electrons detector; (b) MG method using a layer of Ti obtained with an in-lens detector: visible defects are propagated at grain boundaries. Both the images are obtained with primary electron energy set at 5 kV.

For the PG sample (Fig. 2.6a) graphene is patterned in stripes 10 μm-long with plasma oxygen. The stripes are not transparent and this suggests strong contaminations due to acetone and polymer visible on the back surface of suspended part. On the other hand, the MG sample (Fig. 2.6b) shows a clean and transparent graphene and results in a continuous film on the scale of 10 μm, which is the size of the crystalline grain obtained by CVD [17]. Above this size the formation of defects and cracks are observed due to the breaking at the grain boundaries, as already reported in literature [18, 19].

To have a more precise indication about contaminations, we performed Raman spectroscopy on both PG and MG samples. The Raman measurements were performed in the reflection geometry on an inverted optical microscope (Axiovert 200, Zeiss) coupled with a 750 mm long spectrometer (Shamrock SR-750, Andor Technology plc). CW laser with the excitation wavelength of 532 nm (Cobolt Samba, 50 mW) was used. The light was focused on the sample by a 100x air objective (NA 0.8, EC Epiplan, Zeiss), resulting in a ~0.4 μm diameter laser spot. The laser power on the sample was controlled by variable neutral density filter and kept at 1 mW. Laser scanning confocal microscopy was performed

before the Raman measurements. The representative Rayleigh images of PG and MG samples are shown in Fig. 2.7a and b, respectively. Fig. 2.7c shows the Raman spectra of single-layer graphene CVD grown on Cu foil measured for different steps of transferring process: i) as received; ii) covered by Ti layer; iii) transferred using the Ti sacrificial layer; iv) transferred using mr-I 7020 sacrificial layer.

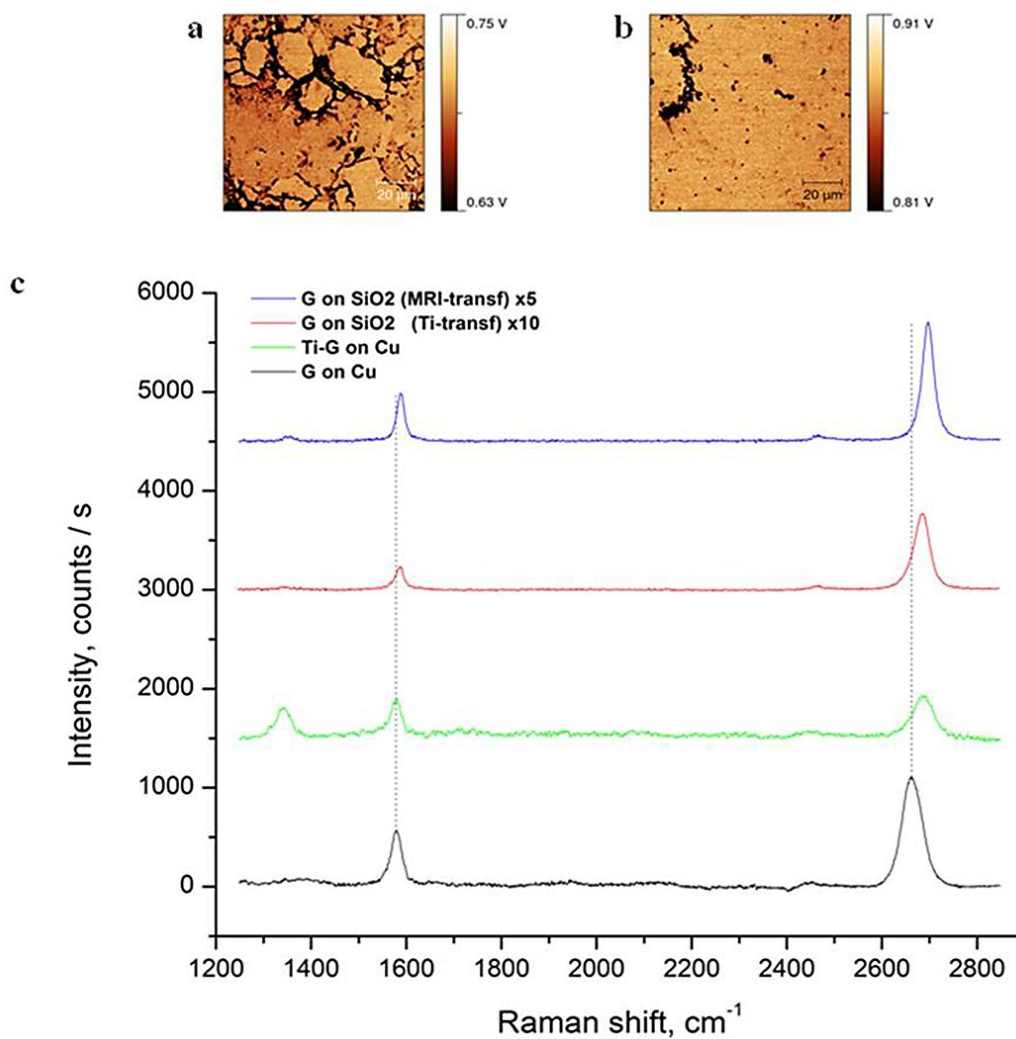


Fig. 2.7: Rayleigh images of (a) PG sample and (b) MG sample; demonstrating more uniform graphene layer in case of (b); (c) Raman spectra of as-grown graphene acquired directly on Cu foil (black), covered by 15 nm thick Ti layer (green), and transferred on  $\text{SiO}_x/\text{Si}$  substrate using Ti (red) or mr-I 7020 (blue). The vertical black dotted lines are displayed for visual guidance and represent the positions of the G- and 2D-peaks of graphene.

The reflectivity images give an indication about the uniformity of the surface: in case of MG sample, graphene appears more uniform and less contaminated respect to PG sample. About Raman spectra, the positions of the G and 2D peaks of graphene on Cu foil are centered at  $1580\text{ cm}^{-1}$  and at  $2665\text{ cm}^{-1}$ , and the 2D/G ratio is about 2. This is a good indication of high-quality monolayer graphene, as compared with the values reported in literature [20, 21]. The D peak gives indication of defects which can be due to breaks, grain boundaries, and lattice defects [22]; in this case, no distinguishable D peak is observed for graphene on Cu foil testifying its high quality; on the contrary an intense D peak is observed when 15 nm-thick Ti layer is deposited on graphene indicating the formation of defects after Ti deposition. The few quantitative differences observed (different G/2D ratio or the position of the 2D peak) can be justified observing that different substrates (metal vs dielectric ones) interact in a different way with graphene so provide different Raman's responses. Interestingly, after the removal of the Ti layer, graphene appears to recover the properties of the as grown one, as the position of the 2D peak remains the same; moreover, the D peak is again negligible testifying that all the defects induced by the Ti deposition are not permanent. In PG sample, D peak is more intense, 2D/G ratio is lower, and the position of the 2D peak is upshifted in comparison with MG sample. All these facts indicate that polymer traces are present on the surface of graphene after the removal while Ti-supported transfer is a cleaner approach.

To have a chemical composition of the graphene surface, we performed x-ray photoelectron spectroscopy (XPS) and X-ray absorption spectroscopy (XAS) at the CNR BACH beamline at Elettra synchrotron radiation facility in Trieste (Italy). The samples were annealed in UHV conditions for 1 hour at  $320^{\circ}\text{C}$  and with a flash at  $380^{\circ}\text{C}$  with a base pressure  $\leq 10^{-9}$  mbar. XPS spectra of C1s core level were acquired using an excitation energy set to 370 eV and a VG-Scienta R3000 hemispherical analyzer, working with an overall energy resolution of 0.2 eV. The C1s XPS spectra for PG and MG samples are shown in Fig. 2.8.

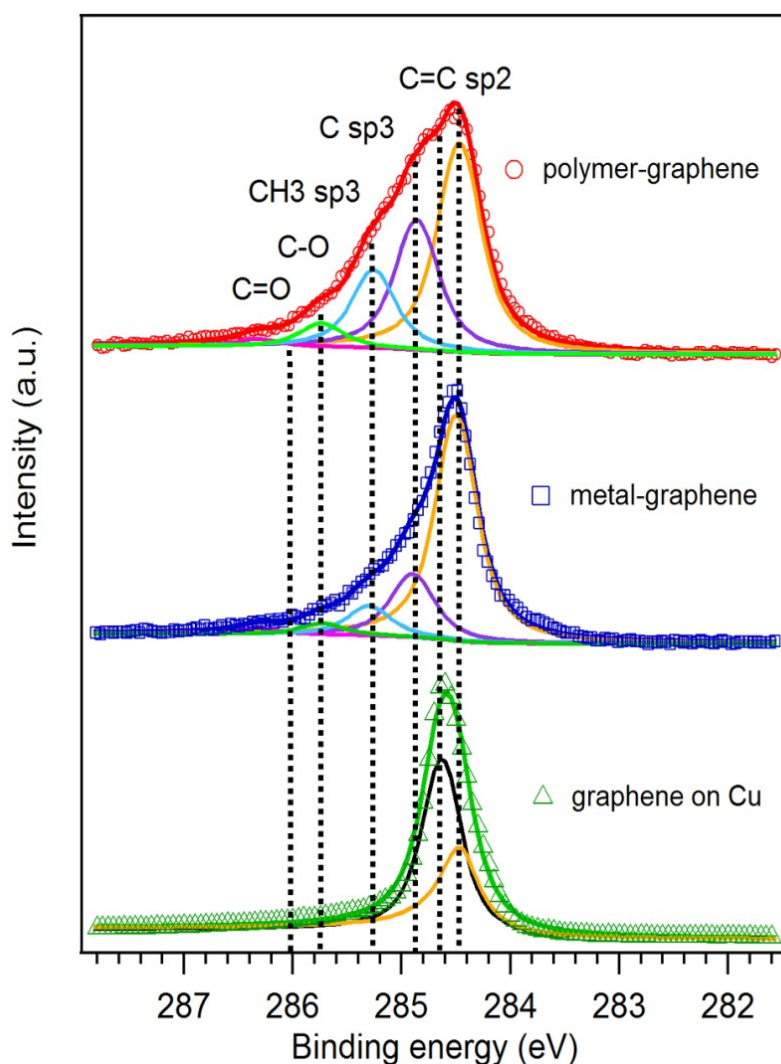


Fig. 2.8: C1s XPS spectra of PG (red curve), MG (blue curve) and graphene on Cu as grown (green curve).

C1s peaks are fitted by a Voigt function, a symmetric convolution of Lorentzian lifetime and Gaussian instrumental broadening, after the subtraction of Shirley background to account for the inelastic photoelectrons. The main peak at 284.5 eV corresponds to the  $sp^2$  carbon (C=C), which is distinctive of the pristine graphene. The presence of components at higher binding energy (BE) is a substantial signal of  $sp^3$  hybridization, and other carbon functionalities, such as C–O and C=O [23, 24] that can be due to physisorbed hydrocarbons. Two different components at 284.8 and 285.3 eV are ascribed to  $sp^3$  species. More precisely, the peak at 284.8 eV is assigned to  $sp^3$  amorphous carbon and defects and could be due to the presence of grain boundaries and lattice defects [1], and also to defects introduced

during the transfer mechanism [10] that can cause the formation of hydrogenated species at the boundaries, such as CH<sub>3</sub> groups (component at 285.3 eV) [11]. In PG sample the presence of hydrocarbon contaminants from polymer residuals further concurs to increase the relative intensity of these components. Peaks at higher BE at 285.8 eV and 286.3 eV correspond to C-O and to C=O bonds, respectively; these oxidized states are given by the presence of chemisorbed oxygen that can be due to the prolonged exposure to atmospheric agents or to the transfer implemented in air [25]. Considering the ratio of the peak areas for each sample, these results show that in PG sample the peaks due to the sp<sup>3</sup> carbon and oxidized species (C-O, C=O) are more than twice as large than those obtained for MG one, suggesting that residues of polymer remain on graphene. Indeed, MG presents a lower contribution due to sp<sup>3</sup>, C=O and C-O components, evidencing a sharp sp<sup>2</sup> carbon peak at 284.5 eV, which is distinctive of good quality pristine graphene. The obtained spectra are compared with the C1s spectrum of as-grown graphene on Cu by CVD (green curve); this spectrum presents two components, the dominant one at 284.65 eV is the fingerprint of as-grown graphene on Cu that is shifted to higher BE with respect to graphene transferred on a substrate because of the stronger interaction with Cu that leads to n-doping as reported in literature [26]; the second feature at 284.65 eV could be associated to a weakly interacting component of graphene with Cu as a consequence of the possible decoupling between Cu and graphene in defected sites due to atmospheric agent exposure [26]. The position of the peaks and the corresponding areas are summarized in Table 1 for all samples.

	C sp <sup>2</sup> (C = C)		C sp <sup>3</sup> (amorphous carbon)		C sp <sup>3</sup> (CH <sub>3</sub> )		C-O		C=O	
	Position (eV)	Area (%)	Position (eV)	Area (%)	Position (eV)	Area (%)	Position (eV)	Area (%)	Position (eV)	Area (%)
<b>Ti</b>	284.5	66.3	284.8	19.3	285.3	9.0	285.8	3.5	286.3	1.9
<b>mr-I</b>	284.5	46.7	284.8	28.9	285.3	17.4	285.8	5.3	286.3	1.7
<b>Cu</b>	284.5	284.65	36.3	63.7	-	-	-	-	-	-

Tab. 1: Positions (eV) e areas (%) of peaks characteristic of C1s for MG, PG and graphene on Cu as grown.

All the performed characterizations indicate a cleaner and less defected graphene in case of Ti transfer respect the use of polymer.

In order to evaluate the graphene arrangement on the substrate after transferring, we performed polarization dependent C K-edge near edge x-ray absorption fine structure (NEXAFS). Polarization-dependent NEXAFS gives information on the orbital hybridization and orientation of the graphene layer transferred on the substrate. C K-edge NEXAFS were measured in partial electron yield mode (PEY) recording C KVV Auger using the electron energy analyzer fixed at the kinetic energy of 261 eV. Two different angles between polarization vector and surface plane were measured: normal-incidence geometry ( $\Theta = 0^\circ$ , s-polarization) and near-grazing incidence geometry ( $\Theta = 60^\circ$ , p-polarization). Fig. 2.9 shows the spectra obtained on MG sample after the removal of the metal.

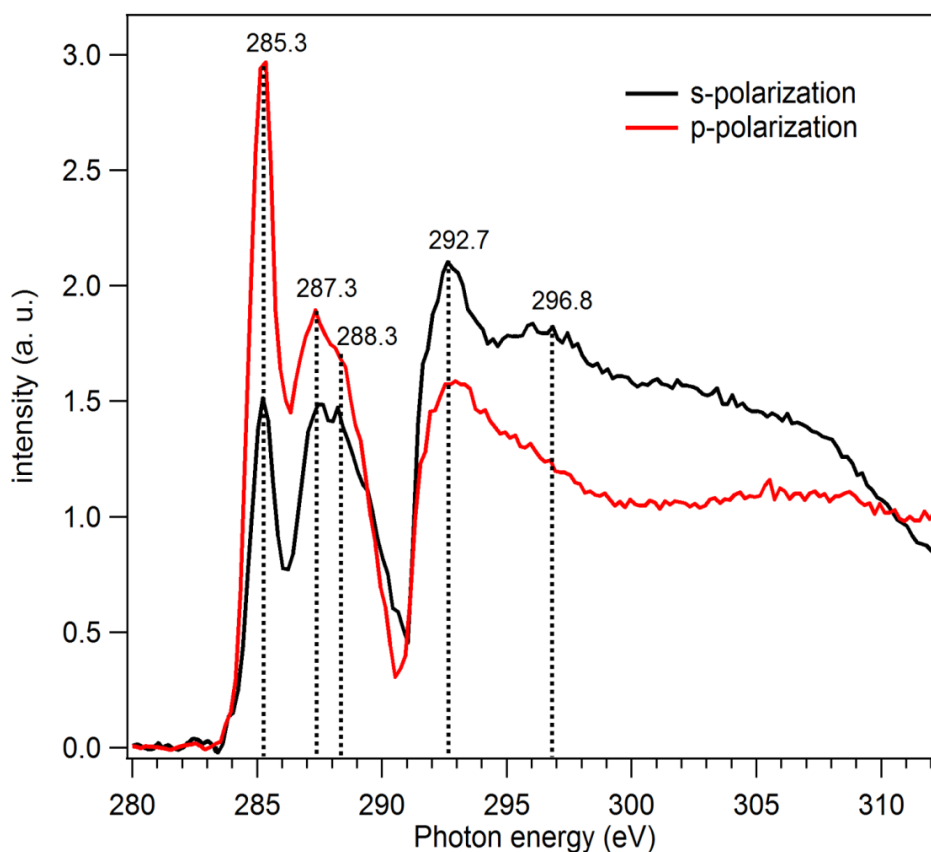


Fig. 2.9: Polarization-dependent NEXAFS obtained on MG sample after the etching of Ti.

The main absorption peak selected with p-polarization corresponds to  $\pi^*$  states (285.3 eV) of  $sp^2$  carbon network, while the continuous absorption at higher photon energies is assigned

to  $\sigma^*$  states (292.7 eV). The polarization dependence shows that the  $\pi^*$  states are suppressed using s-polarized light, evidencing the presence of a nearly flat graphene layer. The other features (287.3, 288.3 and 296.8 eV) could derive from the presence of CO bonds due to the substrate, because of the presence of some defects or breaks in the graphene layer.

### **2.2.3 Analysis of the metal residuals after titanium removal**

Once confirmed the lower level of contaminants and defects introduced by the Ti transfer, remains to analyze if metal residues are present on graphene after Ti removal. In order to evaluate this, XAS spectra at the  $L_{23}$  edge of Ti and K edge of F were performed in total electron (TEY) method. Fig. 2.10a shows the spectrum of Ti  $L_{23}$ -edge XAS and where no traces of Ti can be observed; a typical Ti spectrum is plotted (dashed line) taken from reference [27] for comparison. We also investigated the presence of Fluorine (F) residues which could result from the HF solution: F K-edge XAS spectrum is shown in Fig. 2.10b: also in this case no F traces are present on graphene. A F 1s edge taken on a  $\text{CaF}_2$  thick film with deposition of 1.2 nm of  $\text{MnF}_2$  (dashed line) taken from reference [28] is plotted for comparison, demonstrating our approach as an alternative for an ultraclean graphene transfer method.



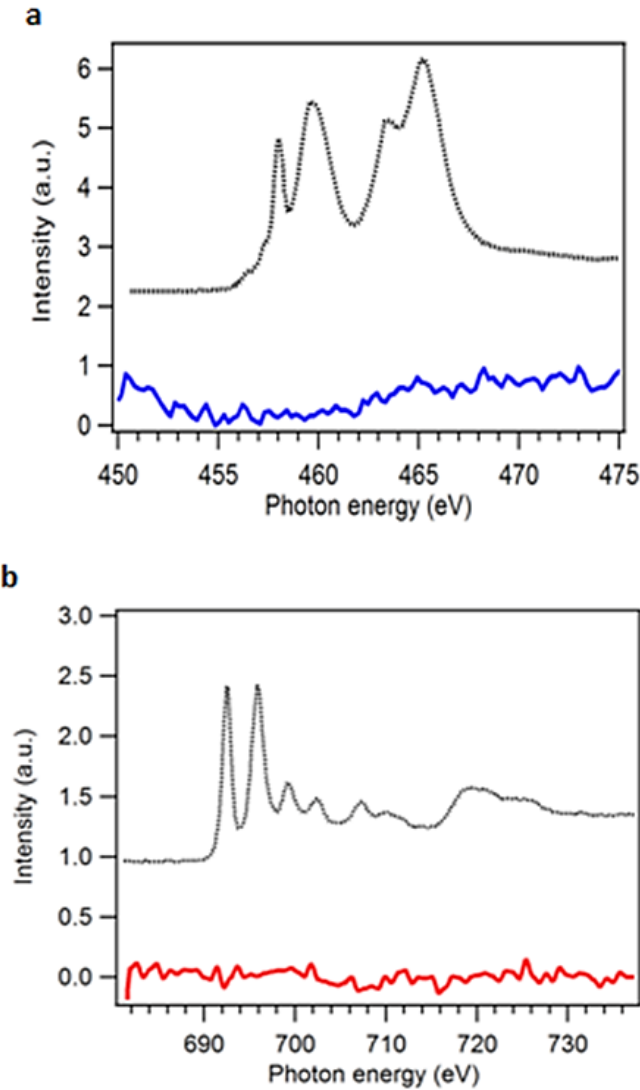


Fig. 2.10: XAS spectra of a) Ti L<sub>23</sub>-edge of MG sample (blue line) compared with Ti L<sub>23</sub> obtained on graphene transferred on TiO<sub>2</sub> (dashed line) taken from reference [27]; b) F k-edge on MG after Ti etching in HF (red line) compared with F 1s edge taken on a CaF<sub>2</sub> thick film after deposition of 1.2 nm of MnF<sub>2</sub> (dashed line) taken from reference [28].

In order to determine quantitatively the residual Ti amount on MG sample, we performed XAS spectra on different Ti layers prepared ad hoc. Three 500x500  $\mu\text{m}^2$  fields patterned with circular dots are fabricated on bulk silicon with electron beam lithography (EBL) and lift-off. The diameter of the dots is fixed to 500 nm and periodicity in the range of 2  $\mu\text{m}$  and 10  $\mu\text{m}$ ; 2 nm-thick layer of Ti is evaporated via electron beam in the same condition used for MG sample. A scheme of the sample is shown in Fig. 2.11. The average coverage of Ti

on each pattern field depends just on geometrical factor, such as the periodicity of the dots array and the thickness of the dots.

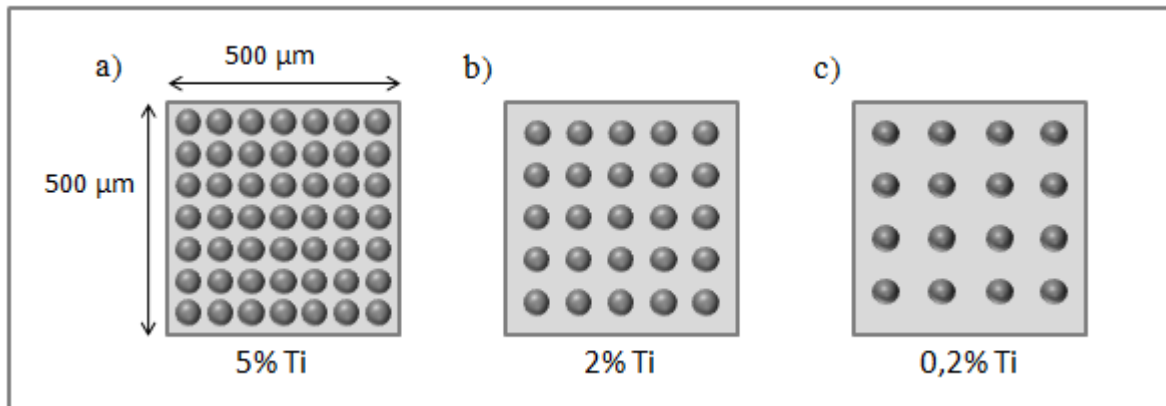


Fig. 2.11: scheme of the sample used as reference. Dots have a fixed diameter of 500 nm and different periodicity: a) 2  $\mu\text{m}$ , relative coverage of 5% of Ti; b) 3  $\mu\text{m}$ , relative coverage of 2% of Ti; c) 10  $\mu\text{m}$ , relative coverage of 0.2% of Ti.

For every field, XAS spectra are recorded in UHV conditions (base pressure  $\leq 10^{-9}$  mbar). XAS  $L_{23}$  edge of Ti is performed in total electron yield (TEY) method. The area of the illuminated sample is about 300  $\mu\text{m}$  x 50  $\mu\text{m}$  so that the spectra are not sensitive to the inhomogeneous distribution of the Ti on the sample surface. The spectra obtained for every field are shown in Fig. 2.12. The XAS spectrum obtained on the MG sample is inserted for comparison. The spectra are normalized to the background.

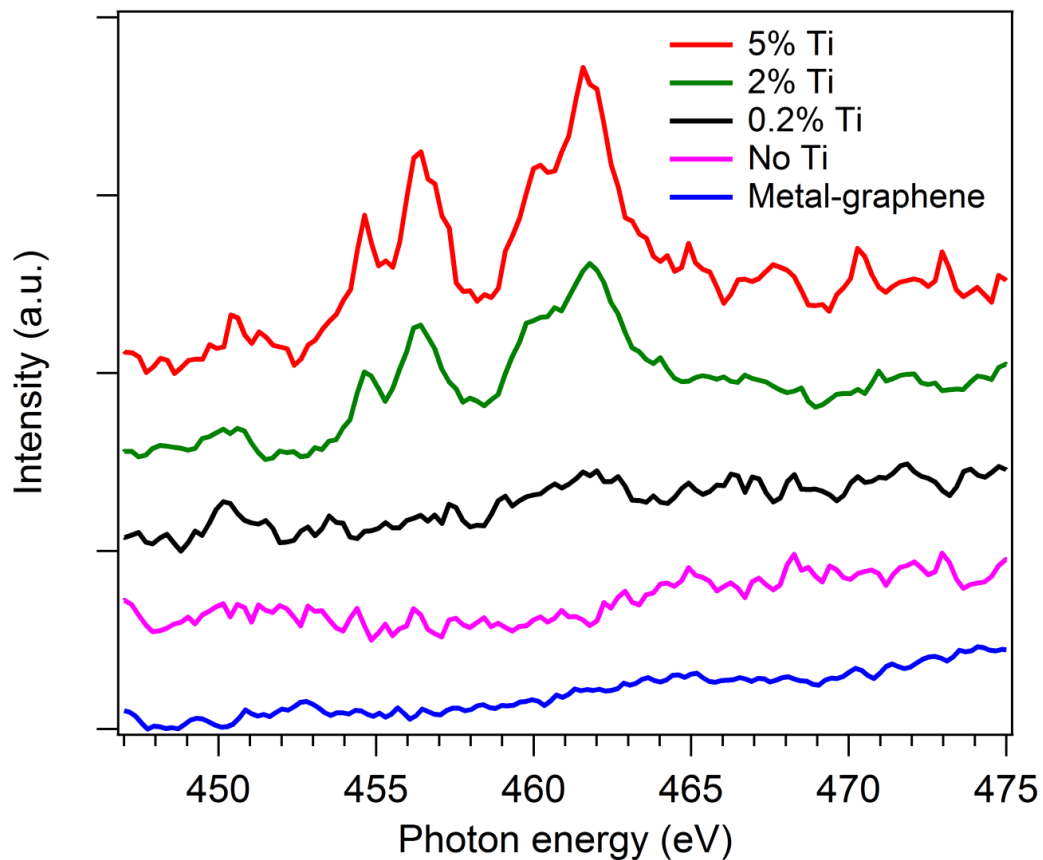


Fig. 2.12: XAS spectrum of metal-graphene (blue curve) compared with spectra obtained on reference sample and with spectrum obtained in an area without Ti (pink curve).

From the measure of the peak areas we achieved the calibration curve shown in Fig. 2.13, where the areas of the spectra are plotted against the average atomic density.

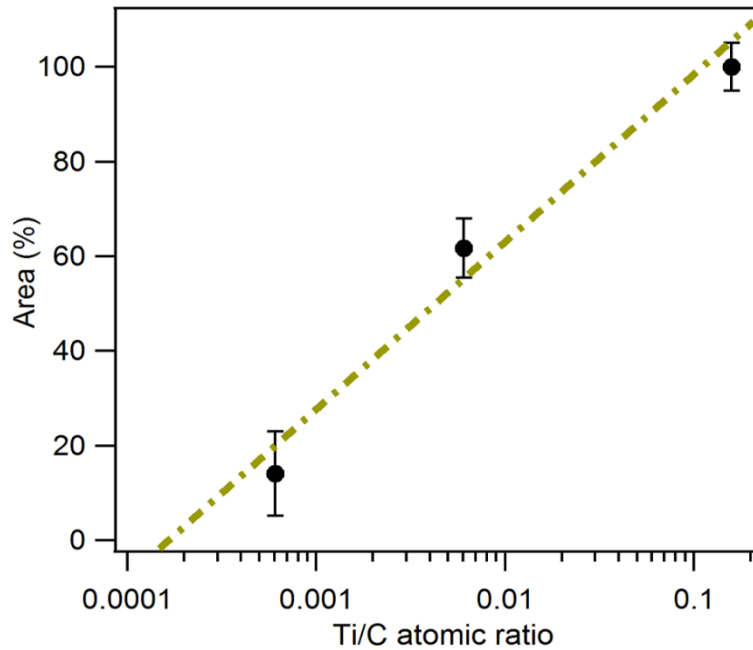


Fig. 2.13: calibration curve of Ti density on the reference sample. The ratio between Ti and C atoms is plotted in function of the areas (%) of XAS peaks.

We obtained 0.1 nm, 0.04 nm and 0.004 nm average coverage corresponding to  $6 \times 10^{14}$ ,  $2.3 \times 10^{13}$  and  $2.3 \times 10^{12}$  atoms/cm<sup>2</sup>, respectively for 2 μm, 3 μm and 10 μm periodicity. Comparing the three lowest spectra we can conclude that the quantity of Ti present after etching on metal-graphene sample is lower than  $2.3 \times 10^{12}$  atoms/cm<sup>2</sup>, that corresponds to the 1% of Ti.

#### 2.2.4 Electrical characterization

Electrical characterization has been performed on graphene transferred on a bulk silicon substrate with a thin thermal SiO<sub>2</sub> layer (300 nm). The transfer method is the same used for PG sample. 1 μm-thick gold contacts are fabricated via electron beam evaporation on the top of graphene using a shadow mask. A SEM image of the fabricated device is shown in Fig. 2.14:

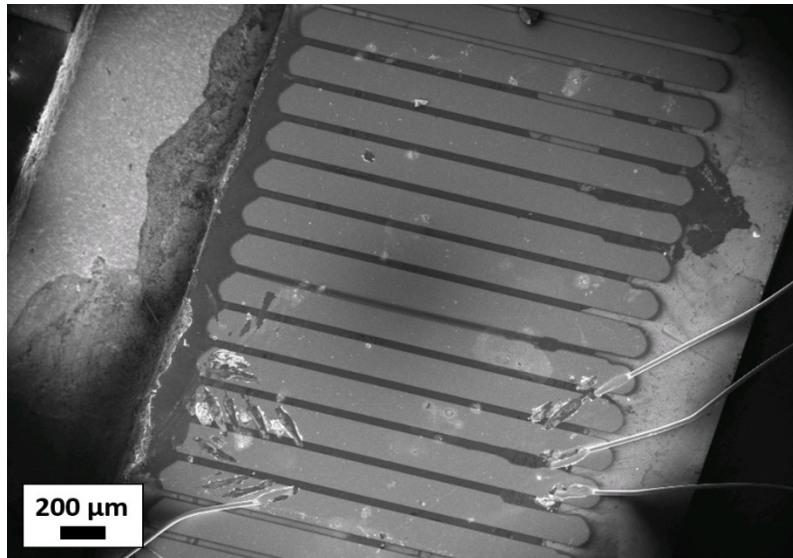


Fig. 2.14: SEM image of graphene transferred on gold contact on SiO<sub>2</sub>. Contacts are wire bonded for electrical measurements.

The sheet resistance is measured with the transmission line method [29] in air on a surface area of  $1900 \times 40 \text{ mm}^2$  using standard dc techniques with bias in the range  $-1.5 \div 1.5 \text{ V}$ . The measured sheet resistance results equal to  $2375 \text{ } \Omega/\text{sq}$ , higher than the value of  $350 \text{ } \Omega/\text{sq}$  reported in the product datasheet [17]. This difference can be ascribed to the size of the analyzed area. Indeed, the average size of the crystalline domains is of the order  $10 \text{ nm}$  so that many high resistance grain boundaries are included and the resulting resistivity is higher. However, the sheet resistance of high-quality, undoped graphene is usually of the order of  $6 \text{ k}\Omega/\text{sq}$  [30] (one conductivity quantum per species of charge carriers [31]), therefore the datasheet value provided by the company is somehow unreliable and other effects may play a dominant role. First, in the provided datasheet there are no information on how electrical measurements are performed. Second, information about the growth parameters is lacking. Therefore, we cannot exclude that the datasheet value is the result of a wrong measurement method or that a large intrinsic [32] or extrinsic doping is present. As a consequence, our measured higher value of sheet resistance after transfer could indicate the introduction of defects which decrease the electron mobility, or a compensation of the intrinsic doping effect. On the other hand if an extrinsic doping, for example due to atmospheric contaminants [33] is present, our transfer method could have removed those contaminants and thus reduced the doping effect. Since we had no means alternative to graphene transfer to measure the conductivity of the pristine material, we have not been able to further analyze this issue.

The same electrical measurements were not possible for the MG protocol because the use of HF metal etching solution removes the oxide; however, we expect the graphene resistivity to be dominated by grain boundary defects also in this case.

## References

- [1] Ferrari AC, Meyer JC, Scardaci V, Casiraghi C, Lazzeri M, Mauri F, Piscanec S, Jiang D, Novoselov KS, Roth S, Geim AK. *Raman Spectrum of Graphene and Graphene Layers*. Physical Review Letters 2006, 97, 187401.
- [2] Kang, J., Shin, D., Bae, S., Hong, B.H. *Graphene transfer: Key for applications* (2012) Nanoscale, 4 (18), pp. 5527-5537.
- [3] Fangping, O., Huang, B., Li, Z., Xiao, J., Wang, H., Xu, H. *Chemical functionalization of graphene nanoribbons by carboxyl groups on stone-wales defects* (2008) Journal of Physical Chemistry C, 112 (31), pp. 12003-12007.
- [4] Ahn, Y., Kim, H., Kim, Y.-H., Yi, Y., Kim, S.-I. *Procedure of removing polymer residues and its influences on electronic and structural characteristics of graphene* (2013) Applied Physics Letters, 102 (9), art. no. 091602.
- [5] Chen, J.-H., Jang, C., Xiao, S., Ishigami, M., Fuhrer, M.S. *Intrinsic and extrinsic performance limits of graphene devices on SiO<sub>2</sub>* (2008) Nature Nanotechnology, 3 (4), pp. 206-209.
- [6] Ryu, S., Liu, L., Berciaud, S., Yu, Y.-J., Liu, H., Kim, P., Flynn, G.W., Brus, L.E. *Atmospheric oxygen binding and hole doping in deformed graphene on a SiO<sub>2</sub> substrate* (2010) Nano Letters, 10 (12), pp. 4944-4951.
- [7] Kim, H.H., Yang, J.W., Jo, S.B., Kang, B., Lee, S.K., Bong, H., Lee, G., Kim, K.S., Cho, K. *Substrate-induced solvent intercalation for stable graphene doping* (2013) ACS Nano, 7 (2), pp. 1155-1162.
- [8] Goossens, A.M., Calado, V.E., Barreiro, A., Watanabe, K., Taniguchi, T., Vandersypen, L.M.K. *Mechanical cleaning of graphene* (2012) Applied Physics Letters, 100 (7), art. no. 073110.
- [9] Lim, Y.-D., Lee, D.-Y., Shen, T.-Z., Ra, C.-H., Choi, J.-Y., Yoo, W.J. *Si-compatible cleaning process for graphene using low-density inductively coupled plasma* (2012) ACS Nano, 6 (5), pp. 4410-4417.
- [10] Li X, Zhu Y, Cai W, Borysiak M, Han B, Chen D, Piner RD, Colomba L, Ruoff RS. *Transfer of large-area graphene films for high-performance transparent conductive electrodes*. Nano Letters 2009, 9 (12), pp. 4359-4363.

- [11] Barin GB, Song Y, Gimenez IDF, Filho AGS, Barreto LS, Kong J. *Optimized graphene transfer: Influence of polymethylmethacrylate (PMMA) layer concentration and baking time on graphene final performance*. Carbon 2015, 84 (C), pp. 82-90.
- [12] [www.graphenea.com](http://www.graphenea.com)
- [13] Unarunotai, S., Koepke, J.C., Tsai, C.-L., Du, F., Chialvo, C.E., Murata, Y., Haasch, R., Petrov, I., Mason, N., Shim, M., Lyding, J., Rogers, J.A. *Layer-by-layer transfer of multiple, large area sheets of graphene grown in multilayer stacks on a single SiC wafer* (2010) ACS Nano, 4 (10), pp. 5591-5598.
- [14] Unarunotai, S., Murata, Y., Chialvo, C.E., Kim, H.-S., MacLaren, S., Mason, N., Petrov, I., Rogers, J.A. *Transfer of graphene layers grown on SiC wafers to other substrates and their integration into field effect transistors* (2009) Applied Physics Letters, 95 (20), art. no. 202101.
- [15] Jang, M., Trung, T.Q., Jung, J.-H., Kim, B.-Y., Lee, N.-E. *Improved performance and stability of field-effect transistors with polymeric residue-free graphene channel transferred by gold layer* (2014) Physical Chemistry Chemical Physics, 16 (9), pp. 4098-4105.
- [16] Joiner CA, Roy T, Hesabi ZR, Chakrabarti B, Vogel EM. *Cleaning graphene with a titanium sacrificial layer*. Applied Physics Letters 2014, 104 (22), art. no. 223109.
- [17] Available at:  
[https://cdn.shopify.com/s/files/1/0191/2296/files/Graphenea\\_Monolayer\\_Film\\_Datash eet\\_2\\_015-05-14.pdf?2328580123161991674](https://cdn.shopify.com/s/files/1/0191/2296/files/Graphenea_Monolayer_Film_Datash eet_2_015-05-14.pdf?2328580123161991674).
- [18] Liu TH, Pao CW, Chang CC. *Effects of dislocation densities and distributions on graphene grain boundary failure strengths from atomistic simulations*. Carbon 2012, 50 (10), pp. 3465-3472.
- [19] Huang PY, Ruiz-Vargas CS, Van Der Zande AM, Whitney WS, Levendorf MP, Kevek JW, Garg S, Alden JS, Hustedt CJ, Zhu Y, Park J, McEuen PL, Muller DA *Grains and grain boundaries in single-layer graphene atomic patchwork quilts*. Nature 2011, 469 (7330), pp. 389-392.
- [20] Frank O, Vejpravova J, Holy V, Kavan L, Kalbac M. *Interaction between graphene and copper substrate: The role of lattice orientation*. Carbon 2014, 68, pp. 440-451.
- [21] Zhao Y, Chen G, Du Y, Xu J, Wu S, Qu Y, Zhu Y. *Plasmonic-enhanced Raman scattering of graphene on growth substrates and its application in SERS*. Nanoscale 2014, 6 (22), pp. 13754-13760.



- [22] Ferrari, A. *Raman spectroscopy of graphene and graphite: Disorder, electron–phonon coupling, doping and nonadiabatic effects*. Solid State Communications 143 (2007) 47–57.
- [23] Ng ML, Balog R, Hornekær L, Preobrajenski AB, Vinogradov NA, Mårtensson N, Schulte K. *Controlling hydrogenation of graphene on transition metals*. Journal of Physical Chemistry C 2010, 114 (43), pp. 18559-18565.
- [24] Webb MJ, Palmgren P, Pal P, Karis O, Grennberg H. *A simple method to produce almost perfect graphene on highly oriented pyrolytic graphite*. Carbon 2001, 49. 3242-3249.
- [25] Peltekis N, Kumar S, McEvoy N, Lee K, Weidlich A, Duesberg GS. *The effect of downstream plasma treatments on graphene surfaces*. Carbon 2012, 50 (2), pp. 395-403.
- [26] Kidambi PR, Bayer BC, Blume R, Wang ZJ, Baetz C, Weatherup RS, Willinger MG, Schloegl R, Hofmann S. *Observing graphene grow: Catalyst-graphene interactions during scalable graphene growth on polycrystalline copper*. Nano Letters 2013, 13 (10), pp. 4769-4778.
- [27] Favaro M, Agnoli S, Di Valentin C, Mattevi C, Cattelan M, Artiglia L, Magnano E, Bondino F, Nappini S, Granozzi G. *TiO<sub>2</sub>/graphene nanocomposites from the direct reduction of graphene oxide by metal evaporation*. Carbon 2014, 68, pp. 319-329.
- [28] Pasquali L, Selvaggi G, Montecchi M, Banshchikov AG, Kaveev AK, Suturin SM, Sokolov NS, Borgatti F, Doyle B, Giglia A, Mahne N, Pedio M, Nannarone S. *X-Ray absorption and reflectivity studies of MnF<sub>2</sub> initial growth on CaF<sub>2</sub>/Si(111)*. In 12th International Symposium NANOSTRUCTURES: Physics and Technology, St Petersburg, Russia, June 21-25, 2004 (literal).
- [29] M. Lazzarino, T. Ozzello, G. Bratina, J.J. Paggel, L. Vanzetti, L. Sorba, A. Franciosi, *Low resistance graded contacts to n-type ZnSe*. Applied Physics Letters 68 (3) (1996) 370-372.
- [30] Blake, P., Brimicombe, P.D., Nair, R.R., Booth, T.J., Jiang, D., Schedin, F., Ponomarenko, L.A., Morozov, S.V., Gleeson, H.F., Hill, E.W., Geim, A.K., Novoselov, K.S. *Graphene-based liquid crystal device* (2008) Nano Letters, 8 (6), pp. 1704-1708.
- [31] Geim, A.K., Novoselov, K.S. *The rise of graphene* (2007) Nature Materials, 6 (3), pp. 183-191.
- [32] Guermoune, A., Chari, T., Popescu, F., Sabri, S.S., Guillemette, J., Skulason, H.S., Szkopek, T., Siaj, M. *Chemical vapor deposition synthesis of graphene on copper with methanol, ethanol, and propanol precursors* (2011) Carbon, 49 (13), pp. 4204-4210.

[33] Cao, P., Varghese, J.O., Xu, K., Heath, J.R. *Visualizing local doping effects of individual water clusters on gold(111)-supported graphene* (2012) *Nano Letters*, 12 (3), pp. 1459-1463.



# Chapter 3

## 3.1 Transparent graphene membranes for ultra-high vacuum experiments in liquid

When a chemical reaction in the gas or the liquid phase requires the presence of a solid catalyst, the investigation of solid-liquid interfaces can provide important information to the understanding and the improvement of the process yield. Usually, the transfer of electrons from the solid substrate to the solution and *vice-versa* is a fundamental effect that should be considered, and therefore its measure is particularly relevant. Photoelectron spectroscopy is a powerful tool to quantify the change of the electronic charge of a molecule or a material. It is usually performed in ultra-high vacuum (UHV) conditions while its application in ambient conditions or, even worst, in liquid, are hindered by the extremely low inelastic mean free path (IMFP) of electrons in a dense media. In this condition, to separate the sample environment from the UHV conditions is a mandatory requirement. Today, different approaches have been developed to overcome this limit and to perform *in situ* and *in operando* study of this processes.

The first approach is based on the use of ambient pressure x-ray photoelectron spectroscopy, when a thin layer of liquid is condensed on the top of the sample; the ambient in contact with the sample is close to the atmospheric pressure, while the rest of the system is kept in vacuum conditions [1].

A second approach is based on the use of liquid cells fabricated with a material which serves as transparent window to photons and electrons. The most used materials are SiO<sub>2</sub> [2], Si<sub>3</sub>N<sub>4</sub> [3] or beryllium [4]. In 2013, Masuda *et al.*, used a SiO<sub>2</sub> membrane as separator between liquid and vacuum to perform *in situ* XPS for the monitoring of silicon oxide growth during electrochemical oxidation at the silicon/water interface [5]. Unfortunately, the minimum thickness of those windows (~50 nm) exceeds the photoelectron IMFP, therefore they can be used only for some technique, such as XAS measurements in fluorescence yield. To provide a tool usable also for other techniques as XPS and XAS, a new approach is needed.

A straightforward solution could be based on the use of a thin membrane which allows higher transmission of photons and electrons. 2D materials such as graphene [6], GO [2], or hexagonal boron nitride [7], seem to be perfect for the realization of photoelectron transparent membranes because of their few atomic layer and mechanical robustness. In particular, graphene represents the ultimate solution because of its elasticity, mechanical strength, impermeability, electron conductivity and transparency to both x-ray radiation and photo-emitted electrons. Alivisatos and coworkers [6] demonstrated the possibility to trap an aqueous solution of DNA-Au-nanoparticles in a sealed liquid cell created by coupling two graphene layers; they were able to observe the dynamic of the system with transmission electron microscope with nanometer resolution. In 2011, Kolmakov and coworkers proved that GO is transparent enough to perform soft x-ray photoelectron measurements [2]; they developed a liquid cell with SiO<sub>2</sub> or Si<sub>3</sub>N<sub>4</sub> membrane with micrometric sized holes covered with few flakes of GO for the observation of water in UHV condition. The problem is that GO it is not conductive and photoelectron spectroscopy require an energy reference [8]; secondly, the thickness of GO membrane cannot be precisely controlled. Finally, because of the small size of the holes a focalized x-ray photon beam was used, but the large photon density created gas bubbles that made the measurements of the liquid disturbed by water radiolysis. The straightforward solution would have been to use larger holes and a defocused beam, but, unfortunately, large flakes of GO were not available.

Trying to overcome this problems, the same group fabricated a transparent graphene membrane [9], demonstrating the advantages of the graphene use in the observation of water with soft x-rays as alternative under-pressure approach. Another study reported by Salmeron and co-workers presents a graphene membrane liquid cell formed by graphene bilayer on a gold-coated Si<sub>3</sub>N<sub>4</sub> membrane with an array of holes [10]. The fundamental problem observed in both the experiments is due to the formation of bubble under continuous illumination of the beam, due to water radiolysis: first, the bubbles can disturb the *in operando* measurements and secondly, the radical produced by the radiolysis may locally oxidize the graphene generating local defects that will collapse under the high pressure developed by the formation of gas bubbles.

## 3.2 Graphene nanobubbles for transparent liquid cells

It is evident that graphene membranes represent a very powerful tool to study *in situ* and *in operando* processes at solid-liquid interfaces, but it should be noted that it is very difficult to obtain large and suspended membranes that do not collapse when placed in vacuum. Secondly, a perfect sealing and a good contact between graphene and the liquid inside the cell is fundamental for the success of the measurements. Keeping in mind these considerations, one can take advantage from graphene flexibility and capacity to deform. When graphene is attached on a substrate, the latter or the transfer itself can induce ripples and blisters. If it could be possible to trap a solution between these ripples and the substrate, these graphene nanobubbles (GNBs) can be used as a sealed, transparent cell. For instance, it was observed that the biaxial strain caused by a thermal process on graphene/hexagonal boron nitride heterostructure can lead to the formation of GNBs [11]. Another example is given by GNBs on diamond used as hydrothermal anvil cell to observe superheating water with different techniques, such as AFM, Raman and *in situ* Fourier transform infrared spectroscopy [12].

In our laboratory, I obtained GNBs on different substrates, such as  $\text{SiO}_2$ ,  $\text{TiO}_2$  and also between two graphene layers suspended on a  $\text{Si}_3\text{N}_4$  membrane. Fig. 3.1a shows a SEM image of GNBs on a  $\text{TiO}_2$  single crystal substrate and the Fig. 3.1b presents an image of GNBs trapped in a graphene bilayer suspended on a  $\text{Si}_3\text{N}_4$  membrane 200-nm-thick, patterned with holes with diameters and periodicity of 8  $\mu\text{m}$  and 16  $\mu\text{m}$ , respectively.

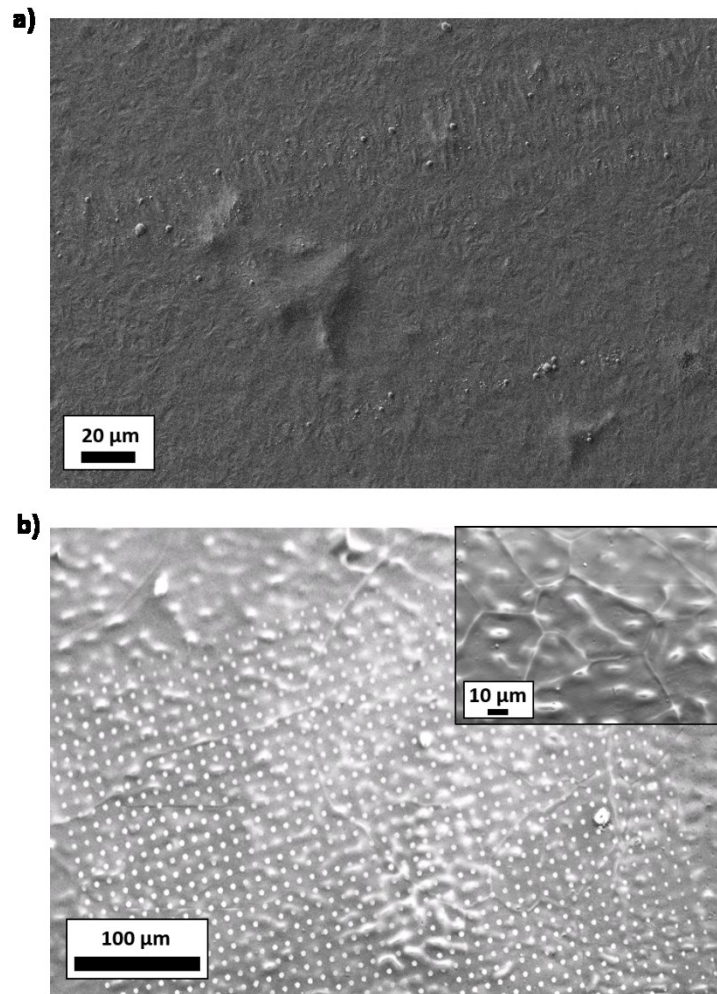


Fig. 3.1: SEM images of GNBs trapped between: a) graphene monolayer and  $\text{TiO}_2$  (100) rutile single crystal; b) two graphene layers suspended on a  $\text{Si}_3\text{N}_4$  membrane. The bilayer is obtained with a double wet transfer using the protocol described in chapter 2 for the PG sample. The inset shows GNBs on a not patterned part of the membrane [Matruglio *et al.*, unpublished].

Fig. 3.1a shows a very large bubble, with size of tens of  $\mu\text{m}$ , but generally the obtained bubbles have size from a few nm to a few microns, such as those obtained in Fig. 3.1b.

### **3.3 Graphene nanobubbles on TiO<sub>2</sub> for *in situ* electron spectroscopy of water**

To realize a sealed cell containing liquid for UHV electron spectroscopy, we decided to create GNBs trapping water on a TiO<sub>2</sub> (100) rutile single crystal substrate. TiO<sub>2</sub> was chosen because it is an important wide-band gap semiconductor and it has been extensively investigated as photocatalyst in a large variety of applications, including air and water purification system [13], hydrogen evolution [14], photo-degradation of pollutants [15], water splitting [16], reduction of carbon dioxide (CO<sub>2</sub>) into carbon fuels [17] and self-cleaning surfaces [18].

The presence of liquid trapped underneath the graphene layer enables the use of this system as liquid cell for XPS and XAS studies in liquid phase or at the solid-liquid interface. In the next sections the production and the characterization of the GNBs will be described. The cells will be used for *in situ* study of water under thermal treatment with AFM, Raman, XPS and XAS techniques in UHV conditions.

#### **3.3.1 Fabrication of graphene nanobubbles**

The GNBs are obtained starting from commercially available CVD graphene on Cu [19]. Fig. 3.2 shows the Raman spectrum of the graphene on Cu as received, obtained with excitation wavelength of 532 nm and the laser power on the sample of 1 mW.



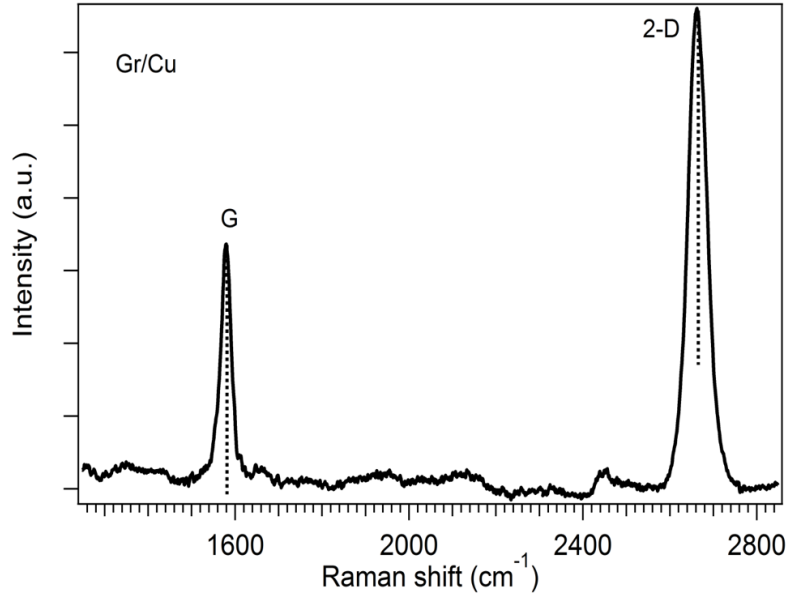
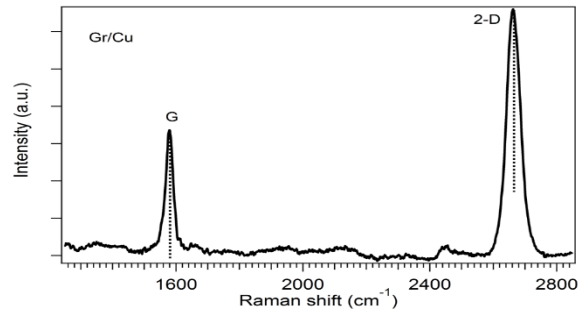


Fig. 3.2: Raman spectrum of the graphene as-received. No distinguishable D peak is observed providing an indication of a not defected, good quality graphene.

#### Graphene Raman spectrum

In graphene, the Stokes phonon energy shift caused by laser excitation (532 nm) creates two peaks: G (1580 cm<sup>-1</sup>), a primary in-plane vibrational mode, that involves sp<sup>2</sup> hybridized carbon atoms (linear increase as the number of graphene layers increases), and D band (1350 cm<sup>-1</sup>), a ring breathing mode from sp<sup>2</sup> carbon rings, which must be near an edge or a defect to be active. Therefore, in absence of defects the D band is not visible. The second-order overtone of a different inplane vibration is the 2D band (2690 cm<sup>-1</sup>). The number of layers can be derived from the ratio of peak intensities,  $I_{2D}/I_G$ , as well as the position and shape of these peaks; in high quality (defect free) single layer graphene is  $\sim 2$ .



The graphene monolayer is transferred on a TiO<sub>2</sub> (100) rutile single crystal using the thermoplastic polymer mr-I 7020 as sacrificial layer instead of the commonly used PMMA, for the reasons presented in the Chapter 2 [20]. The mr-I 7020 seems the right choice because a high quantity of impurities on top of the graphene may hinder the escape of the electrons photoemitted from the underlying sample. The transfer method based on a Ti sacrificial layer

cannot be applied because the HF etching solution of the Ti sacrificial layer can also etch the TiO<sub>2</sub> substrate.

Following the protocol developed in Chapter 2 for the PG sample, 250 nm of mr-I 7020 was spin-coated on graphene on Cu. The Cu foil is etched overnight in a Cu etching solution (FeCl<sub>3</sub>:H<sub>2</sub>O=3:7 ratio in volume). Possible residuals due to the etching solutions (Fe and Cu) are avoided rinsing the graphene/polymer membrane in DI water. The GNBs are obtained fishing graphene into DI water directly on the TiO<sub>2</sub> crystal with the TiO<sub>2</sub> approaching the substrate in a parallel direction with the graphene-polymer membrane, avoiding the water escape. The wettability of the bare TiO<sub>2</sub> substrate, and thus the number of GNBs, was previously modulated by oxygen plasma and thermal treatments up to 700°C [21] because surface defects and adsorption of OH<sup>-</sup> groups on the crystal surface contribute to the formation of GNBs during the transfer procedure. Finally, mr-I 7020 is dissolved in cold acetone for 5 minutes. A scheme of the transfer procedure is reported in Fig. 3.3:

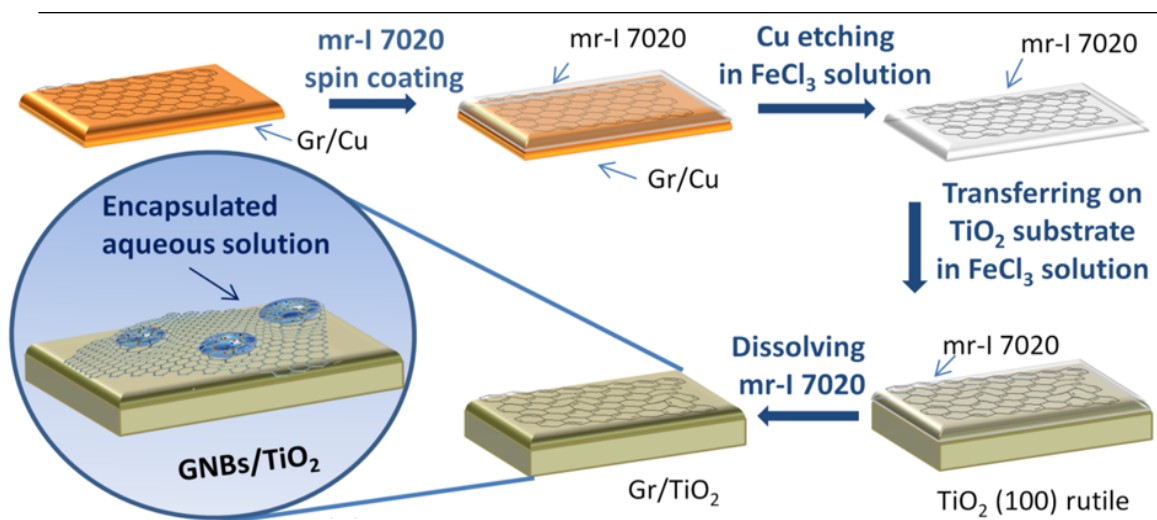


Fig. 3.3: scheme of the graphene wet transfer process from Cu to TiO<sub>2</sub> substrate.

To verify the absence of residuals due to the etching solution, XAS measurements have been performed on the CNR BACH beamline at Elettra Sincrotrone Trieste. The XAS spectra of Fe L23-edge and Cu L23-edge are shown in Fig. 3.4a and b, respectively.

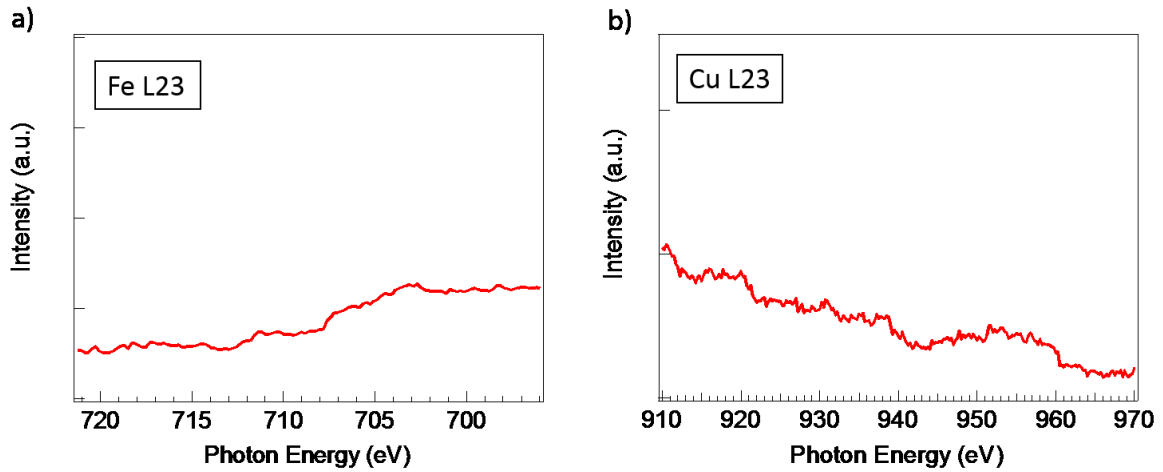


Fig. 3.4: XAS spectra of: (a) Fe L23-edge and (b) Cu L23-edge.

It was observed that even with low concentrations of Fe, such as 0.025 ML deposited on Cu(100), the typical peaks and structures of Fe L23 are visible in XAS spectra [22]. Moreover, it is known that 1 ML of Fe (bcc) corresponds to  $1.214 \times 10^{15}$  atoms/cm<sup>2</sup> [23]. Since no structures are detectable in our spectrum (Fig. 3.4a), we can estimate that Fe residuals are for sure lower than  $10^{15}$  atoms/cm<sup>2</sup> and lower than 0.025 ML.

Regarding the Cu, Ferretti *et al.* deposited Cu clusters on a Si substrate, and observed that for a coverage of  $(3 - 8) \times 10^{12}$  atoms/cm<sup>2</sup>, Cu structure is visible in the Cu L3 XANES spectrum [24]. In Fig. 3.4b, no structures are clearly visible, indicating that Cu residuals are lower than the value of  $10^{12}$  atoms/cm<sup>2</sup>.

### 3.3.2 Characterization of graphene nanobubbles

To prove the presence of the water trapped in the GNBs, AFM measurements have been performed on the freshly prepared sample and compared with the same sample annealed for 1 hour at 350 °C in UHV. The measurements have been performed in intermittent mode using Nanowizard II AFM (JPK), which allows to scan the sample in the range of 100x100x15 μm. PPP-FM silicon probes (Nanosensors) with a force constant of 3 N/m and guaranteed tip radius of curvature less than 10 nm has been used. The scan rate was 0.25 Hz. The obtained measurements are shown in Fig. 3.5.

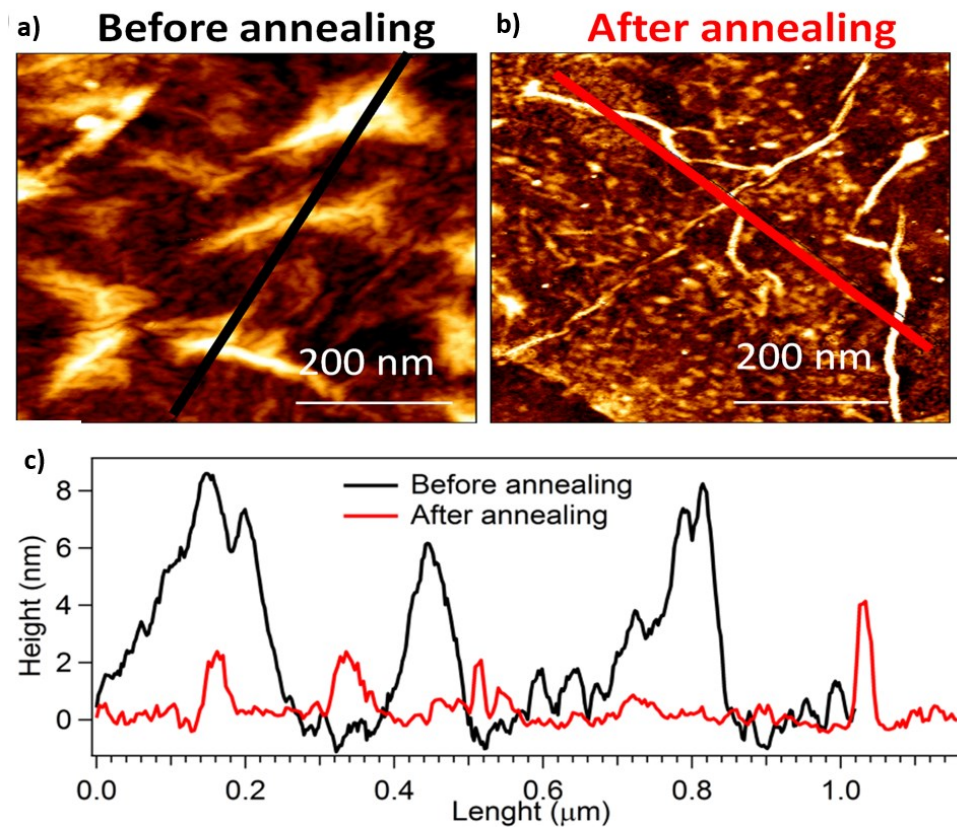


Fig. 3.5: (a) AFM image of GNBs full of water on TiO<sub>2</sub> substrate before annealing; (b) AFM image of the same sample after annealing at 350°C, which induce a clear GNB collapse; (c) height profile obtained before annealing (black curve) and after the annealing (red curve). Irregularly shaped GNBs with an average height of 6 nm and lateral size of a few hundreds of nanometers are observed before the annealing, while a nearly flat layer is formed after the annealing.

The height profile before the annealing process (black curve in Fig. 3.5c) indicates the formation of irregularly shaped GNBs with an average height of 6 nm, and lateral size of a few hundreds of nm. The AFM images in Fig. 3.5a and b show a change in the topography after the annealing, confirmed also from the height profile (red curve in Fig. 3.5c): graphene becomes flat and the number of defects and sharp bends increases. Our interpretation is that the extra breaks are formed in the sites where the biggest GNBs collapsed due to the overpressure generated by the thermal treatment in UHV.

To confirm our hypothesis and to characterize the structural changes of the system, we performed Raman spectroscopy in order to have an indication about graphene quality and defects before and after the thermal treatment. Raman measurements have been performed

in the reflection geometry on an inverted optical microscope (Axiovert 200, Zeiss) coupled with a 750 mm long spectrometer (Shamrock SR-750, Andor Technology plc). CW laser with the excitation wavelength of 532 nm (Cobolt Samba, 50 mW, bandwidth 1 MHz) was used as an excitation source, with a diameter of laser spot of  $\sim 0.35 \mu\text{m}$  and power of 1 mW. The Raman spectra obtained before (black spectrum) and after the annealing (red spectrum) are shown in Fig. 3.6.

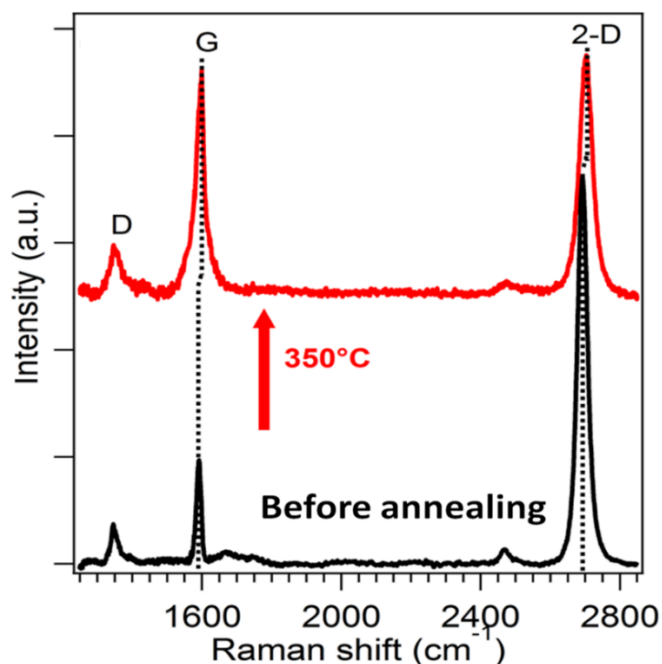


Fig. 3.6: Raman spectra of GNBs before (black curve) and after the annealing (red curve).

The increasing of D peak and the diminution of the 2D/G ratio indicate an increase of defects and a deterioration of the quality.

The spectra show the three distinct peaks of graphene [25]: D peak at  $1350 \text{ cm}^{-1}$ , G and 2D peaks at  $1590 \text{ cm}^{-1}$  and  $2695 \text{ cm}^{-1}$ , respectively. The as-transferred graphene is characterized by a high 2D/G ratio, about 3.7, indication of the high quality of the layer [26]. The presence of the D peak indicates that some defects are introduced during the transfer process: indeed, before the transfer the as-grown graphene does not show any D peak (Fig. 3.2b). After annealing the 2D/G ratio is  $\sim 1$ , indicating a deterioration of the quality, which is consistent with the sharp bends and cracks already observed in the AFM images. The positions of D, G and 2D peaks after annealing are systematically up-shifted and broadened that is a sign of

a trend from a tensile-like to a compressive-like strain [26]. A similar behavior was already observed in other system, such as graphene nanoblisters filled with gas [27].

A scheme of the whole process is shown in Fig. 3.7:

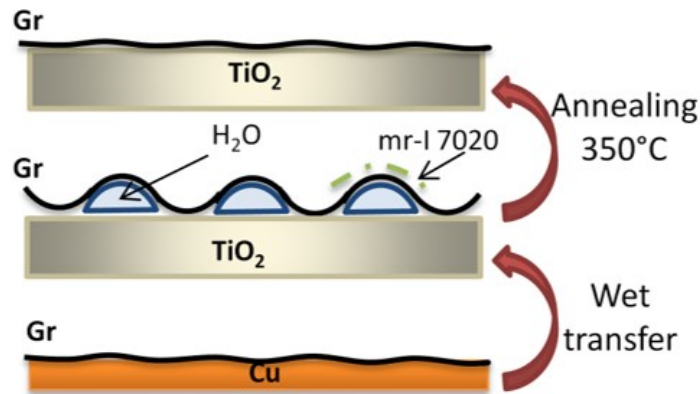


Fig. 3.7: summary scheme of the whole process, from the graphene on metal to the final configuration measured.

In order to have information about the orbital hybridization and orientation of the graphene layer transferred on the TiO<sub>2</sub> crystal, polarization-dependent NEXAFS has been carried out in UHV (base pressure  $< 10^{-9}$  mbar). NEXAFS at the C K-edge were measured in partial electron yield mode at two different angles between polarization vector and surface plane: normal incidence geometry ( $\Theta = 0^\circ$ , s-polarization) and near grazing incidence geometry ( $\Theta = 60^\circ$ , p-polarization). The spectra are shown in Fig. 3.8.

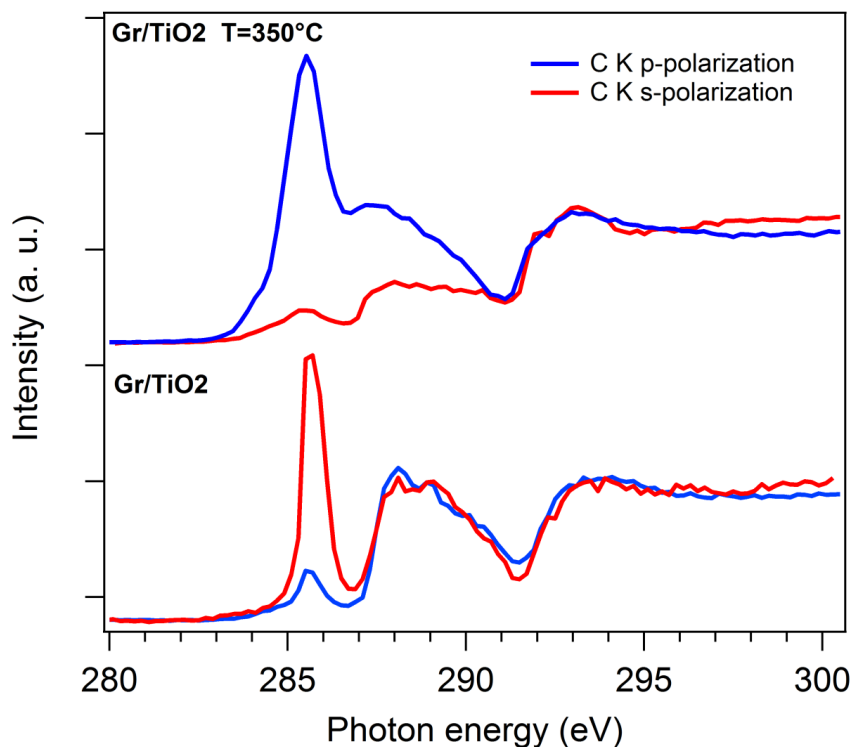


Fig. 3.8: Polarization dependent NEXAFS at C-K edge of as-transferred graphene/TiO<sub>2</sub> (lower spectra) and graphene/TiO<sub>2</sub> annealed at 350°C in UHV (upper spectra).

The spectra suggest the transition from a curved morphology (GNBs) to a flat graphene layer after water evaporation. The spectrum of as-transferred graphene shows a limited dichroism of the  $\pi$ - and  $\sigma$ -resonances in comparison to the annealed one. This behavior can be observed in systems with curved morphology, where the  $\pi^*$  orbitals are randomly oriented with respect to the photon electric field along the surface [28].

### 3.3.3 Ultra-high vacuum measurements on graphene nanobubbles

To demonstrate the possibility to perform x-ray electron measurements *in situ*, XPS have been performed. The spectra of the system before and after the annealing are compared with the spectrum of graphene as-received. XPS spectra of C1s, O1s and Ti 2p core levels are recorded using two different excitation energies: 596 and 1049 eV. A VG-Scienta R3000 hemispherical analyzer, working with an overall energy resolution of 0.2 eV, was used for XPS measurements. C1s peaks of the system before and after the annealing is shown in Fig.

3.9; the spectra are fitted by a Gaussian function prior subtraction of Shirley background to account for the inelastic photoelectrons.

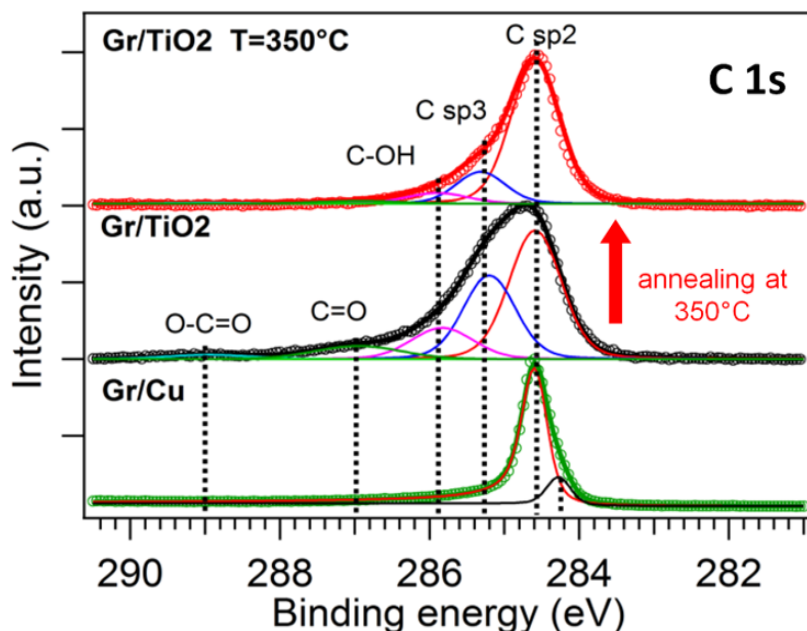


Fig. 3.9: C1s XPS spectra of graphene on Cu as grown (green curve), GNBs on TiO<sub>2</sub> as transferred (black curve), and graphene on TiO<sub>2</sub> after the annealing at 350°C (red curve).

The main peak at 284.5 eV corresponds to the sp<sup>2</sup> carbon (C=C), distinctive of pristine graphene, while the second component at 285.0 eV is ascribed to sp<sup>3</sup> species that are due to amorphous carbon introduced during the transfer process [29]. The weak component at 285.6 eV is a signal of C–O bonds, which could be associated to the formation of hydrogenated or oxidized species at the boundaries, such as C-OH or epoxy groups [30]. The small components at higher binding energies typical of C=O (~286 eV) or O=C-O (~288 eV) species indicates the presence of some polymer residuals from mr-I 7020 employed for the transfer. The contribution of these components is less than the main sp<sup>2</sup> carbon peak, showing that the as-transferred graphene is quite clean. After 1 h of annealing at 350 °C, a clear narrowing of the C1s spectrum of graphene/TiO<sub>2</sub> is observed as a consequence of the thermal removal of mr-I 7020 polymer residuals. In fact, all the components at higher binding energies associated to C=O or O=C-OH species are absent.

To prove the presence of the water, O 1s spectra have been recorded. The spectra are shown in Fig. 3.10.



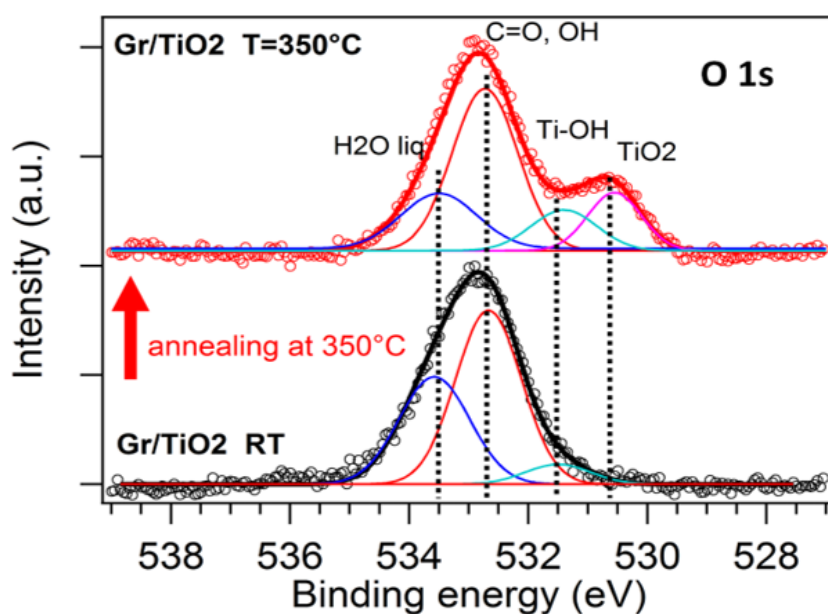


Fig. 3.10: O1s XPS spectra of GNBs on TiO<sub>2</sub> before (black curve) and after the annealing (red curve).

Spectra are deconvoluted using four Gaussian components: as-transferred Gr presents a peak at 531.4 eV that is associated to oxygen deficiencies on TiO<sub>2</sub> surface [31] and to bridging hydroxyls on the surface vacancies [32] of TiO<sub>2</sub>, while the component at 532.5 eV can be attributed to C-OH or C-O groups most likely due to polymer residuals or epoxy species at the boundaries of the Gr layer, as also observed on C 1s [33]. The component at 533.5 eV is in good agreement with the binding energy (BE) of liquid water [34, 35]. These data strongly indicate that a layer of liquid water and hydroxyl species were trapped at the graphene/TiO<sub>2</sub> interface during the wet transfer procedure. After the annealing at 350°C, the liquid component of water (533.5 eV) is clearly reduced, although not completely removed. Also the intensity of C-O and C-OH components on the surface of graphene decreases as consequence of the thermal removal of polymer residuals. Interestingly, an extra peak at 530.5 eV originating from the lattice oxygen of TiO<sub>2</sub> appears [36]. To confirm this last result, Ti 2p spectra are recorded and shown in Fig. 3.11.

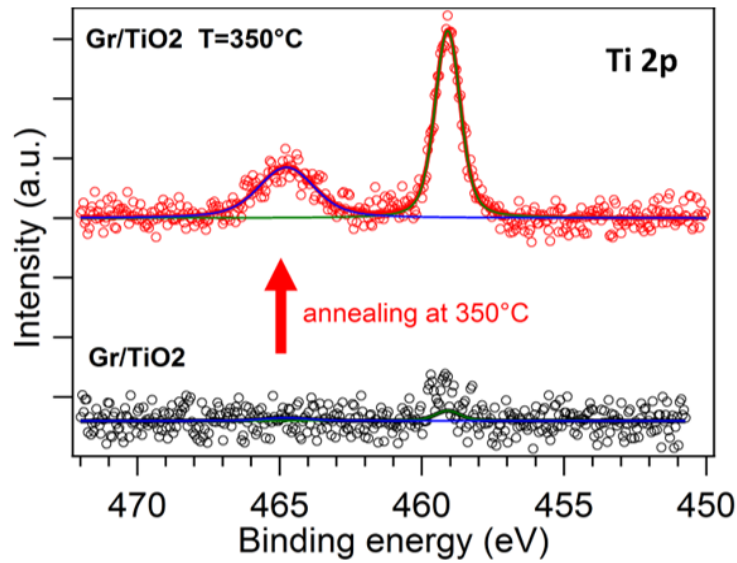


Fig. 3.11: Ti 2p XPS spectra of GNBs on TiO<sub>2</sub> before (black curve) and after the annealing (red curve).

Before the thermal treatment, the TiO<sub>2</sub> core-level emission peak is barely visible, while after annealing the two peaks with BE of 458.5 and 464.2 eV arising from spin orbit-splitting 2p<sub>3/2</sub> and 2p<sub>1/2</sub> of Ti<sup>4+</sup> in TiO<sub>2</sub> are clearly observed [37]. No trace of Ti<sup>3+</sup> or Ti<sup>2+</sup> signals are present in Ti 2p spectra indicating that the thermal treatment does not affect the stoichiometry of rutile [37]. This is confirmed also by XAS spectra at the L<sub>23</sub> edge of Ti of Gr/TiO<sub>2</sub> (100) single crystal, recorded before and after the annealing; the measurements are performed in total electron (TEY) method. The results are shown in Fig. 3.12.

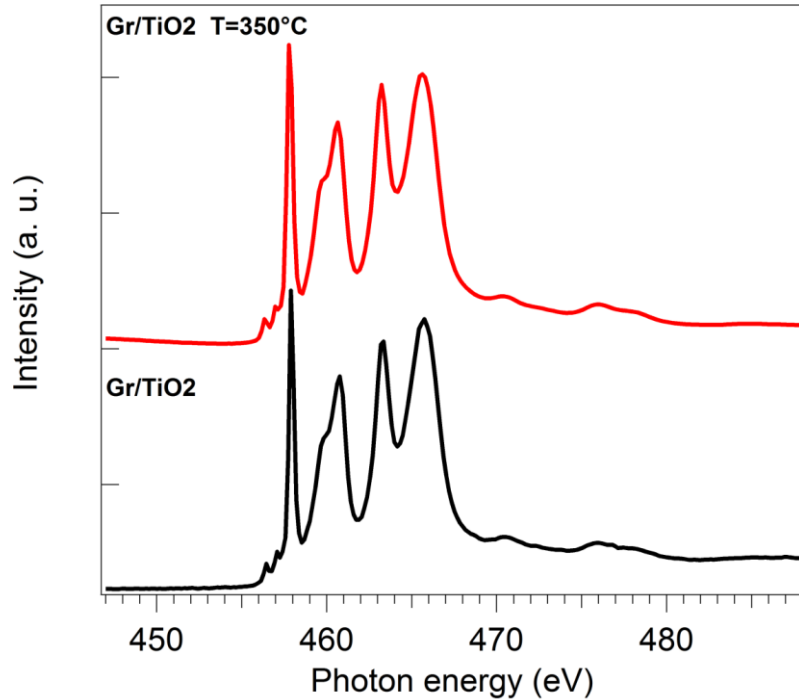


Fig. 3.12: XAS at Ti L<sub>2,3</sub> edge of rutile in as-transferred Gr/TiO<sub>2</sub> (black curve) and Gr/TiO<sub>2</sub> annealed at 350°C in UHV (red curve).

Both Ti L<sub>2,3</sub> XAS spectra show the typical structure of rutile single crystal [37] with two small pre-edge features at 456.4 eV and 457 eV, and the distinctive splitting of the L<sub>2</sub> and L<sub>3</sub> components. Ti L<sub>2,3</sub> XAS show that the stoichiometry of TiO<sub>2</sub> crystal is not affected by the presence of Gr, and confirm its resistance to chemical and thermal treatments during the transfer procedure.

To return to the spectra in Fig. 3.11, it is important to note that the increase of the photoemission intensity from bulk TiO<sub>2</sub> both in Ti 2p and in O 1s spectra after the annealing indicates that the TiO<sub>2</sub> substrate is initially covered by a layer of an electronically dense material which is removed by the thermal treatment. Moreover, the thickness of such layer should be larger than the electron escape depth, which, for the kinetic energy under investigation, is in the range of 0.5 nm – 5 nm. On the other hand, the C 1s is dominated by the sp<sup>2</sup> component arising from the Gr layer both before and after annealing, indicating that graphene is the uppermost layer of our sample, while, the contaminant residuals present on the graphene surface are not enough to screen the signal of the underlying layers. We can therefore conclude that the screening material is trapped between the Gr layer and the TiO<sub>2</sub> substrate. The significant reduction of the H<sub>2</sub>O components in O 1s spectra upon annealing

proves that the enclosed material is composed of liquid water trapped during the transfer process.

### **3.4 Advantage in the use of graphene nanobubbles for *in situ* UHV analysis**

We successfully developed a novel graphene transparent sealed cell based on the formation of GNBs filled with water for *in situ* studies of a liquid environment using conventional electron spectroscopy techniques in UHV conditions.

The process to obtain a disordered array of GNBs is more simple and robust in comparison to “conventional” graphene layers suspended on SiO<sub>2</sub> or Si<sub>3</sub>N<sub>4</sub> patterned membranes. In fact, with this configuration, graphene is not suspended over an orifice, but it is simply transferred on the solid substrate owing the proper wettability for trapping aqueous solution inside GNBs. In this way the system avoids the risk of break or collapse of the graphene layer. In addition, this system is time saving because does not require the fabrication of a micro-patterned support. Another important aspect is that thanks to the elasticity of graphene, the GNB can follow any change in the volume of the system, so that the trapped liquid can be always in contact with the graphene layer even though the solvent may evaporate slowly from defects. Graphene layers suspended on a membrane may not be able to keep the contact with the residual liquid inside the cell in case of leakage, making difficult the measurement of XPS or XAS signals.

The proposed system is a valid, alternative method to measure stable systems in liquid, enabling the electronic characterization of different chemical or physical processes in liquid phase or at the solid/liquid interface.

## References

- [1] Lichterman, M.F., Hu, S., Richter, M.H., Crumlin, E.J., Axnanda, S., Favaro, M., Drisdell, W., Hussain, Z., Mayer, T., Brunschwig, B.S., Lewis, N.S., Liu, Z., Lewerenz, H.-J. *Direct observation of the energetics at a semiconductor/liquid junction by operando X-ray photoelectron spectroscopy* (2015) *Energy and Environmental Science*, 8 (8), pp. 2409-2416.
- [2] Kolmakov, A., Dikin, D.A., Cote, L.J., Huang, J., Abyaneh, M.K., Amati, M., Gregoratti, L., Günther, S., Kiskinova, M. *Graphene oxide windows for in situ environmental cell photoelectron spectroscopy* (2011) *Nature Nanotechnology*, 6 (10), pp. 651-657.
- [3] Velasco-Velez, J.-J., Wu, C.H., Pascal, T.A., Wan, L.F., Guo, J., Prendergast, D., Salmeron, M. *The structure of interfacial water on gold electrodes studied by x-ray absorption spectroscopy* (2014) *Science*, 346 (6211), pp. 831-834.
- [4] Koga, H., Croguennec, L., Ménétrier, M., Mannessiez, P., Weill, F., Delmas, C., Belin, S. *Operando X-ray absorption study of the redox processes involved upon cycling of the li-rich layered oxide  $Li_{1.20}Mn_{0.54}Co_{0.13}Ni_{0.13}O_2$  in Li ion batteries* (2014) *Journal of Physical Chemistry C*, 118 (11), pp. 5700-5709.
- [5] Masuda, T., Yoshikawa, H., Noguchi, H., Kawasaki, T., Kobata, M., Kobayashi, K., Uosaki, K. *In situ x-ray photoelectron spectroscopy for electrochemical reactions in ordinary solvents* (2013) *Applied Physics Letters*, 103 (11), art. no. 111605.
- [6] Chen, Q., Smith, J.M., Park, J., Kim, K., Ho, D., Rasool, H.I., Zettl, A., Alivisatos, A.P. *3D motion of DNA-Au nanoconjugates in graphene liquid cell electron microscopy* (2013) *Nano Letters*, 13 (9), pp. 4556-4561.
- [7] Caneva, S., Weatherup, R.S., Bayer, B.C., Brennan, B., Spencer, S.J., Mingard, K., Cabrero-Vilatela, A., Baehtz, C., Pollard, A.J., Hofmann, S. *Nucleation control for large, single crystalline domains of monolayer hexagonal boron nitride via Si-doped Fe catalysts* (2015) *Nano Letters*, 15 (3), pp. 1867-1875.
- [8] Kolmakov, A., Gregoratti, L., Kiskinova, M., Günther, S. *Recent Approaches for Bridging the Pressure Gap in Photoelectron Microspectroscopy* (2016) *Topics in Catalysis*, 59 (5-7), pp. 448-468.
- [9] Kraus, J., Reichelt, R., Günther, S., Gregoratti, L., Amati, M., Kiskinova, M., Yulaev, A., Vlassiuk, I., Kolmakov, A. *Photoelectron spectroscopy of wet and gaseous samples through graphene membranes* (2014) *Nanoscale*, 6 (23), pp. 14394-14403.

- [10] Wu, C.H., Weatherup, R.S., Salmeron, M.B. *Probing electrode/electrolyte interfaces in situ by X-ray spectroscopies: Old methods, new tricks* (2015) *Physical Chemistry Chemical Physics*, 17 (45), pp. 30229-30239.
- [11] Pan, W., Xiao, J., Zhu, J., Yu, C., Zhang, G., Ni, Z., Watanabe, K., Taniguchi, T., Shi, Y., Wang, X. *Biaxial compressive strain engineering in graphene/boron nitride heterostructures* (2012) *Scientific Reports*, 2, art. no. 893.
- [12] Xuan Lim, C.H.Y., Sorkin, A., Bao, Q., Li, A., Zhang, K., Nesladek, M., Loh, K.P. *A hydrothermal anvil made of graphene nanobubbles on diamond* (2013) *Nature Communications*, 4, art. no. 1556.
- [13] Šuligoj, A., Štanger, U.L., Tušar, N.N. *Photocatalytic air-cleaning using TiO<sub>2</sub> nanoparticles in porous silica substrate* (2014) *Chemical Papers*, 68 (9), pp. 1265-1272.
- [14] Fujishima, A., Honda, K. *Electrochemical photolysis of water at a semiconductor electrode* (1972) *Nature*, 238 (5358), pp. 37-38.
- [15] Fujishima, A., Zhang, X., Tryk, Donald.A. *Heterogeneous photocatalysis: From water photolysis to applications in environmental cleanup* (2007) *International Journal of Hydrogen Energy*, 32 (14), pp. 2664-2672..
- [16] Kudo, A., Miseki, Y. *Heterogeneous photocatalyst materials for water splitting* (2009) *Chemical Society Reviews*, 38 (1), pp. 253-278.
- [17] Inoue, T., Fujishima, A., Konishi, S., Honda, K. *Photoelectrocatalytic reduction of carbon dioxide in aqueous suspensions of semiconductor powders* (1979) *Nature*, 277 (5698), pp. 637-638.
- [18] Fateh, R., Dillert, R., Bahnemann, D. *Self-cleaning properties, mechanical stability, and adhesion strength of transparent photocatalytic TiO<sub>2</sub>-ZnO coatings on polycarbonate* (2014) *ACS Applied Materials and Interfaces*, 6 (4), pp. 2270-2278.
- [19] [www.graphenea.com](http://www.graphenea.com).
- [20] Matruggio, A., Nappini, S., Naumenko, D., Magnano, E., Bondino, F., Lazzarino, M., Dal Zilio, S. *Contamination-free suspended graphene structures by a Ti-based transfer method* (2016) *Carbon*, 103, pp. 305-310.
- [21] Yang, L., Zhang, M., Shi, S., Lv, J., Song, X., He, G., Sun, Z. *Effect of annealing temperature on wettability of TiO<sub>2</sub> nanotube array films* (2014) *Nanoscale Research Letters*, 9 (1), 7 p.
- [22] Gambardella, P., Stepanow, S., Dmitriev, A., Honolka, J., De Groot, F.M.F., Lingenfelder, M., Gupta, S.S., Sarma, D.D., Bencok, P., Stanescu, S., Clair, S., Pons, S., Lin, N., Seitsonen, A.P., Brune, H., Barth, J.V., Kern, K. *Supramolecular control of*

- the magnetic anisotropy in two-dimensional high-spin Fe arrays at a metal interface* (2009) *Nature Materials*, 8 (3), pp. 189-193.
- [23] Repetto, D., Lee, T.Y., Rusponi, S., Honolka, J., Kuhnke, K., Sessi, V., Starke, U., Brune, H., Gambardella, P., Carbone, C., Enders, A., Kern, K. *Structure and magnetism of atomically thin Fe layers on flat and vicinal Pt surfaces* (2006) *Physical Review B - Condensed Matter and Materials Physics*, 74 (5), art. no. 054408.
- [24] Ferretti, N., Balkaya, B., Vollmer, A., Neeb, M., Eberhardt, W. *Inner-shell photoelectron spectroscopy of size-selected Cu-clusters on Si* (2007) *Journal of Electron Spectroscopy and Related Phenomena*, 156-158, pp. 124-127.
- [25] Ferrari, A.C., Basko, D.M. *Raman spectroscopy as a versatile tool for studying the properties of graphene* (2013) *Nature Nanotechnology*, 8 (4), pp. 235-246.
- [26] Ding, F., Ji, H., Chen, Y., Herklotz, A., Dörr, K., Mei, Y., Rastelli, A., Schmidt, O.G. *Stretchable graphene: A close look at fundamental parameters through biaxial straining* (2010) *Nano Letters*, 10 (9), pp. 3453-3458.
- [27] Zabel, J., Nair, R.R., Ott, A., Georgiou, T., Geim, A.K., Novoselov, K.S., Casiraghi, C. *Raman spectroscopy of graphene and bilayer under biaxial strain: Bubbles and balloons* (2012) *Nano Letters*, 12 (2), pp. 617-621.
- [28] Larciprete, R., Colonna, S., Ronci, F., Flammini, R., Lacovig, P., Apostol, N., Politano, A., Feulner, P., Menzel, D., Lizzit, S. *Self-Assembly of Graphene Nanoblisters Sealed to a Bare Metal Surface* (2016) *Nano Letters*, 16 (3), pp. 1808-1817.
- [29] Bae, S., Kim, H., Lee, Y., Xu, X., Park, J.-S., Zheng, Y., Balakrishnan, J., Lei, T., Ri Kim, H., Song, Y.I., Kim, Y.-J., Kim, K.S., Özyilmaz, B., Ahn, J.-H., Hong, B.H., Iijima, S. *Roll-to-roll production of 30-inch graphene films for transparent electrodes* (2010) *Nature Nanotechnology*, 5 (8), pp. 574-578.
- [30] Lee, J., Kim, Y., Shin, H.-J., Lee, C., Lee, D., Moon, C.-Y., Lim, J., Chan Jun, S. *Clean transfer of graphene and its effect on contact resistance* (2013) *Applied Physics Letters*, 103 (10), art. no. 103104.
- [31] Chu, D., Younis, A., Li, S. *Direct growth of TiO<sub>2</sub> nanotubes on transparent substrates and their resistive switching characteristics* (2012) *Journal of Physics D: Applied Physics*, 45 (35), art. no. 355306.
- [32] Xing, M., Shen, F., Qiu, B., Zhang, J. *Highly-dispersed Boron-doped graphene nanosheets loaded with TiO<sub>2</sub> nanoparticles for enhancing CO<sub>2</sub> photoreduction* (2014) *Scientific Reports*, 4, art. no. 6341.

- [33] Yang, D., Velamakanni, A., Bozoklu, G., Park, S., Stoller, M., Piner, R.D., Stankovich, S., Jung, I., Field, D.A., Ventrice Jr., C.A., Ruoff, R.S. *Chemical analysis of graphene oxide films after heat and chemical treatments by X-ray photoelectron and Micro-Raman spectroscopy* (2009) *Carbon*, 47 (1), pp. 145-152.
- [34] Tissot, H., Gallet, J.-J., Bournel, F., Olivieri, G., Silly, M.G., Sirotti, F., Boucly, A., Rochet, F. *The Electronic Structure of Saturated NaCl and NaI Solutions in Contact with a Gold Substrate* (2016) *Topics in Catalysis*, 59 (5-7), pp. 605-620.
- [35] Ketteler, G., Yamamoto, S., Bluhm, H., Andersson, K., Starr, D.E., Ogletree, D.F., Ogasawara, H., Nilsson, A., Salmeron, M. *The nature of water nucleation sites on TiO<sub>2</sub>(110) surfaces revealed by ambient pressure X-ray photoelectron spectroscopy* (2007) *Journal of Physical Chemistry C*, 111 (23), pp. 8278-8282.
- [36] Li, L., Yan, J., Wang, T., Zhao, Z.-J., Zhang, J., Gong, J., Guan, N. *Sub-10 nm rutile titanium dioxide nanoparticles for efficient visible-light-driven photocatalytic hydrogen production* (2015) *Nature Communications*, 6, art. no. 5881.
- [37] Pei, Z., Ding, L., Feng, W., Weng, S., Liu, P. *Defect self-doped TiO<sub>2</sub> for visible light activity and direct noble metal anchoring* (2014) *Physical Chemistry Chemical Physics*, 16 (39), pp. 21876-21881.





# Chapter 4

## 4.1 Graphene nanobubbles on TiO<sub>2</sub> for *in situ* electron spectroscopy of liquid-phase chemical reactions

In the Chapter 3, the realization of GNBs filled with water for *in situ* electron spectroscopy analysis has been described. The possibility to fill the GNBs with the desired solution, enables the investigation of the electronic mechanisms at the base of liquid/solid electronic transfer in processes such as catalysis, energy conversion processes, water splitting and so on.

In a very recent work, Nair's group fabricated GNBs trapping different salts (MgCl<sub>2</sub>, CuSO<sub>4</sub>, Ca(OH)<sub>2</sub>) between two graphene layers [1]; the chemical reaction of salts with water was promoted by pressure and led to the formation of the 2D crystals of the corresponding oxides. The reaction was monitored by Raman spectroscopy at room temperature and TEM analysis. To the best of our knowledge, this represents the only study in literature of chemical reaction inside GNBs. In the mentioned experiment, however, GNB are used to confine the liquid phase into a high pressure environment. On the other hand, as already shown in Chapter 3, GNB allow the application of UHV-based analytical techniques, which could not be used otherwise to investigate the properties of liquid systems. Since techniques such as XPS or XAS spectroscopy can provide unique knowledges in liquid/solid interface investigation, we decide to demonstrate the application GNBs as a sealed cell to follow the dynamic of a few demonstrative chemical reactions. Two reactions will be analyzed, one promoted by the temperature (reduction of Fe in a FeCl<sub>3</sub> solution) and one promoted by UV light (reduction of Fe in a Prussian Blue solution), monitoring *in situ* the reactions in a liquid environment.

## 4.2 *In situ* study of liquid-phase thermal reduction of FeCl<sub>3</sub> solution

Iron-based compounds are red-ox species at the base of many biologic processes, such as respiration [2], nitrogen fixation [3], and photosynthesis [4], and of high relevance in several technological processes such as fuel cells [5] and galvanic corrosion phenomena [6]. For these reasons, we decided to follow the chemistry of the thermal-induced reduction of Fe in a FeCl<sub>3</sub> aqueous solution trapped inside the GNBs as a proof of the possible use of this system for *in situ* studies. This choice was also dictated by the easiness of its implementation: indeed, a solution based on diluted FeCl<sub>3</sub> is used to etch Cu for CVD-grown graphene transfer, as described in Chapter 2, therefore its trapping inside GNB was of easy implementation.

The thermal decomposition of FeCl<sub>3</sub> produce FeCl<sub>2</sub> + Cl<sub>2</sub> and takes place at temperature near to 200°C [7]. Therefore, to promote the chemical reaction, the system was annealed to 250°C for 1 h with two purposes, check the GNB thermal stability and follow the thermal induced reduction process from Fe<sup>3+</sup> to Fe<sup>2+</sup>. The reaction has been analyzed with XPS and XAS, measuring the electronic states of Cl, Fe and O obtained through a combination of electron spectroscopies in the different phases of the process.

### 4.2.1 Sample preparation

Following the same protocol showed in the Chapter 3 for the fabrication of GNBs, a solution 1.6 M of FeCl<sub>3</sub>·(H<sub>2</sub>O)<sub>6</sub> (Sigma-Aldrich, ACS reagent, 97%) is trapped between GNBs and a TiO<sub>2</sub> (100) rutile single crystal substrate, just by skipping the rinsing procedure with DI water. Commercially available CVD grown graphene on Cu is used [8]. Till the end of the process, the graphene surface is covered by 250 nm-thick layer of mr-I 7020, and it never gets in contact with the etching solution. Therefore, as already shown in Chapter 3, XAS at the Fe L<sub>3,2</sub>-edge measured on GNBs filled with water shows that no unintentionally deposition of Fe may result from this process [9]. Fig. 4.1 shows a cartoon of the final configuration of the fabricated sample.

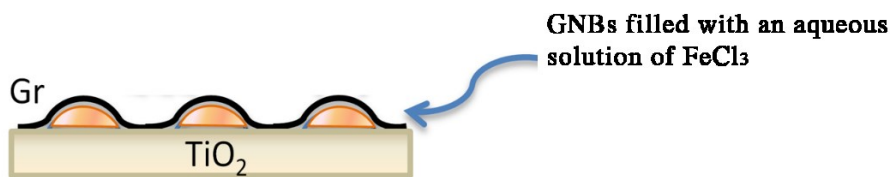


Fig. 4.1: cartoon of the fabricated sample: the diluted  $\text{FeCl}_3$  solution is trapped in GNBs on  $\text{TiO}_2$  substrate.

#### 4.2.2 X-ray electron spectroscopy of $\text{FeCl}_3$ solution in graphene nanobubbles

We performed x-ray measurements at the CNR BACH beamline at Elettra Sincrotrone in Trieste. The chemical features of the GNBs containing  $\text{FeCl}_3$  has been investigated by XPS and XAS. Two photon energies have been used for the scope, 596 eV and 1049 eV in order to change the surface sensitivity and disentangle the surface/vacuum interface from the bulky contributions.

**Surface sensitivity**

When a monochromatic primary beam of electrons is incident on a surface, the intensity of the primary electrons  $I_0$  is damped as function of the distance  $d$  into the solid:

$$I(d) = I_0 e^{-d/\lambda(E)}$$

where  $I(d)$  is the electron intensity after the travel through the solid.  $\lambda(E)$  is the inelastic mean free path (IMFP) of the electrons, described from the universal curve. Between 54 and 500 eV of electron energy, there is the maximum of the surface sensitivity.

In order to confirm the presence of the liquid inside GNBs and to confirm the presence of  $\text{FeCl}_3$  in solution we measured XPS O 1s and Cl 2p core-level photoemission spectra. The results are showed in Fig. 4.2a and b, respectively. The spectra have been normalized to their maximum intensity and a Shirley background to account for the inelastic photoelectrons have been subtracted.

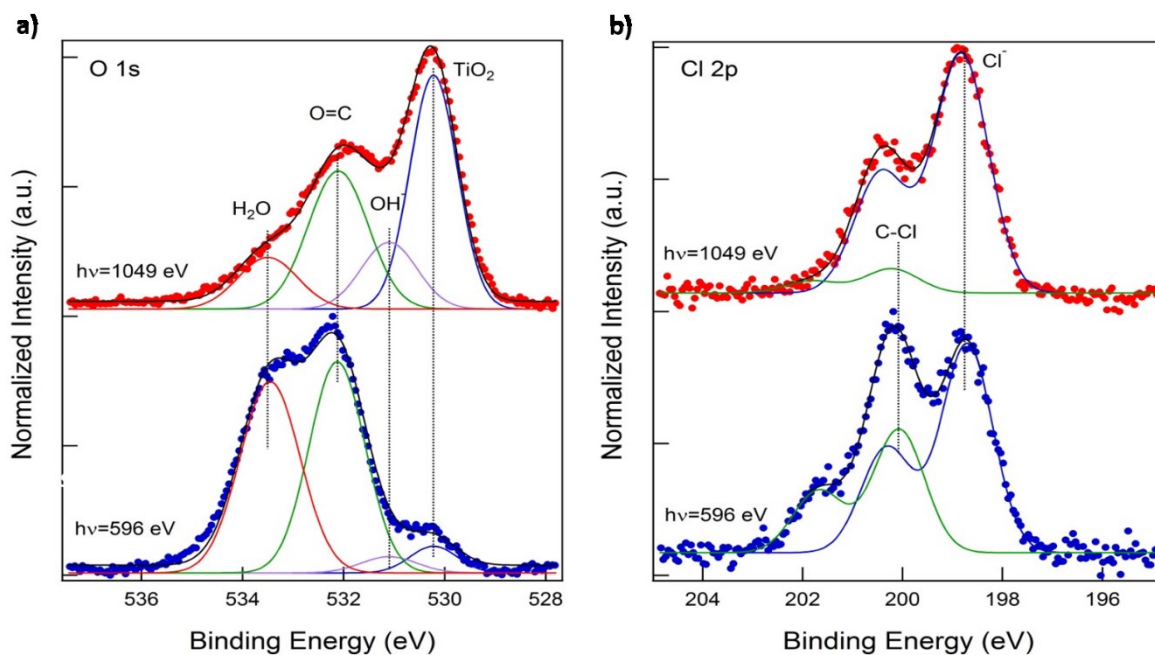


Fig. 4.2: XPS spectra of a) O1s and b) Cl 2p of GNBs filled with an aqueous solution of FeCl<sub>3</sub> (1.6 M) acquired using a surface-sensitive photon of 596 eV in energy (blue curves) and a more bulk sensitive photon of 1049 eV in energy (red curves).

As observed for GNBs filled with water, the O 1s peaks can be deconvoluted in four components: the one at 533.5 eV is related to liquid water, as already shown in the previous chapter [10, 11]; the component at 532.5 eV can be related to graphene surface contamination (C-O, C-OH), the one at 531.4 eV is related to hydroxyl radicals (OH) at the TiO<sub>2</sub> surface, and finally, the one at 530.5 eV is related to bulk TiO<sub>2</sub>. As expected, higher is the used energy, more bulk sensitive is the photon, and consequently higher is the intensity of the component associated to bulk TiO<sub>2</sub>. Surprisingly, the H<sub>2</sub>O/C=O ratio decreases with bulk sensitive photons; this is something unexpected, because we expected to have less sensitivity to the water/graphene interface. Our hypothesis is that the two spectra are taken in two different position on the sample and spectrum at higher energy is taken in an area with a smaller density of GNBs; consequently, the components associated to H<sub>2</sub>O is lower respect to an area with a higher number on bubbles.

Cl 2p spectra consist of two spin-orbits doublets: the first peaked at 198.7 eV and 200.3 eV is attributed to Cl<sup>-</sup> ions in solution, the second peaked at 200.1 eV and 201.7 is attributed to the formation of Cl-C bond at the graphene interface [12, 13]. With the surface sensitive photon energy of 596 eV, the intensity of the component associated to Cl atoms bound to

the graphene layer is higher; while using the bulk sensitive photon energy of 1049 eV, the intensity of the Cl<sup>-</sup> component is stronger, in agreement with the hypothesis that the liquid solution of FeCl<sub>3</sub> that contains the Cl<sup>-</sup> ions is confined between graphene and TiO<sub>2</sub>.

#### 4.2.3 X-ray electron spectroscopy of Fe reduction inside graphene nanobubbles

To promote the Fe reduction from Fe<sup>3+</sup> to Fe<sup>2+</sup>, the system was annealed at 250°C for 1 h *in situ*, without transferring the sample to a different experimental system. The C1s and the Fe 2p spectra acquired before and after the thermal treatment are shown in Fig. 4.3a and b, respectively.

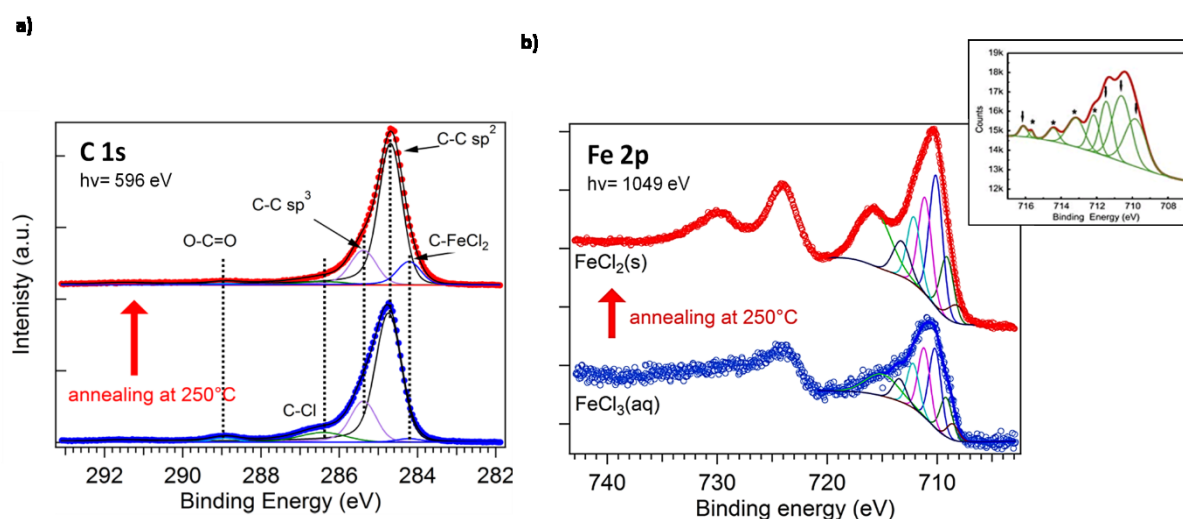


Fig. 4.3: XPS spectra of a) C1s and b) Fe 2p before (blue spectrum) and after the annealing (red spectra). The spectra in a) are recorded using a photon energy of 596 eV, while the spectra in b) are recorded with photon energy of 1040 eV. The inset in b) shows the XPS Fe 2p spectrum for polyacrylonitrile/ferrous chloride nanofibers, taken from ref. [14] for comparison: arrows correspond to the Fe 2p in Fe(II), dots correspond to Fe 2p in Fe(III).

Upon annealing the intensity signal C 1s does not show a strong intensity change. However, a decrease of the C-C sp<sup>3</sup> component intensity can be observed that we attributed to the removal of polymer contaminants as already shown in the Chapter 3. Moreover, a new peak at 284.1 eV appears, showing the presence of a C-FeCl<sub>2</sub> component.

The analysis of the Fe 2p core level after the annealing shows the Fe in a 2+ oxidation state, which is the appearance of features characteristic of solid FeCl<sub>2</sub> [15]. The 2p<sub>3/2</sub> peak of both Fe spectra can be fitted using several components and the fitting values obtained for the annealed sample are in good agreement with those of FeCl<sub>2</sub> reported in literature [14].

To confirm the obtained results, we analyzed the oxidation state of Fe ions also by recording the XAS spectra at the Fe L<sub>3,2</sub>-edge in total electron yield (TEY), measuring the current on the graphene layer, before and after the annealing. The spectra are reported in Fig. 4.4 and are obtained before (blue curve) and after the annealing (red curve). Both spectra are compared with a simulation obtained with the Ligand Field Multiplet (LFM) approach (grey curves) [16]. The effects of  $\sigma$ - and  $\pi$ -donation from water to Fe ions were not accounted in these simulations.

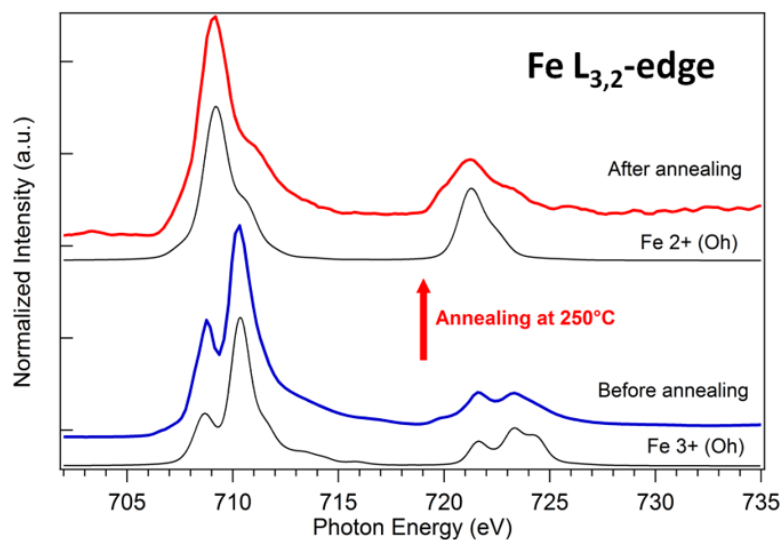


Fig. 4.4: XAS spectra of the Fe L<sub>3,2</sub>-edge measured on GNBs filled with FeCl<sub>3</sub> solution before (blue curve) and after the annealing at 250°C (red curve). Calculated LFM spectra (grey curves) of Fe<sup>3+</sup> (before annealing) and Fe<sup>2+</sup> (after annealing) are reported together with the corresponding experimental data.

Before annealing, the simulated spectrum accurately reproduces the main features of the experimental data assuming the Fe<sup>3+</sup> in an octahedral (O<sub>h</sub>) configuration typical of FeCl<sub>3</sub> compounds [17]. As expected, the iron L<sub>3</sub>-edge of FeCl<sub>3</sub> consists of a main peak at 710.5 eV and a pre-peak at 708.7 eV in the L<sub>3</sub>-edge, and by two components at 721.8 and 723.5 eV (and a shoulder at 720 eV) in the L<sub>2</sub>-edge. After annealing, the spectrum dramatically

changes to a conformation typical of Fe(II) compounds [18], which is composed by a main peak at 709.8 eV and a small shoulder at 711.5 eV, while the L<sub>2</sub>-edge has a main component at 721.4 eV and two small shoulders at 720.5 and 723.6 eV. The simulation, assuming the Fe<sup>2+</sup> in O<sub>h</sub> configuration, reproduces quite well the experimental spectrum expected for FeCl<sub>2</sub> [19], thus confirming the thermal induced reduction of Fe from 3<sup>+</sup> to 2<sup>+</sup>.

To prove that the thermal-induced reduction of FeCl<sub>3</sub> to FeCl<sub>2</sub> occurs only if the molecules are in liquid phase, Fe L<sub>3,2</sub>-edge XAS spectra were also acquired on a dry film of FeCl<sub>3</sub>·(H<sub>2</sub>O)<sub>6</sub> prepared by drop casting on a Si wafer as a function of the annealing temperature. The results are shown in Fig. 4.5.

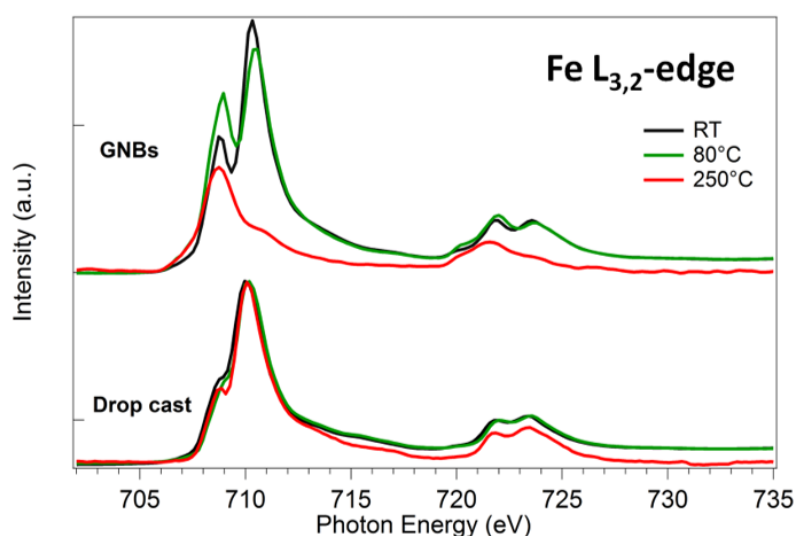


Fig. 4.5: XAS spectra of the aqueous solution (top spectra) and dry film (bottom spectra) of FeCl<sub>3</sub>(H<sub>2</sub>O)<sub>6</sub> measured at different temperature: RT (black curve), 80°C (green curve), and 250°C (red curve).

From the spectra, it is clear that the oxidation state of the dry film does not change upon annealing, while it gradually switches from 3<sup>+</sup> to 2<sup>+</sup> in the case of the aqueous solution. It is interesting to notice that upon annealing at 80°C the spectrum still indicates the presence of the water component and the oxidation state of Fe is a mixture of 3<sup>+</sup> and 2<sup>+</sup> ions. Heating up to 250°C, the temperature induces the complete Fe<sup>3+</sup> reduction to Fe<sup>2+</sup> and the evaporation of water. On the contrary, in the drop cast of FeCl<sub>3</sub>·(H<sub>2</sub>O)<sub>6</sub> the Fe reduction does not occur and the dry film undergoes a different thermal dehydration and decomposition mechanism that lead to the formation of oxide species such as Fe(OH)Cl<sub>2</sub>, FeOOH and Fe<sub>2</sub>O<sub>3</sub>, as already



widely investigated in literature [20]. A cartoon which summarize the process in GNBs is shown in Fig. 4.6.

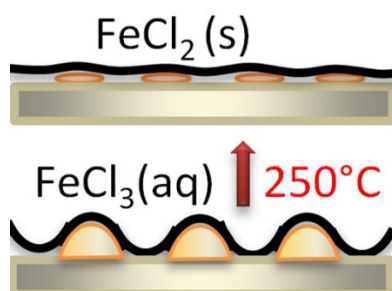


Fig. 4.6: scheme of the process before and after the annealing at 250 °C.

Fig. 4.7 shows a summary scheme of the proposed thermal decomposition mechanisms for  $\text{FeCl}_3$  aqueous solution (Fig. 4.7a) and  $\text{FeCl}_3$  dry film (Fig. 4.7b).

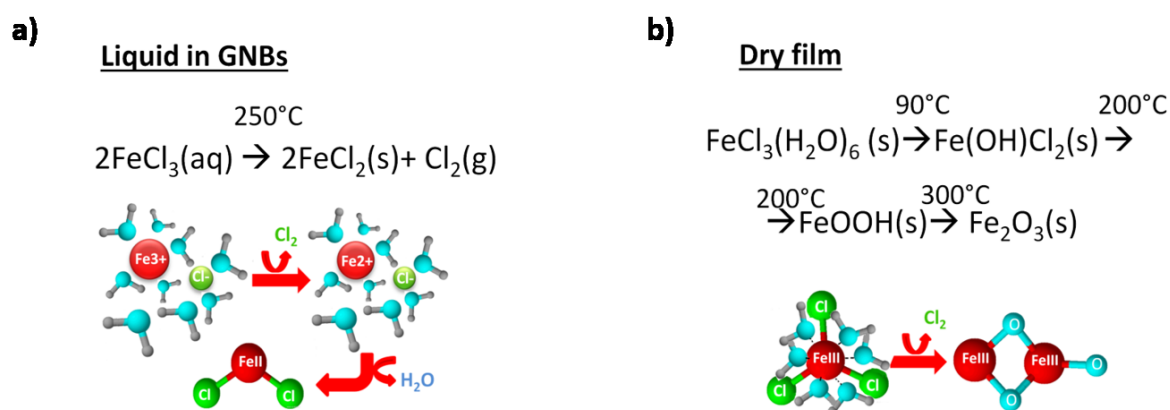


Fig. 4.7: schematic representation of the proposed thermal decomposition mechanisms for a)  $\text{FeCl}_3$  aqueous solution and b)  $\text{FeCl}_3$  dry film.

This study demonstrated that the use of GNBs enables the application of UHV-based spectroscopies to follow the dynamics of a chemical reduction which occurs in the liquid phase. To this purpose we designed the simplest possible experiment, using  $\text{FeCl}_3$ , which did not require extra processing step with respect to the fabrication described in Chapter 3 (indeed, it reduced the process complexity by one step, the rinsing procedure), and used temperature as an external input, that was already implemented on the BACH beamline and thus did not required extra instrumental efforts. However, the use of GNB is general and can

be applied to a large number of chemical reactions. To demonstrate the general character of this approach, we followed the dynamic of a chemical reduction in GNBs promoted by UV light. The experiment and the results are presented in the next sections.

### 4.3 *In situ* study of liquid-phase UV reduction of Prussian Blue

To demonstrate the adaptability of GNBs for a different kind of study, we decided to analyze the photoreduction of the Prussian Blue (PB) starting from its soluble form  $K[Fe^{III}Fe^{II}(CN)_6]$  [21]. The interest in PB derives from its use in a lot of applications, such as material in photomagnetic devices [22], electroactive layer in electrochemistry [23], cathode material for battery [24], and electrode in biosensors [25]. PB is characterized by interesting photomagnetic properties that can be attributed to photoinduced electron transfer processes leading to changes in the oxidation and spin state of Fe. Indeed, upon UV light exposure the electrons promoted in the conduction band of ferromagnetic PB can be reduced leading to the paramagnetic colorless Everitt's salt, well known as Prussian White (PW) [25] with formula  $K_2[Fe^{II}Fe^{II}(CN)_6]$ ; partial or complete oxidation leads to the Berlin Green (or Prussian Green) with formula  $KFe^{III}[Fe^{II}(CN)_6] \cdot Fe^{III}[Fe^{III}(CN)_6]$  and  $Fe^{III}[Fe^{III}(CN)_6]$ , respectively [26].

Photoinduced electron transfer of PB was already studied on  $TiO_2$  nanosheets by Fourier transform infrared spectroscopy upon light irradiation at room temperature. It was observed that the electron transfer occurs only in presence of a water environment [25]; upon UV band gap excitation of  $TiO_2$ , holes and electrons are generated in the valence band and the conduction band, respectively. The electron transfer requires the presence of water, which acts as scavenging reagent to reduce the generated holes in the valence band, preventing that the electrons excited to the conduction band could be easily recombined with holes [27]. The photoexcited electrons from  $TiO_2$  are injected into PB to reduce  $Fe^{III}$  to  $Fe^{II}$  atoms, and convert it into PW. A scheme of the process is shown in Fig. 4.8.

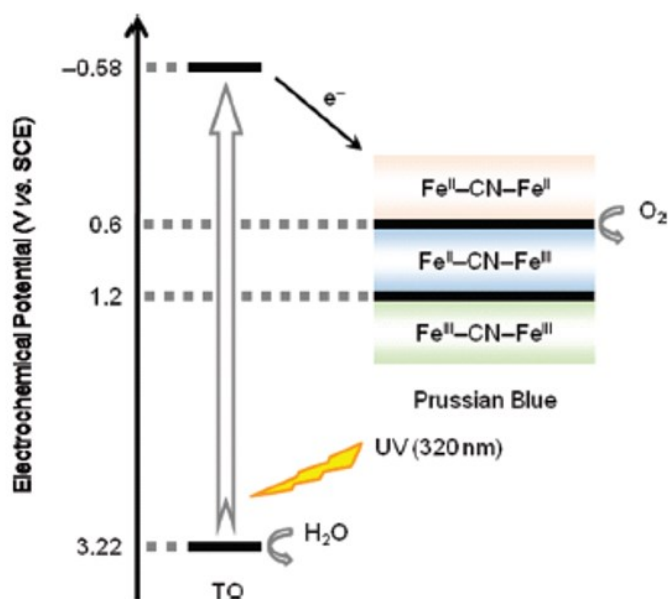
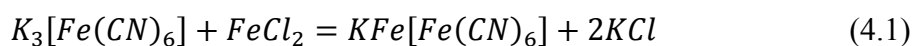


Fig. 4.8: schematic energy diagram of photoinduced electron process in the TO Nanosheets/Prussian Blue Ultrathin Films [25].

We decided to use GNBs to analyze the photoreduction of PB *in situ*. GNBs on TiO<sub>2</sub> single crystal filled with PB are compared with a dry sample of PB on TiO<sub>2</sub> in order to compare the effect of the presence of water on the photoreduction process. Photoreduction is induced *in situ* using an UV laser at 395 nm of wavelength at 15 mW for different intervals of time. XPS and XAS electron spectroscopy have been used to monitoring the reaction; Raman spectroscopy has been performed to confirm the obtained results.

#### 4.3.1 Sample preparation

GNBs filled with the PB solution on a TiO<sub>2</sub> (100) rutile single crystal substrate have been fabricated. The PB solution is prepared with 6.58 mg of K<sub>3</sub>[Fe(CN)<sub>6</sub>] (Potassium ferri-cyanide, Sigma Aldrich), with the addition of 0.97 gr of FeCl<sub>2</sub>·4H<sub>2</sub>O (Iron(II) chloride tetrahydrate, Sigma Aldrich), in 20 ml of DI water. The final PB solution is diluted 10 times. The reaction is described by the (4.1):



A picture of the starting and the final solutions is shown in Fig. 4.9.

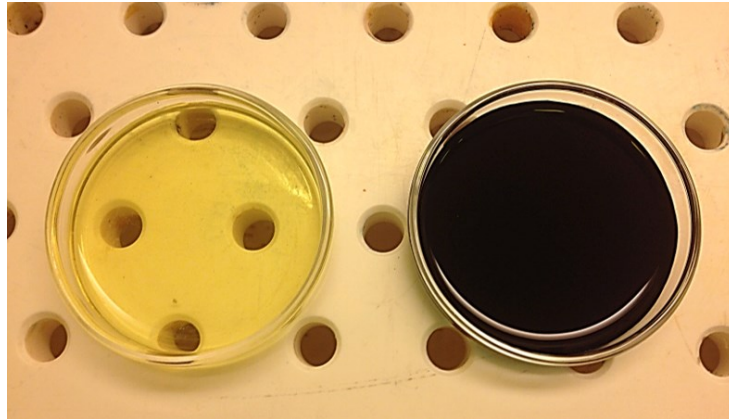


Fig. 4.9: the starting Potassium ferri-cyanide solution (yellow) and the final PB solution (dark blue).

CVD grown graphene on Cu is provided by the Department of Physics of Bilkent University in Ankara, Turkey. I characterized the graphene as-grown by SEM and Raman spectroscopy at IOM-CNR laboratory. The SEM images and the Raman spectrum are shown in Fig. 4.10a and b, respectively. The Raman spectrum is obtained with the excitation wavelength of 532 nm and with laser power on the sample of 1 mW.

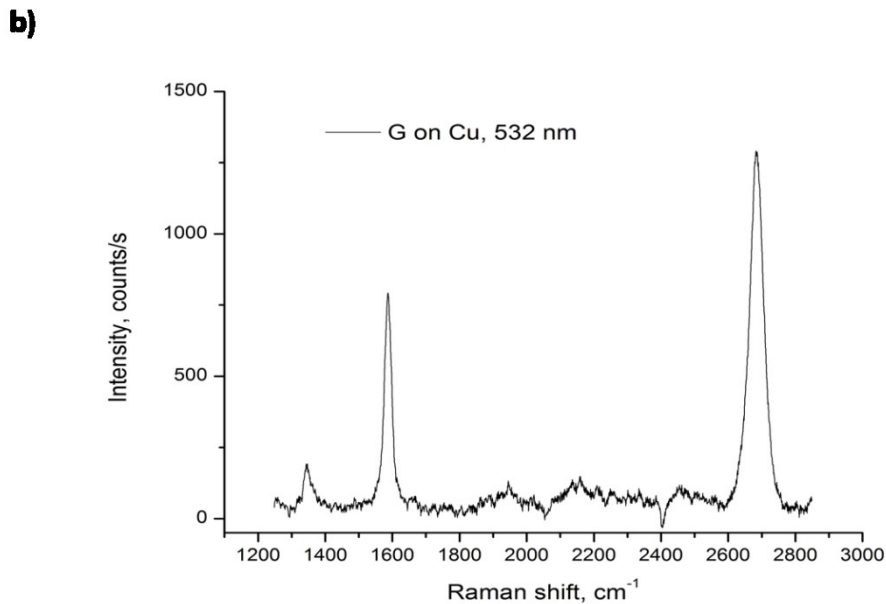
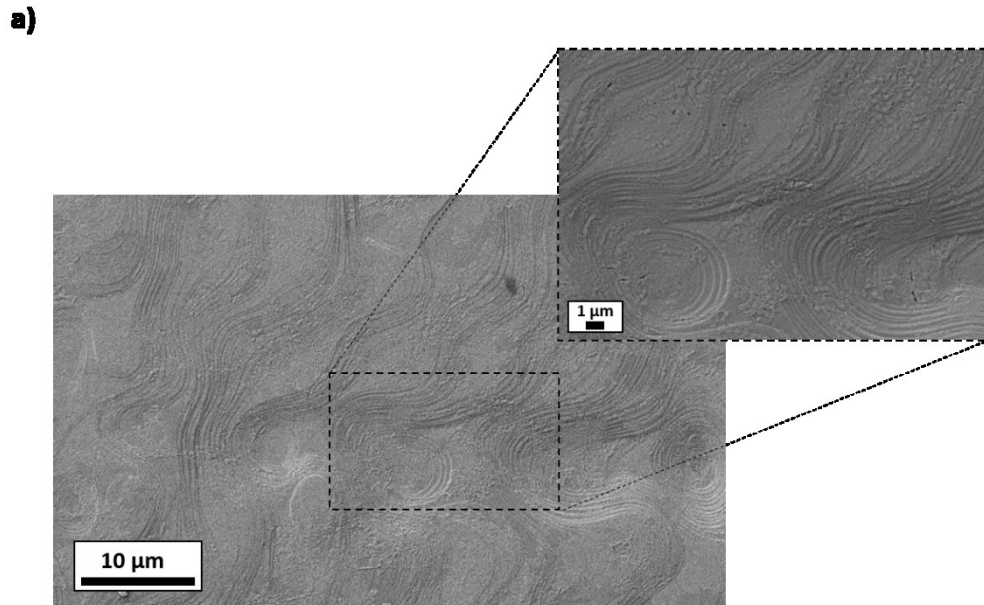


Fig. 4.10: characterization of CVD graphene as-grown on Cu. a) SEM image and b) Raman spectrum.

As shown in Fig. 4.10a, thanks to graphene electron transparency, the Cu surface morphology is visible, and graphene cover clear Cu steps. This is an aspect already observed with commercial CVD grown graphene, as shown in the chapter 2. The Raman spectrum in Fig. 4.10b indicates a good quality, monolayer graphene, with a little D peak which suggests the existence of a low quantity of defects due to grain boundaries and lattice defects.

For the samples preparation, the same procedure described in the paragraph 4.2.1 was adopted. After the deposition of 250 nm of mr-I 7020 on graphene, the Cu is etched and the graphene/polymer membrane is rinsed several times in DI water and transferred in the PB solution. The membrane is fished with a TiO<sub>2</sub> (100) rutile single crystal substrate directly in the solution, allowing the formation of GNBs.

Moreover, two dry samples are prepared with drop casting method, one with a drop of PB on TiO<sub>2</sub> single crystal and one on Cu in order to analyze the role of water.

### 4.3.2 Photoreduction of Prussian Blue inside graphene nanobubbles

X-ray measurements have been performed at the CNR BACH beamline at Elettra Sincrotrone in Trieste. To be sure of the presence of the aqueous solution inside the GNBs, we measured XPS O1s spectra detected at 594 eV in binding energy. The spectra are taken before the UV irradiation and after 45 minutes of irradiation and are shown in Fig. 4.11:

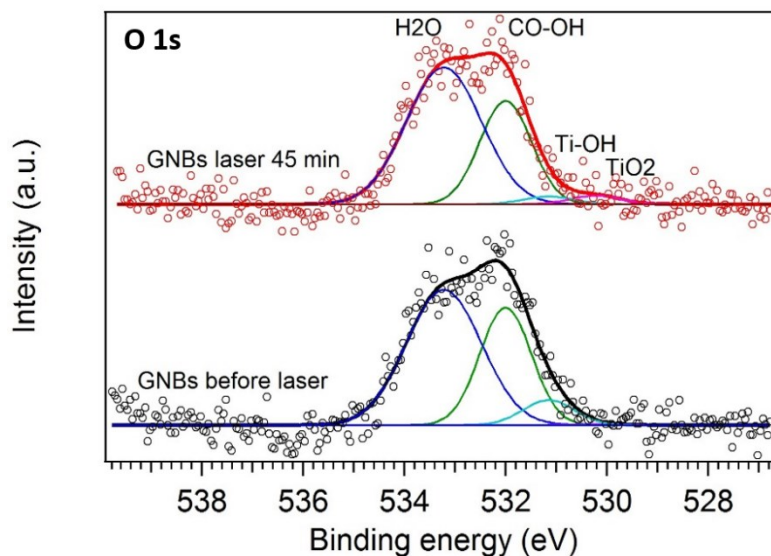


Fig. 4.11: XPS O1s spectra of GNBs obtained before the UV irradiation (black curve) and after 45 minutes of irradiation (red curve).

As previously reported for the GNBs filled with FeCl<sub>3</sub> solution and in chapter 3, the O 1s peaks can be deconvoluted in four components. The component at 533.5 eV is related to liquid water and do not change after UV irradiation, demonstrating the sealing of the cell.

The component at 531.9 eV can be associated to the graphene contaminations CO-OH, due to atmospheric contamination or polymer residuals, present in both spectra. The component at 531 eV can be related to hydroxyl radicals (OH) at the TiO<sub>2</sub> surface and finally, the component at 530.1 eV is related to bulk TiO<sub>2</sub>; this latter is very low due to the dense media interposed between the TiO<sub>2</sub> substrate and the graphene.

XPS C1s spectra before and after 45 minutes of irradiation are taken to check the graphene condition. The obtained spectra are shown in Fig. 4.12:

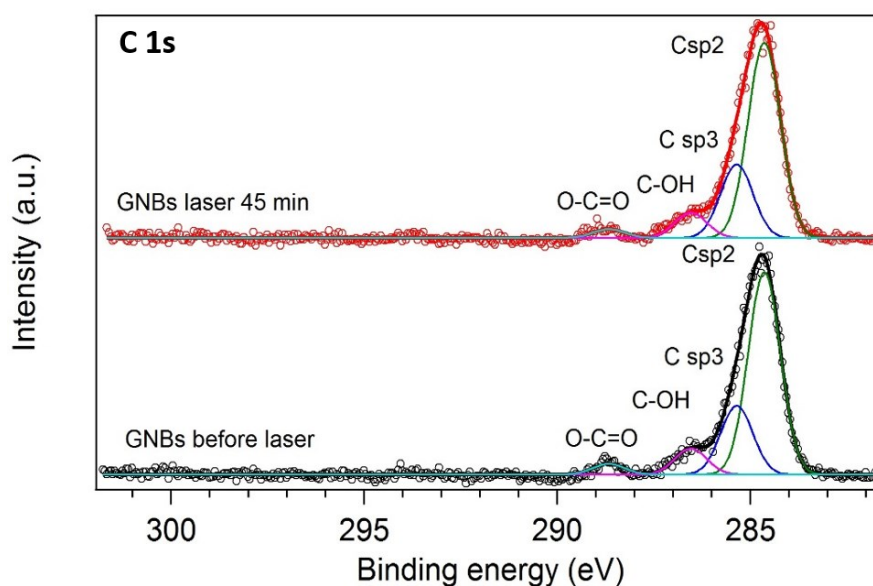


Fig. 4.12: C1s XPS spectra of GNBs before (black curve) and after 45 minutes of UV irradiation at 395 eV (red curve).

Fig. 4.12 shows that the UV irradiation do not change graphene components. Before and after irradiation, C 1s spectra present a pronounced sp<sup>2</sup> component at 284.6 eV, associated to high quality graphene, a sp<sup>3</sup> component at 285.3 eV associate to defects in the lattice and grain boundaries and C-OH and O-C=O components at 286.5 eV and 288.e eV due to atmospheric contamination and polymer residuals. The irradiation does not introduce additional defects or damage into the graphene; indeed, a little decrease of the O-C=O components are visible, indicating a cleaning effect of the UV laser [28].

PB photoreduction was examined by XAS at the Fe L<sub>3,2</sub> edge measured in TEY through the graphene membrane. Spectra are measured at different intervals of times: before the irradiation (black spectrum), after 20 minutes of irradiation (green spectrum), after 40

minutes of irradiation (blue spectrum) and after 70 minutes of irradiation (red spectrum). The spectra are shown in Fig. 4.13:

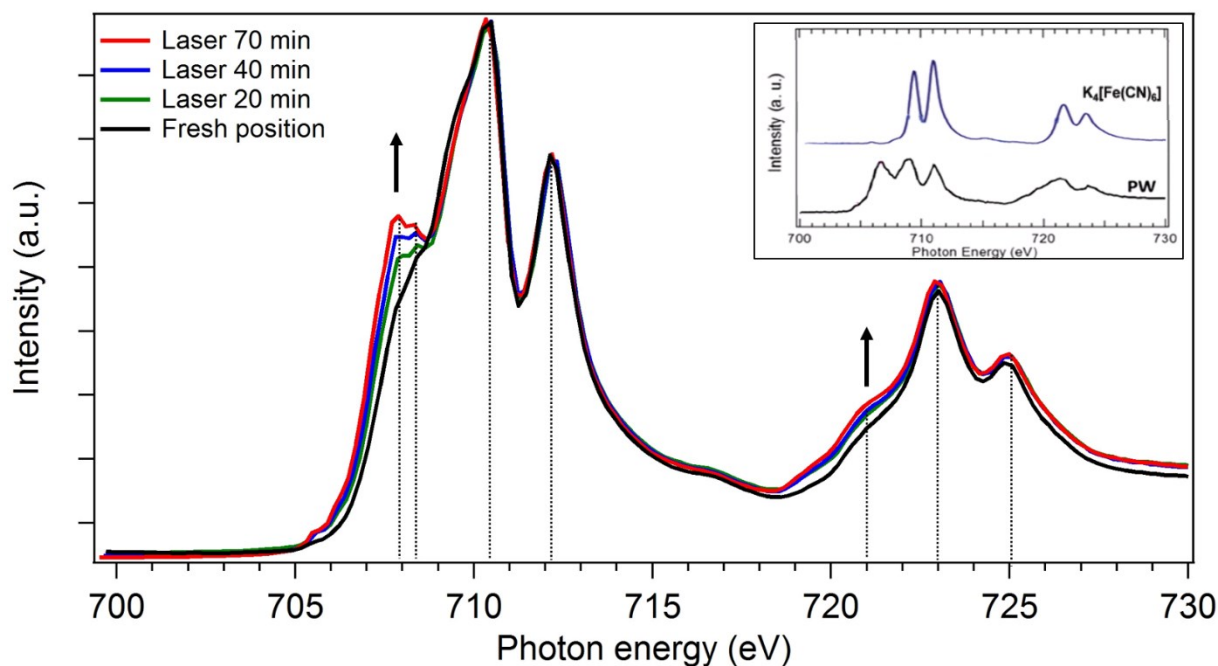


Fig. 4.13: XAS spectra of Fe L<sub>3,2</sub> edge measured: before the irradiation (black), after 20 minutes of irradiation (green), after 40 minutes of irradiation (blue) and after 70 minutes of irradiation (red). The inset show typical XAS spectra of PW (black curve) [29] and PB (blue curve) [30].

Before irradiation, Fe XAS spectrum has the typical shape of PB [30]. Upon 20 minutes of UV irradiation the XAS spectrum shows a change in the direction of a configuration typical of reduced Fe species [29]: PB (Fe<sup>III</sup>-CN-Fe<sup>II</sup>) evolves to PW (Fe<sup>II</sup>-CN-Fe<sup>II</sup>), as shown by the increase of the peaks at 708 eV and 721 eV as indicated. A typical XAS spectra of PW is taken from the reference [29] and shown in the inset for comparison. These results indicate that the reduction takes place and continues under the UV exposition.

To affirm that the reduction is due to the UV irradiation, we need to exclude the x-rays contribution. I prepared a new fresh sample of GNBs on TiO<sub>2</sub> filled with PB, following the same protocol of the previous one. The sample was exposed only to the x-ray beam for 45 minutes without the laser irradiation. The obtained XAS Fe L<sub>3,2</sub> edge spectrum is compared with the one obtained under 45 minutes of UV irradiation with the x-ray beam switched off.



The only contribution due to x-rays is during the measurements, but the exposition time is reduced to the time of measurement (5 minutes). The results are shown in Fig. 4.14.

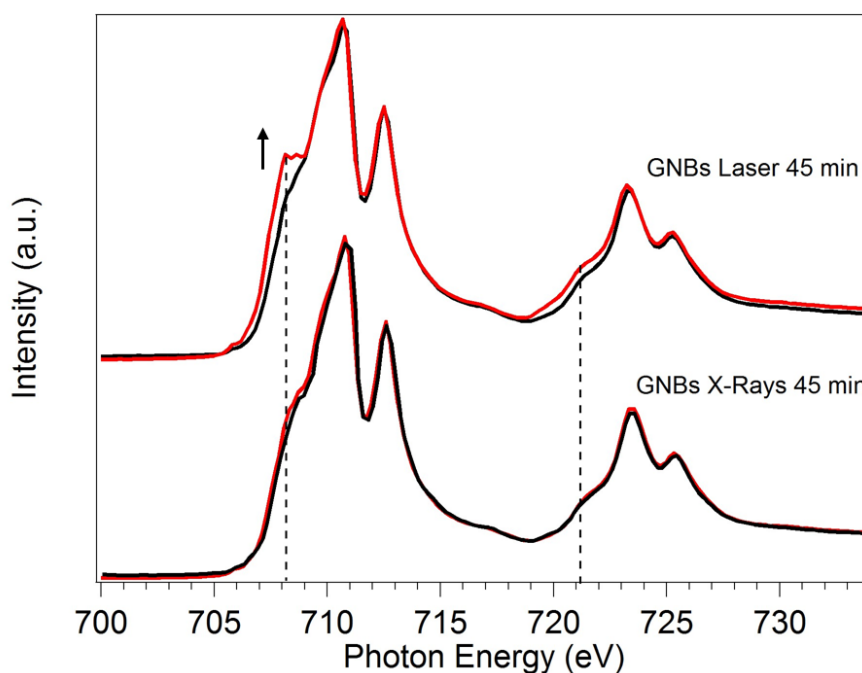


Fig. 4.14: XAS Fe  $L_{3,2}$  edge spectra obtained on GNBs filled with PB and exposed for 45 minutes to x-rays (bottom spectra) and for 45 minutes to UV irradiation (upper spectra).

The black and red spectra are measured before and after the irradiation, respectively.

As visible in Fig. 4.14, after 45 minutes of UV irradiation the peaks at 708 eV and at 721 eV start to increase approaching to the shape reported for the PW (as described before). This indicate that the Fe reduction starts. In case of x-ray irradiation, no evident change in the Fe  $L_{3,2}$  edge are visible after 45 minutes of exposition, confirming that the main factor responsibly of the reduction is the UV light.

To prove the requirement of the water environment, we compared the XAS spectra of Fe  $L_{3,2}$  on GNBs with a dry sample. The sample is prepared with drop casting method with a drop of PB on  $TiO_2$ . The sample are irradiated for 20 minutes, which is a sufficient time for the observation of Fe reduction (as previously shown in Fig. 4.13). The obtained results are shown in Fig. 4.15.

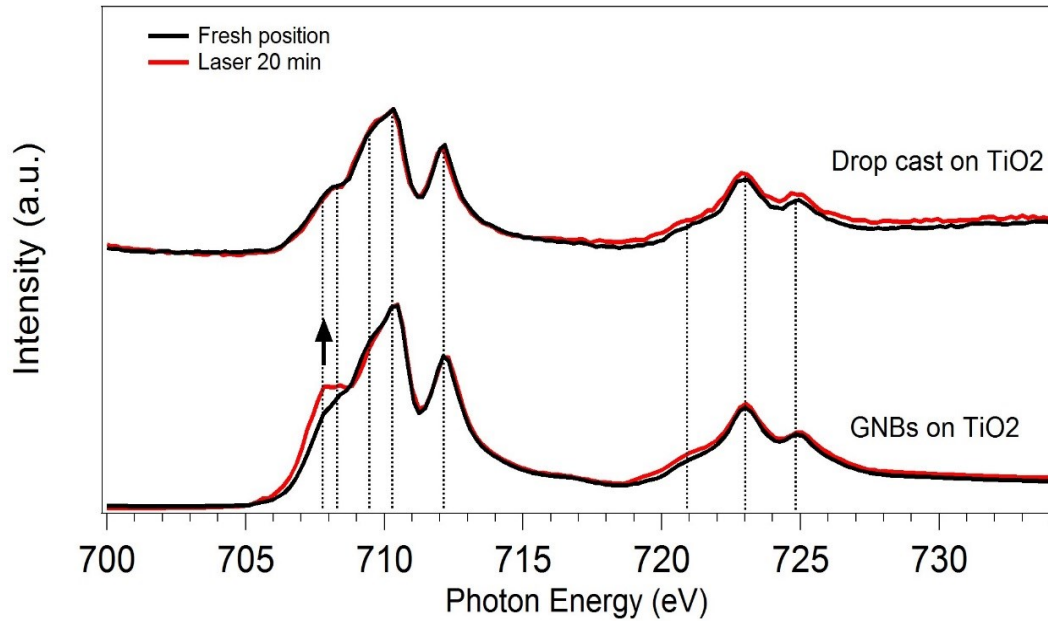


Fig. 4.15: XAS Fe  $L_{3,2}$  edge spectra obtained after 20 minutes of UV exposition on: GNBs on  $TiO_2$  filled with PB (bottom spectra), PB drop cast on  $TiO_2$  (upper spectra). The black and red spectra are measured before and after the irradiation, respectively.

GNBs on  $TiO_2$  shown Fe reduction after UV irradiation. On the contrary, with a drop cast on  $TiO_2$  any reduction occurs, suggesting that the water environment is necessary for the chemical reduction and that the GNB approach could ensure this condition.

The obtained results are confirmed by Raman measurements. Raman spectra are acquired using 100x objective (0.8NA) and a wavelength of 532 nm. All the spectra are acquired by scanning the sample in  $20 \times 20 \mu m^2$  area. Fig. 4.16 shows Raman spectra of a fresh sample of GNBs (black spectrum) and after 15 hours of exposition to UV light (laser at 395 nm, 15 mW of power) (red spectrum). The spectra are compared with PB on glass, which can be used as a reference of a dry sample, since glass substrate does not show Raman peaks in that range.

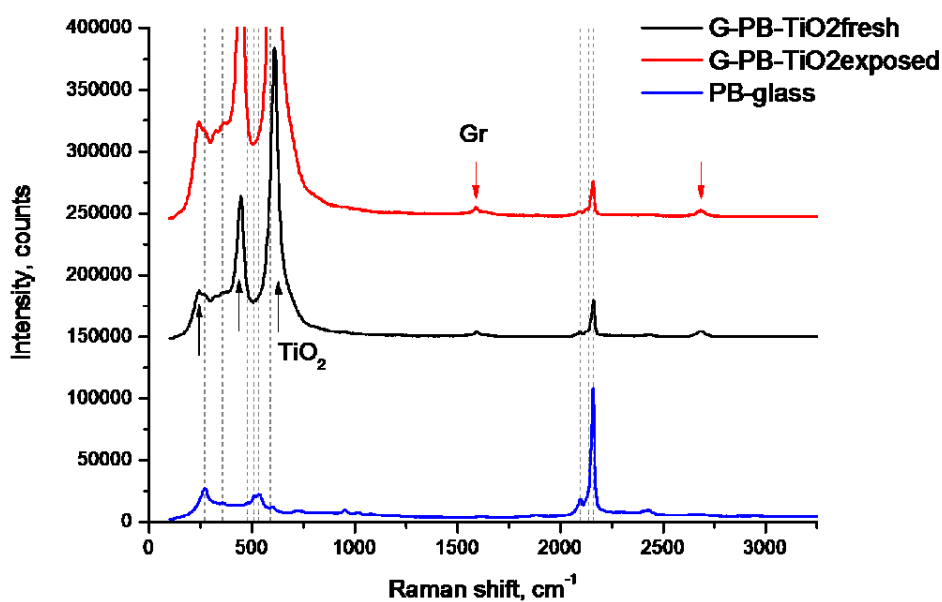


Fig. 4.16: Raman spectra of dry PB on glass (blue spectrum), fresh prepared GNBs on TiO<sub>2</sub> (black spectrum) and GNBs after 15 hours of UV exposition (red spectrum).

The dry sample shows feature very different from the GNBs. The peak at 2160 cm<sup>-1</sup> is referred to the Fe<sup>II</sup>-C≡N-Fe<sup>III</sup> A<sub>g</sub> (symmetric) stretching mode of PB [31] and is dominant for all spectra. In GNBs spectra, graphene peaks are marked by red arrows. The ratio of 2D/G intensities is about 1.5 which is typical if the signal acquired from a large area [32]. Graphene G and 2D peaks are shown in Fig. 4.17a and b, respectively. Graphene properties remain the same after UV illumination and no defects are introduced within exposure time. Fig. 4.17c shows the C≡N stretching mode of PB and depends on the iron cation valence state and coordination environment [33] and is a good indicator of iron oxidation.

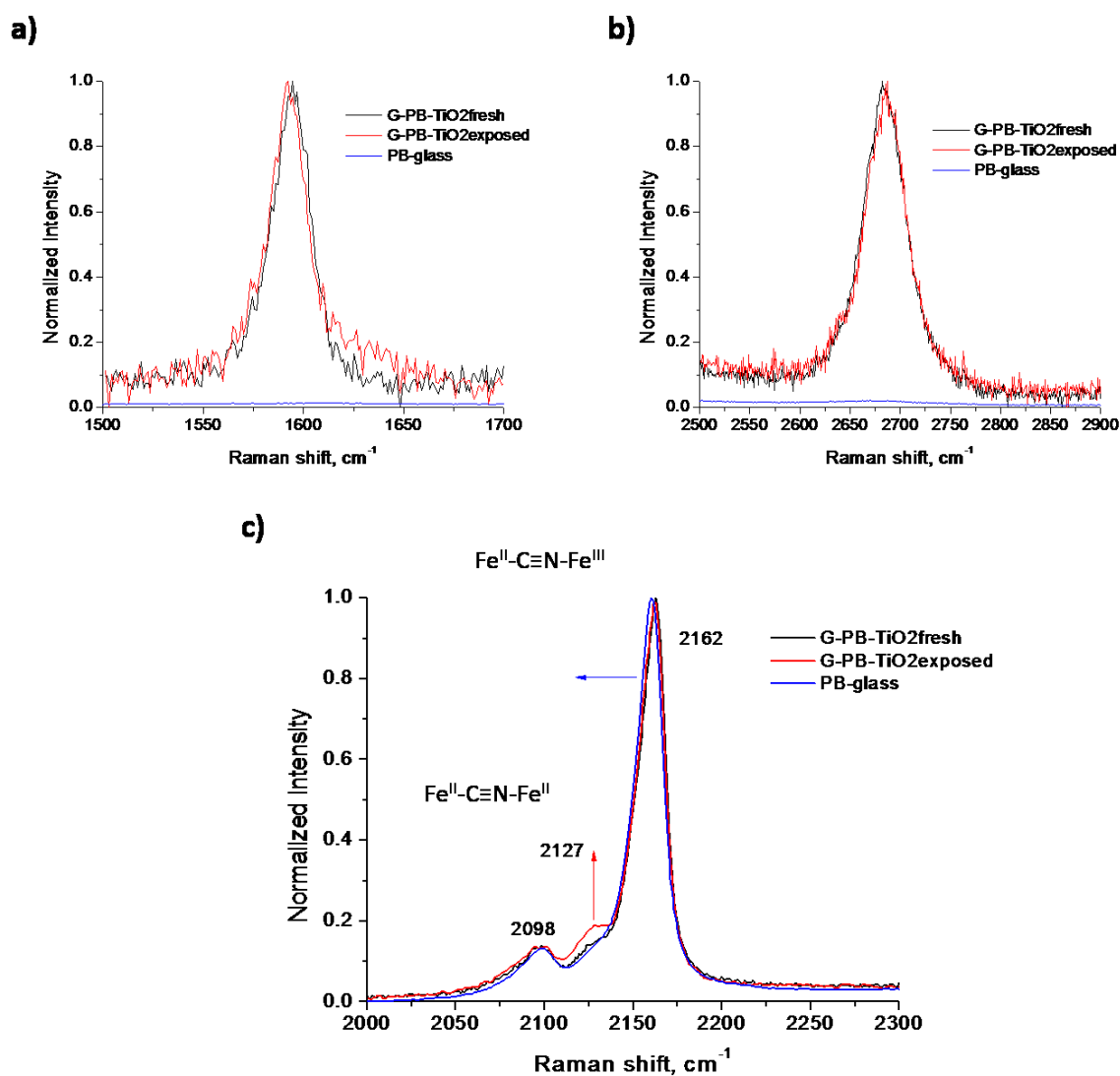


Fig. 4.17: Raman spectra of: a) graphene G peak and b) graphene 2D peak; c) C≡N stretching mode of PB.

Fig. 4.17c is referred to the  $\text{Fe}^{\text{II}}\text{-C}\equiv\text{N-Fe}^{\text{III}}$   $A_g$  stretching mode of PB [31]. The weak peak around  $2090\text{ cm}^{-1}$  is the  $E_g$  mode (asymmetric) of the  $\text{Fe}^{\text{II}}\text{-C}\equiv\text{N-Fe}^{\text{III}}$  stretching vibration [33]. On PB on glass (blue spectrum) this mode downshift by  $2\text{-}3\text{ cm}^{-1}$ . This shift can be explained by a sample drying since the  $A_g$  mode for dried PB on glass is observed at  $2160\text{ cm}^{-1}$ . It may be estimated that the presence of water or  $\text{OH}^-$  ions play an important role in the frequency shift of  $A_g$  stretching mode. The intensity of  $2090\text{ cm}^{-1}$  peak remains unchanged with UV illumination. Finally, the relative intensity of C≡N stretching mode when surrounded by  $\text{Fe}^{\text{II}}$  ( $2127\text{ cm}^{-1}$  peak) [33] grows after UV illumination (red spectrum) proving that the higher iron oxidation state of the iron cations is observed.

The reported studies confirmed that GNBs can be used to monitor *in situ* properties and dynamics of liquids for different techniques, including analysis in UHV conditions. Since we actually used the GNBs as a liquid sealed cells for *in situ* analysis without transferring the sample to a different experimental system, this configuration should be used also to follow the process also *during* the reactions, opening the way to use GNBs for *in operando* studies which can be applied at different fields such as chemistry or biology.

## References

- [1] Vasu, K.S., Prestat, E., Abraham, J., Dix, J., Kashtiban, R.J., Beheshtian, J., Sloan, J., Carbone, P., Neek-Amal, M., Haigh, S.J., Geim, A.K., Nair, R.R. *Van der Waals pressure and its effect on trapped interlayer molecules* (2016) *Nature Communications*, 7, art. no. 12168.
- [2] Neelson, K.H., Saffarini, D. *Iron and manganese in anaerobic respiration: Environmental significance, physiology, and regulation* (1994) *Annual Review of Microbiology*, 48, pp. 311-343.
- [3] Tang, C., Robson, A.D., Dilworth, M.J. *The role of iron in nodulation and nitrogen fixation in Lupinus angustifolius L* (1990) *New Phytologist*, 114 (2), pp. 173-182.
- [4] Jiang, C.-D., Gao, H.-Y., Zou, Q., Shi, L. *Effects of iron deficiency on photosynthesis and photosystem II function in soybean leaf* (2007) *Journal of Plant Physiology and Molecular Biology*, 33 (1), pp. 53-60.
- [5] Lefèvre, M., Proietti, E., Jaouen, F., Dodelet, J.-P. *Iron-Based catalysts with improved oxygen reduction activity in polymer electrolyte fuel cells* (2009) *Science*, 324 (5923), pp. 71-74.
- [6] Hudson, J.L., Tsotsis, T.T. *Electrochemical reaction dynamics: a review* (1994) *Chemical Engineering Science*, 49 (10), pp. 1493-1572.
- [7] Nijkamp, M. G. *Hydrogen Storage using Physisorption: Modified Carbon Nanofibers and Related Materials.*, Ph.D. Thesis. Universiteit Utrecht (2002).
- [8] [www.graphenea.com](http://www.graphenea.com)
- [9] Matruglio, A., Nappini, S., Naumenko, D., Magnano, E., Bondino, F., Lazzarino, M., Dal Zilio, S. *Contamination-free suspended graphene structures by a Ti-based transfer method* (2016) *Carbon*, 103, pp. 305-310.
- [10] Tissot, H., Olivieri, G., Gallet, J.-J., Bournel, F., Silly, M.G., Sirotti, F., Rochet, F. *Cation Depth-Distribution at Alkali Halide Aqueous Solution Surfaces* (2015) *Journal of Physical Chemistry C*, 119 (17), pp. 9253-9259.
- [11] Kolmakov, A., Dikin, D.A., Cote, L.J., Huang, J., Abyaneh, M.K., Amati, M., Gregoratti, L., Günther, S., Kiskinova, M. *Graphene oxide windows for in situ environmental cell photoelectron spectroscopy* (2011) *Nature Nanotechnology*, 6 (10), pp. 651-657.

- [12] Wang, L., Guo, C., Zhu, Y., Zhou, J., Fan, L., Qian, Y. *A FeCl<sub>2</sub>-graphite sandwich composite with Cl doping in graphite layers: A new anode material for high-performance Li-ion batteries* (2014) *Nanoscale*, 6 (23), pp. 14174-14179.
- [13] Zhang, X., Schiros, T., Nordlund, D., Shin, Y.C., Kong, J., Dresselhaus, M., Palacios, T. *X-Ray Spectroscopic Investigation of Chlorinated Graphene: Surface Structure and Electronic Effects* (2015) *Advanced Functional Materials*, 25 (26), pp. 4163-4169.
- [14] Lin, Y., Cai, W., Tian, X., Liu, X., Wang, G., Liang, C. *Polyacrylonitrile/ferrous chloride composite porous nanofibers and their strong Cr-removal performance* (2011) *Journal of Materials Chemistry*, 21 (4), pp. 991-997.
- [15] Grosvenor, A.P., Kobe, B.A., Biesinger, M.C., McIntyre, N.S. *Investigation of multiplet splitting of Fe 2p XPS spectra and bonding in iron compounds* (2004) *Surface and Interface Analysis*, 36 (12), pp. 1564-1574.
- [16] Stavitski, E., de Groot, F.M.F. *The CTM4XAS program for EELS and XAS spectral shape analysis of transition metal L edges* (2010) *Micron*, 41 (7), pp. 687-694.
- [17] Wasinger, E.C., De Groot, F.M.F., Hedman, B., Hodgson, K.O., Solomon, E.I. *L-edge X-ray Absorption Spectroscopy of Non-Heme Iron Sites: Experimental Determination of Differential Orbital Covalency* (2003) *Journal of the American Chemical Society*, 125 (42), pp. 12894-12906.
- [18] Atak, K., Bokarev, S.I., Gotz, M., Golnak, R., Lange, K.M., Engel, N., Dantz, M., Suljoti, E., Kühn, O., Aziz, E.F. *Nature of the chemical bond of aqueous Fe<sup>2+</sup> probed by soft X-ray spectroscopies and ab initio calculations* (2013) *Journal of Physical Chemistry B*, 117 (41), pp. 12613-12618.
- [19] Everett, J., Céspedes, E., Shelford, L.R., Exley, C., Collingwood, J.F., Dobson, J., Van Der Laan, G., Jenkins, C.A., Arenholz, E., Telling, N.D. *Ferrous iron formation following the co-aggregation of ferric iron and the Alzheimer's disease peptide  $\beta$ -amyloid (1-42)* (2014) *Journal of the Royal Society Interface*, 11 (95), art. no. 20140165.
- [20] Kanungo, S.B., Mishra, S.K. *Thermal dehydration and decomposition of FeCl<sub>3</sub>·xH<sub>2</sub>O* (1996) *Journal of Thermal Analysis*, 46 (5), pp. 1487-1500.
- [21] J. Kirby, D. Saunders. *Fading and colour change of Prussian blue: methods of manufacture and the influence of extenders* (2004) *National Gallery Technical Bulletin*. (2004) vol. 25. Editor Ashok Roy.
- [22] Yamamoto, T., Saso, N., Umemura, Y., Einaga, Y. *Photoreduction of prussian blue intercalated into titania nanosheet ultrathin films* (2009) *Journal of the American Chemical Society*, 131 (37), pp. 13196-13197.

- [23] Itaya, K., Uchida, I., Neff, V.D. *Electrochemistry of polynuclear transition metal cyanides: Prussian blue and its analogues* (1986) *Accounts of Chemical Research*®, 19 (6), pp. 162-168.
- [24] Neff, V.D. *Some Performance Characteristics of a Prussian Blue Battery* (1985) *Journal of the Electrochemical Society*, 132 (6), pp. 1382-1384.
- [25] Yamamoto, T., Saso, N., Umemura, Y., Einaga, Y. *Photoreduction of prussian blue intercalated into titania nanosheet ultrathin films* (2009) *Journal of the American Chemical Society*, 131 (37), pp. 13196-13197.
- [26] *Granqvist, C. G. Handbook of Inorganic Electrochromic Materials*, 1<sup>st</sup> edition (1995) Elsevier B.V
- [27] Duonghong, D., Ramsden, J., Grätzel, M. *Dynamics of interfacial electron-transfer processes in colloidal semiconductor systems* (1982) *Journal of the American Chemical Society*, 104 (11), pp. 2977-2985.
- [28] Jia, Y., Gong, X., Peng, P., Wang, Z., Tian, Z., Ren, L., Fu, Y., Zhang, H. *Toward High Carrier Mobility and Low Contact Resistance: Laser Cleaning of PMMA Residues on raphene Surfaces* (2016) *Nano-Micro Letters*, 8 (4), pp. 336-346.
- [29] Wang, L., Song, J., Qiao, R., Wray, L.A., Hossain, M.A., Chuang, Y.-D., Yang, W., Lu, Y., Evans, D., Lee, J.-J., Vail, S., Zhao, X., Nishijima, M., Kakimoto, S., Goodenough, J.B. *Rhombohedral Prussian white as cathode for rechargeable sodium-ion batteries* (2015) *Journal of the American Chemical Society*, 137 (7), pp. 2548-2554.
- [30] Hocking, R.K., Wasinger, E.C., De Groot, F.M.F., Hodgson, K.O., Hedman, B., Solomon, E.I. *Fe L-edge XAS studies of K<sub>4</sub>[Fe(CN)<sub>6</sub>] and K<sub>3</sub>[Fe(CN)<sub>6</sub>]: A direct probe of back-bonding* (2006) *Journal of the American Chemical Society*, 128 (32), pp. 10442-10451.
- [31] Gervais, C., Languille, M.-A., Réguer, S., Gillet, M., Pelletier, S., Garnier, C., Vicenzi, E.P., Bertrand, L. *Why does Prussian blue fade? Understanding the role(s) of the substrate* (2013) *Journal of Analytical Atomic Spectrometry*, 28 (10), pp. 1600-1609.
- [32] Mažeikien, R., Niaura, G., Malinauskas, A. *Electrocatalytic reduction of hydrogen peroxide at Prussian blue modified electrode: An in situ Raman spectroelectrochemical study* (2011) *Journal of Electroanalytical Chemistry*, 660 (1), pp. 140-146.
- [33] Samain, L., Grandjean, F., Long, G.J., Martinetto, P., Bordet, P., Strivay, D. *Relationship between the synthesis of Prussian blue pigments, their color, physical properties, and their behavior in paint layers* (2013) *Journal of Physical Chemistry C*, 117 (19), pp. 9693-9712.





# Chapter 5

## 5.1 Graphene nanostructures as neuronal interfaces

Tissue engineering is an emerging strategy to repair and regenerate tissues and organs. One of the mainstream approaches to perform tissue regenerations is based on the use of substrates which mimic the cellular microenvironment and provide physico-chemical cues to enable cell attachment, proliferation, and differentiation. In particular, in the last decades, social and cost implications of neuronal diseases are increasing and this are leading to a big interest in evaluating the possibility to restore, at least partially, the functions of central or peripheral nervous system compromised after an injury or a neuro-associated disease. In this field, a new-generation of devices must have the ability to interact actively with the newly formed tissue. In fact, the possibility to stimulate cells composing an artificial tissue or to record cells signals could open to new therapeutic approaches to treat neurological disabilities [1].

A neuronal interface with nanoscale components could represent the ideal choice to interface the complex structural features of neuronal tissue, because many elements of neurons, glial cells, and extracellular matrix (ECM) are characterized by nanoscale dimensions. Moreover, the unique intrinsic properties of nanomaterials offer a great promise for seamlessly integration of neuro-devices with neural tissue simulating the morphological features (and functions) of real cells and ECM [2]. Electrically active nanomaterials such as carbon nanotubes (CNTs) [3], silicon nanowires [4], gallium phosphide nanowires [5], and conducting polymer nanotubes [6] have been already interfaced with central and peripheral nervous systems demonstrating the feasibility of such approach and even peculiar advantages respect to conventional materials. For instance, CNT-based scaffolds have been found to promote growth, differentiation, and survival of neurons and to improve their electrophysiological properties in terms of firing frequency and degree of synchronization [7]. Recently, single layer graphene, due to its extraordinary properties such as high electrical conductivity, large surface area, flexibility, and excellent cytocompatibility, is

attracting great interest as biocompatible material for neuronal interfaces. It was shown that CVD grown graphene can act as a possible platform for neuronal growth [8] and primary hippocampal neurons from mouse can grow on bare graphene for up to 5 days, improving significantly cellular adhesion and processes outgrowth in early stages of network formation (1÷2 days in vitro – DIV) [9]. Interestingly, in the same work, neurons cultured on defective graphene sheets showed only limited neuronal attachment and growth, while highly ordered and crystalline graphene sheets allowed the development of cells. These observations suggest that high-quality graphene, characterized by high crystallinity and low lattice defectivity, plays an extremely important role in neuronal attachment, outgrowth, and axonal specification. Starting from these assumptions, graphene-based devices could open a route for the development of a new generation of flexible and high-sensitive bio-scaffold and neural prostheses [10].

In this Chapter, our preliminary results confirm that high quality graphene can be successfully used to interface neuronal cells and, more interestingly, can also control their electrical properties.

## **5.2 Growth of neuronal cells on supported and suspended graphene**

Inspired by the current results, we decide to study, for the first time in literature, the electrical activity of neuronal networks developed on single layer graphene. As well-known from literature, suspended graphene membranes are characterized by an electron mobility two order of magnitude higher than graphene transferred on a substrate ( $\sim 200000 \text{ cm}^2\text{V}^{-1}\text{s}^{-1}$  respect to  $\sim 28000 \text{ cm}^2\text{V}^{-1}\text{s}^{-1}$  for unsuspended graphene transferred on Si/SiO<sub>2</sub>) [11]. This is mainly due to the strong interaction of graphene with the underlying substrate which could lead to surface charge traps formation [12], substrate induced ripples and/or formation of interfacial phonons [13]. The electrical properties of the substrate could represent the main perturbation factor of neuronal electrical activity. For this reason, we started a collaboration with the neurobiology sector of the International School of Advanced Study (S.I.S.S.A) in Trieste, in order to study the morphological and the electrophysiological (passive and active properties) characteristics of neuronal networks on both supported and suspended graphene. At the best of our knowledges, there are no studies about the development and the

electrophysiological activity of primary neurons on graphene and, in particular, on suspended graphene membranes.

### 5.2.1 Fabrication of the substrates

In order to have a biocompatible and transparent substrate, I used OrmoComp® (micro resist technology, GmbH) which is an imprintable, non-toxic, UV-curable polymer and is transparent from near UV (350 nm) to VIS (800 nm) covering so all the spectrum of visible light.

I prepared two different kind of samples, one with a flat OrmoComp surface (to produce supported graphene), and the second with a patterned OrmoComp surface (to produce suspended graphene). I started from a silicon master which has patterned relief structures on its surface and subsequently a poly-dimethylsiloxane (PDMS) stamp is prepared with replica molding process. A PDMS mould is preferred rather than the silicon master because allows multiple copies without damaging the original and can be use in mass production.

Two masters have been prepared, one flat and one patterned with an array of grooves. In detail, to produce the silicon masters, MEGAPOSIT® SPR 220 1.2 photoresist is patterned on silicon with lines of width and periodicity of 10 µm and 20 µm, respectively. The pattern is transferred to the silicon wafer by ICP-RIE, with a deep of 10 µm using BOSCH® like process (gases: SF<sub>6</sub>, C<sub>4</sub>F<sub>8</sub>, Ar), and a final O<sub>2</sub> plasma to remove the resist mask.

15 minutes of Piranha solution treatment (H<sub>2</sub>SO<sub>4</sub>:H<sub>2</sub>O<sub>2</sub> 7:3 ratio in volume) allows the removal of carbon residuals from the surface. On both obtained silicon stamps (flat and patterned), silanization has been performed to increase the idrophobicity reducing, consequently, adhesion interaction of the PDMS. This will allow a successful peeling-off of PDMS replicas from the stamp. The PDMS stamps have been prepared with the replica molder method, as follow: silicone elastomer (SILGARD® 184) is mixed with the liquid curing agent (10:1 ratio in

#### Silanization

Cover a surface with organofunctional alkoxy silane molecules. In case of silicon, Piranha solution can be used to increase the surface density of reactive -OH groups. This can hydrolyze and form siloxane linkages (Si-O-Si) with organic silane molecules.



weight), degassed in a desiccator and finally cured at 85 °C overnight. The OrmoComp substrates have been prepared on circular glasses (5 mm of diameter, 0.12 mm thick), cleaned previously in Piranha solution (H<sub>2</sub>SO<sub>4</sub>:H<sub>2</sub>O<sub>2</sub> 5:5 ratio in volume). A drop of OrmoComp is droplet on the glass and pressed with the PDMS stamp in order to transfer the micropattern. Finally, the OrmoComp is cured with UV light and the PDMS stamp is released. A SEM image of the obtained patterned OrmoComp substrate on glass is shown in Fig. 5.1.

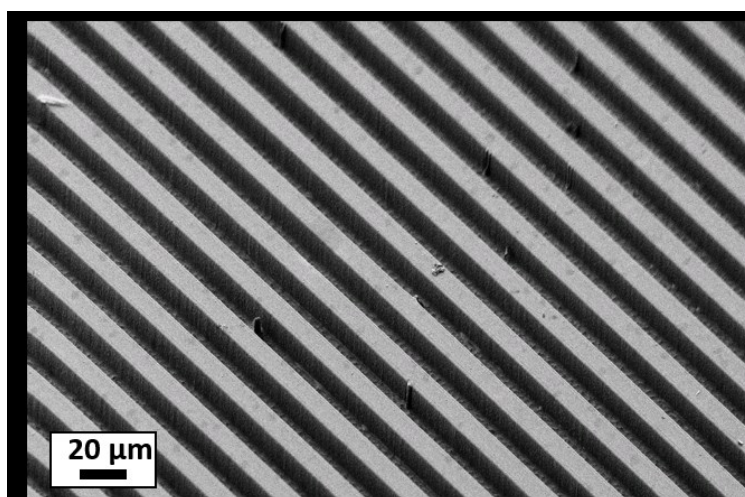


Fig. 5.1: SEM image of the OrmoComp substrate patterned with an array of lines with width and periodicity of 10 μm and 20 μm, respectively.

Commercially available CVD graphene on Cu [14] is used following the protocol previously described in Chapter 2. Briefly, a sacrificial layer 250 nm-thick of mr-I 7020 is spin coated on the graphene/Cu and the polymer/graphene/Cu membrane is placed in the Cu etching solution. After the etching process, graphene is rinsed in DI water and the transfer is performed fishing graphene into the water directly on the OrmoComp substrate. Water is left to evaporate at room temperature for 2 h, and mr-I 7020 is dissolved in cold acetone for 5 minutes. In case of suspended graphene, CPD process is performed in order to avoid the collapse of the suspended structures. A summary scheme of the process for the two sets of samples is shown in Fig. 5.2.

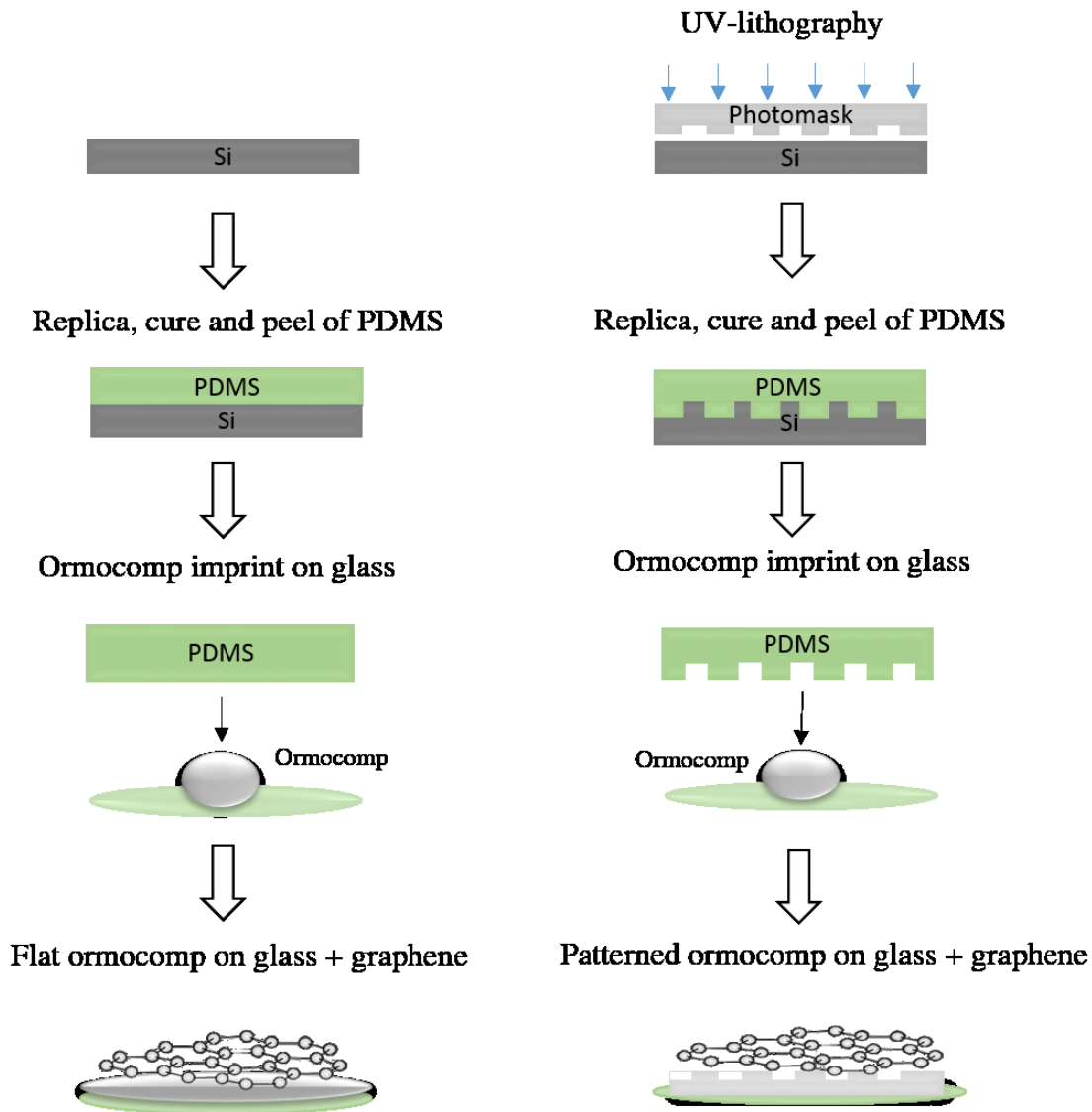


Fig. 5.2: scheme of the fabrication process used for the flat graphene samples (on the left) and the suspended graphene samples (on the right).

### 5.2.2 Neuronal cultures

Neuronal cultures and electrophysiological experiments were performed in S.I.S.S.A. NeuroNano Laboratory. Primary neuronal cells were obtained from rat hippocampi. Dissociated hippocampal cultures were prepared according to Malgaroli and Tsien method [15] with slight modification [16]. Briefly, after the decapitation of Wistar neonatal (P2/P3) rats (in accordance with regulations of the Italian Animal Welfare Act and approved by the local Authority Veterinary Service), hippocampi were isolated from the rest of the brain

and upon enzymatic treatment neurons were dissociated by pipetting. Before using for culturing, all the OrmoComp/graphene substrates were mounted on glass coverslips (12×24 mm<sup>2</sup>, 0.13÷0.16 mm thick, Kindler, EU) using a thin adhesive layer of PDMS cured at 120 °C for 1 hour. Coverslips were placed in small Petri dishes and culture in serum-containing medium in a 5% CO<sub>2</sub>-humified incubator for 9÷10 days. Finally, cells were plated on three replica of substrates for each condition: bare glass used for control (ctrl), supported graphene on flat OrmoComp and suspended graphene on patterned OrmoComp. Before cell plating all the samples were sterilised in UV for 20 minutes and covered by a thin layer of poly-L-ornithine.

### **5.2.3 Morphology of neuronal cells on different substrates: SEM characterization**

A first information of the developed neuronal networks can be obtained by SEM characterization. After glutaraldehyde fixation in cacodylate buffer, performed following the protocol described by Bosi *et al.* [17], cultures are dehydrated dipping the sample in water/ethanol solutions at progressively higher alcohol concentrations (50%, 75%, 95%, 98% and 100% ethanol for 5 minutes each at room temperature). Finally, samples are metallized via sputter-coater with Pt: Au = 5 nm:5 nm in order to make the sample conductive to electrons. Fig. 5.3 shows SEM images of the cells which were obtained on the different substrates. In particular, large-area images on the left show a portion of the resulting neuronal networks (glass controls in Fig.5.3a, supported graphene in Fig. 5.3c, and suspended graphene in Fig. 5.3e); small-area images on the right pointed out the morphology of the individual cells composing the network (glass control in Fig. 5.3b, supported graphene in Fig. 5.3d and suspended graphene in Fig. 5.3f).

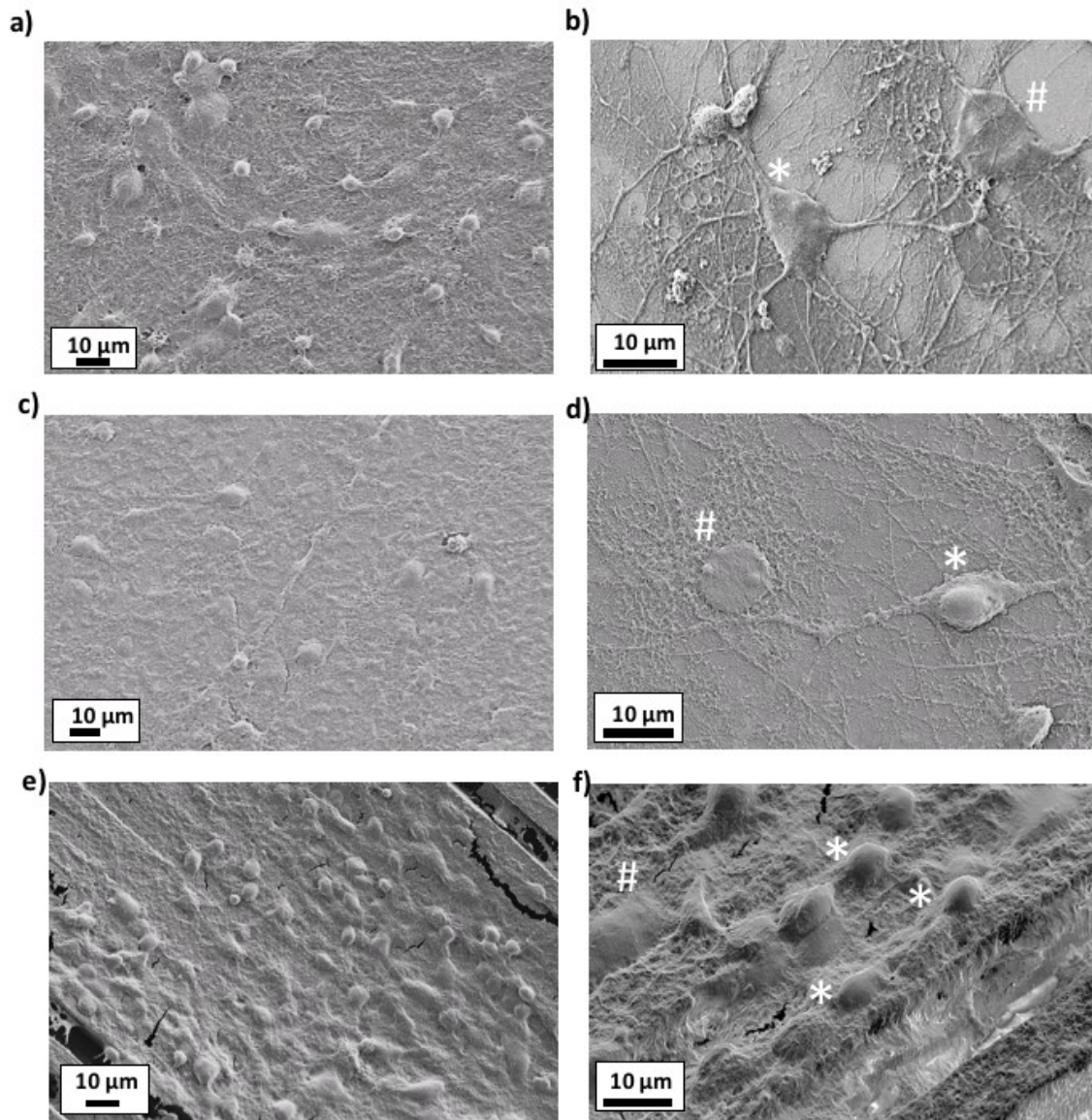


Fig. 5.3: SEM images of networks of primary neurons from rat hippocampus developed on three different substrates: control glass (a and b), supported graphene (c and d) and suspended graphene (e and f). On the left low magnification images pointing out cellular network structure; on the right high magnification images revealing the morphology of the single cells composing the network.

SEM images reveal that cells grown on glass control and on supported graphene substrates show similar network morphologies. From the high magnification images, it is possible to distinguish the protruding, globular shape of neuronal cell bodies, marked with asterisks, and the flat, circular shape, of glial cells nucleus, marked with hash marks. ECM is visible



in both samples, but in areas where its amount is limited it is possible to visualize individual cells distinguishing between their phenotype based on cell-body morphology. Cells grown on suspended graphene are more difficult to individually visualize, mainly due to the presence of a higher amount of ECM covering all the cells present on the surface. For this reason, it is not possible to univocally distinguish cells between neurons or glial cells basing only on cell body shape. Moreover, cell bodies appear smaller in size when compared with cells grown on both controls and supported graphene.

Finally, the presence of some breaks and rips on the suspended structure can be noticed (Fig. 5.3f); these breaks are absent on pristine samples (before cell culturing), and were probably produced during cell development or during subsequent fixation, dehydration and drying processes.

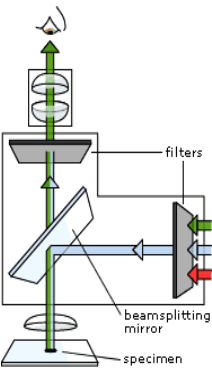
#### 5.2.4 Immunofluorescence experiments

In order to identify cells and to distinguish neuronal cells, fluorescence microscopy has been used.

**Fluorescence microscopy**

---

Uses the high specificity of antibodies to their antigen to target fluorescent dyes (fluorophores) to specific biomolecules within a cell, allowing the distribution of the target molecule in the sample. The specimen is illuminated with light of a specific wavelength which is absorbed by the fluorophores.



The radiation collides with the atoms in the specimen and electrons are excited to a higher energy level. The spectral emission of the fluorophore is matched by a filter which allows to image the distribution of a single fluorophore (color) at a time. Multi-color images of several types of fluorophores must be composed by combining several single-color images.

To proceed with immunofluorescence, dissociated hippocampal cultures were fixed using a solution of 4% paraformaldehyde in phosphate buffered saline and subsequently stained

follow the protocol described by Bosi *et al.* [17]. Upon staining, cultures were imaged using a confocal microscope (DM6000 Leica Microsystems GmbH, Wetzlar, Germany) and analysed using the open-source software Fiji (ImageJ). Samples were investigated using a 20× magnification air-working objective (NA=0.75) and serial confocal planes (z-stack) were acquired every 500 nm across the entire sample surface (n = 80 z-stacks maximum). The cultures were displayed using  $\beta$ -tubulin III positive cells (in red, pointing out neuronal cell phenotype) and glial fibrillary acidic protein (GFAP) positive ones (in green, pointing out, instead, glial cell phenotype). On all the samples cellular nuclei were visualized by DAPI (in blue). An example of such analysis is reported in Fig. 5.4 showing morphology of cells developed on a supported graphene substrate.

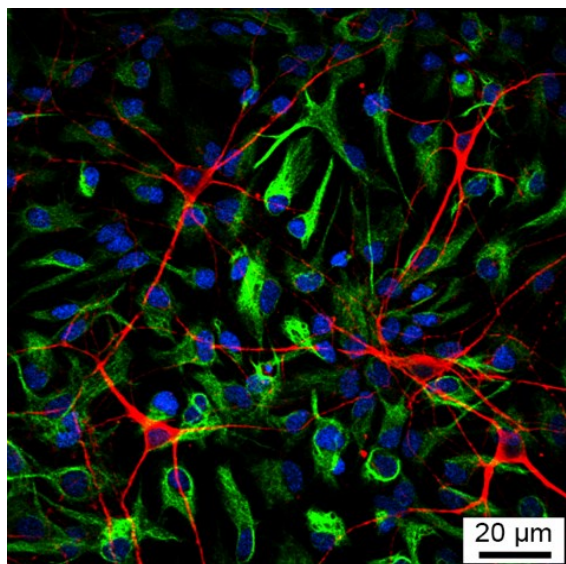


Fig. 5.4: confocal fluorescence image of dissociated cells from rat hippocampus after 9 DIV of in-vitro culturing above a supported graphene substrate. Neurons were marked in red pointing out neuronal-specific cytoskeletal protein  $\beta$ -tubulin III, while glial cells were highlighted taking advantage of the glial cell specific intermediate-filament protein glial fibrillary acidic protein (GFAP in green). Nuclei of all cells were marked using 4',6-diamidino-2-phenylindole (DAPI), a fluorescent stain that binds strongly to A-T rich regions in DNA and extensively used in fluorescence microscopy for cell counting.

The fluorescence image of Fig. 5.4 shows a continuous cells network on supported graphene, formed by neurons and glial cells, confirming the SEM image of Fig. 5.3c. As highlighted

also from SEM images of Fig. 5.4a and c, neuronal networks developed above control glass and supported graphene are characterized by comparable cellular and network morphologies. To have information also on the cells developed on suspended graphene, the 3D confocal fluorescence reconstruction has been performed and the results are shown in Fig. 5.5. Neuronal cells are indicating in red ( $\beta$ -Tubulin III), glial cells in green (GFAP), and nuclei in blue (DAPI).

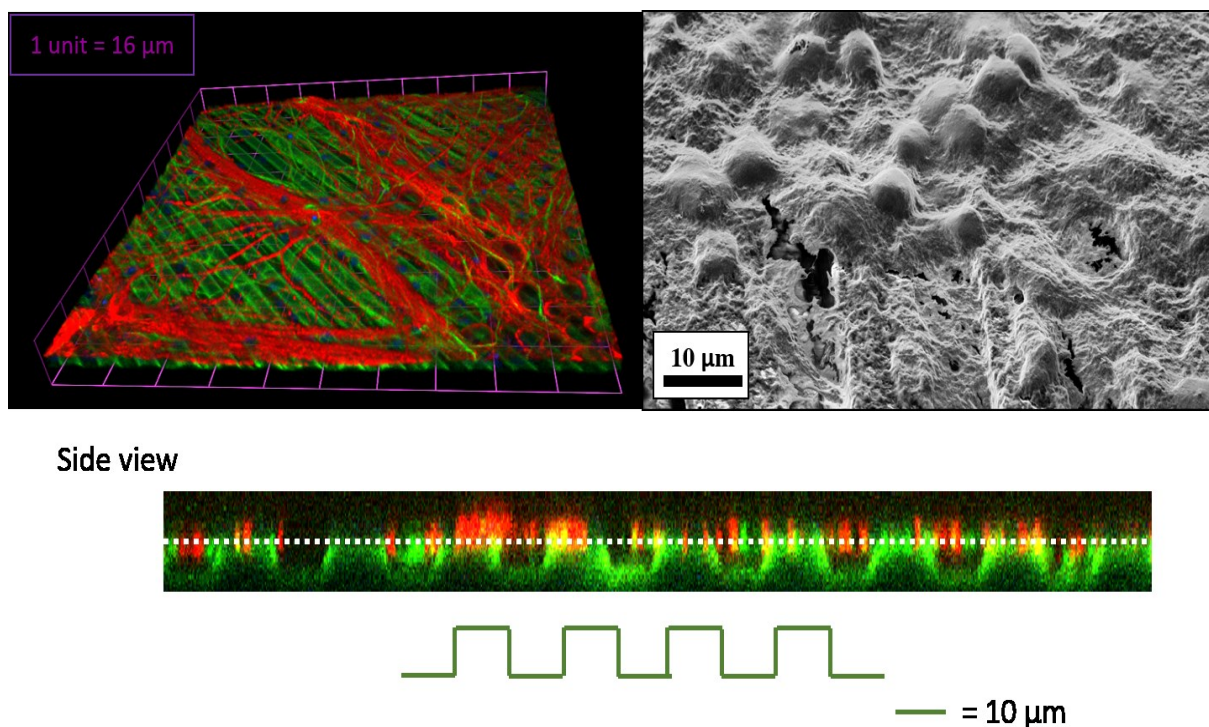


Fig. 5.5: top-left, 3D confocal fluorescence reconstruction of hippocampal cells from rat on suspended graphene. In red neuronal cells ( $\beta$ -Tubulin III), in green glial cells (GFAP), nuclei in blue (DAPI). Top-right, SEM image of cells grown on suspended graphene. Bottom, a representative cross section of the confocal reconstruction above pointing out the localization of all neuronal cells (in red) above a plane (the monoatomic layer of graphene) situated at the top of underneath OrmoComp stripes. Green signal which come from the substrate itself is imputable to OrmoComp auto-fluorescence.

As pointed out by the side-view in the lower part of Fig. 5.5, neuronal cells appear suspended above the OrmoComp stripes, probably due to the presence of the suspended layer of graphene. This supposition is validated as well by the SEM image in Fig. 5.5, right, were cells appear all coplanar, and any inter-row invagination is present. Interestingly, OrmoComp substrate exhibits a strong fluorescence in the green channel, an unintentional

property that make possible a direct confocal reconstruction of the underlying patterned substrate.

Despite the fact that cell densities on all the three substrates are comparable, neurons on suspended graphene show a preferential orientation along the underneath parallel linear grooves. This is an unexpected behavior, if we consider that the grooves are not directly accessible to the cells but rather masked by the graphene layer. This result may be due to the differential stiffness of the substrate between the regions where graphene is suspended (flexible) and the regions where graphene is supported on OrmoComp stripes (rigid).

Fig. 5.6a shows a 3D confocal fluorescence image of the border between the OrmoComp stripes and the glass control. The patterned region is the only area on which graphene is present. Cells are arranged on both the surfaces.

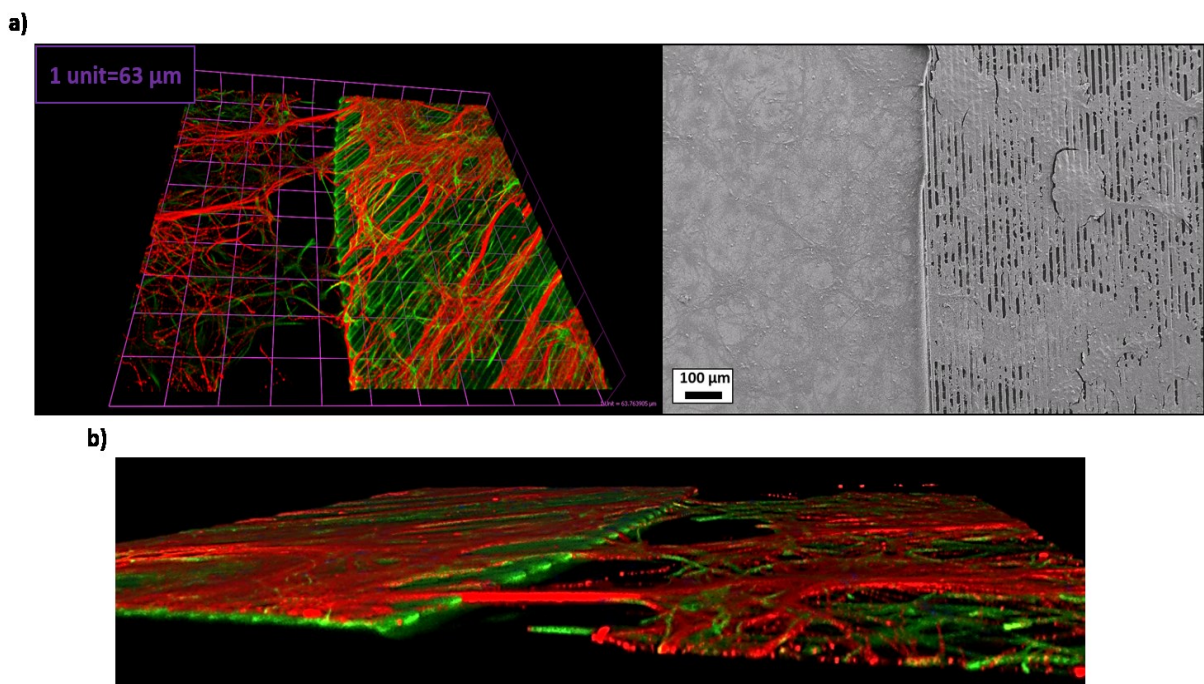


Fig. 5.6: a) left, 3D confocal fluorescence reconstruction of hippocampal cells from rat on the boundary between the flat glass area of the sample (left-part) and the patterned area with suspended graphene (right-part). In red neuronal cells ( $\beta$ -Tubulin III), in green glial cells (GFAP), nuclei in blue (DAPI). Right, SEM image of cells grown on a similar region of the sample. b) a 3D perspective representation of the confocal image which shows again that the resulting neuronal network extends from the graphene (on the patterned substrate) region to the flat region so forming a continuous. Green signal coming from the pattern itself is imputable to OrmoComp auto-fluorescence.

Fig. 5.6 shows a cellular network which continue from the OrmoComp patterned region to the flat glass surface; this aspect is visible in the confocal 3D reconstruction (Fig. 5.6a left), which shows both neurons and glial cells, and in the SEM image (Fig. 5.6a right), showing presence of cells on both sides of sample. The aligned network of neuronal cells on the suspended graphene region gradually transforms in a more spread morphology on the flat glass surface, as shown also by the 3D prospective in Fig. 5.6b, confirming the results observed in Fig. 5.5.

### 5.2.5 Electrophysiology

For all electrophysiological characterization the patch clamp technique has been used [18]. Electrophysiological experiments were performed using protocols describe by Lovat *et al.* [16]. The cellular electrical activity is obtained recording the ionic currents flowing through ionic channels at the plasma membrane of the excitable cell. Briefly, a patch of neuronal cell membrane is isolated by a sealed glass capillary with a diameter tip of about 1  $\mu\text{m}$ . A gentle suction is applied, in order to remove the membrane interposed between cell cytosol and the inner solution of the pipette. Consequently, a tight junction is originated between the two electrolytic environments. A silver/silver-chloride reversible electrode is placed into the capillary in order to have the electrode in contact with the inner environment of the cell through the “giga-ohm” pipette-membrane junction; in this way it is possible to record the cellular electrical activity. The measurements are performed holding the membrane potential to the desired value (voltage clamp-mode) [19]. Patch-clamp recordings were analysed subsequently by the AxographX and Clampfit 10.4 (Molecular Devices) software.

The experiments are focused mainly on the evaluation of cells passive properties (resistance and capacitance) and network electrical activity (spontaneous post-synaptic currents amplitude and frequency). Cell resistance and capacitance give an indication of the health state of cell’s membrane and an estimation of cell dimension, respectively. Spontaneous post-synaptic currents (sPSC) amplitude may be correlated to a higher efficiency of post-synaptic neurons to be polarised by the pre-synaptic neuron or to a higher level of synchronisation in network activity. Instead, sPSC frequency could be directly correlated, in first approximation, to the number of synapses present in the network.

. The results of electrophysiological characterisations done on neuronal cultures grown on glass controls (CTRL), on supported graphene (FLAT) and on suspended graphene (SUSP) are shown in Fig. 5.7.

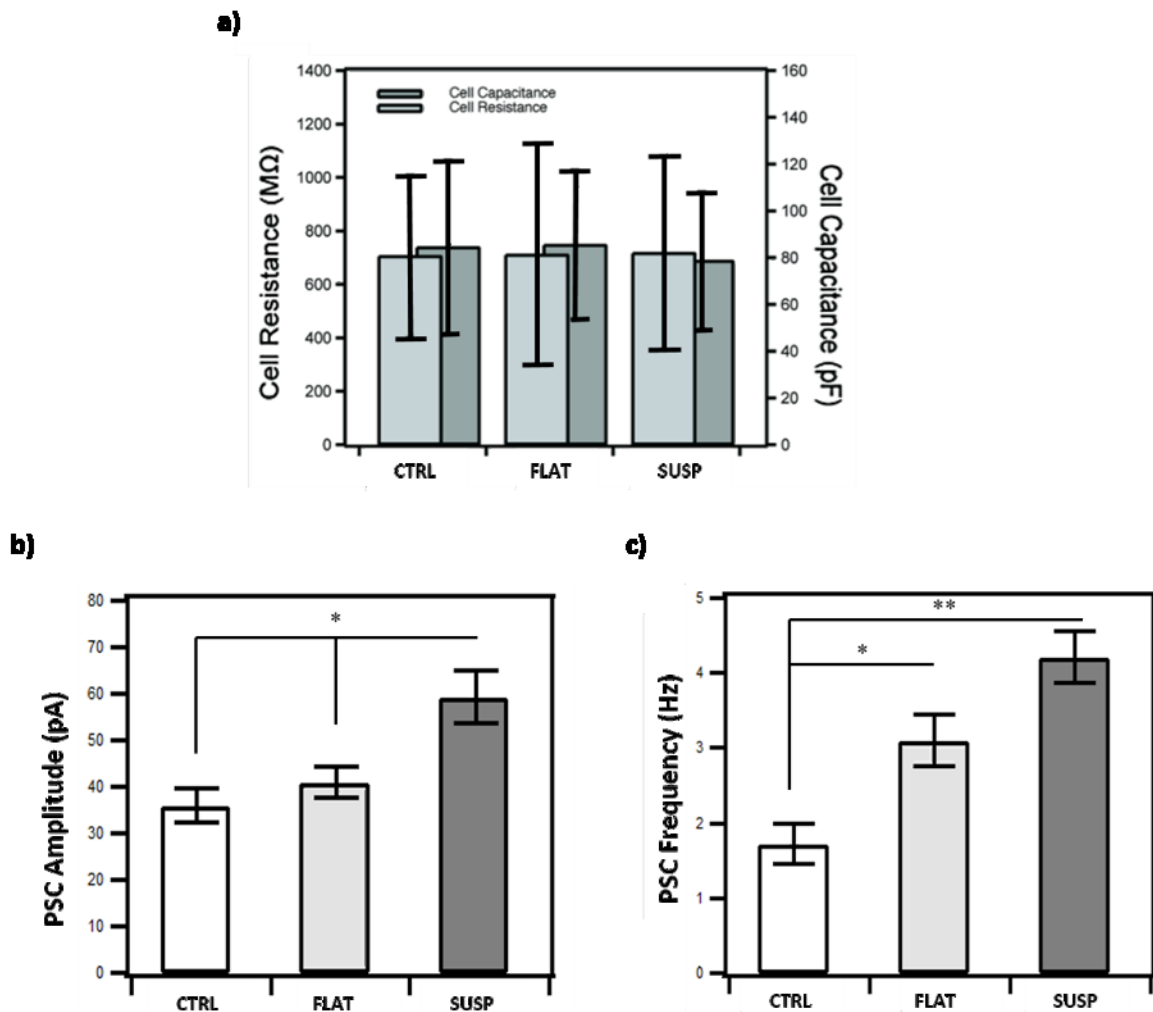


Fig. 5.7: electrophysiological characterization of neuronal networks; a) neuronal cells passive properties (cell capacitance in dark gray, and cell resistance in light gray) for neuronal networks developed on control glass substrates (CTRL), on supported graphene (FLAT) and on suspended graphene (SUSP); b) spontaneous post synaptic currents amplitudes; c) frequencies for neuronal networks developed on the same three substrates.

All data represented as normal distributions (mean±SD).

The passive properties for neurons on all the three substrates (Fig. 5.7a) show a cell resistance of  $707 \pm 304$  MΩ,  $712 \pm 414$  MΩ and  $718 \pm 362$  MΩ for CTRL, FLAT and SUSP respectively, and a cell capacitance:  $85 \pm 27$  pF,  $86 \pm 32$  pF and  $79 \pm 29$  pF, for CTRL, FLAT and SUSP, respectively. These results are very close to each other, indicating that neurons

on graphene substrates are characterised by healthy membranes as on controls and, from the other hand, that neurons have similar dimensions on all the three substrates.

The analysis of spontaneous post-synaptic currents amplitudes (Fig. 5.7b) points out similar values for neurons grown on control glass and on supported graphene ( $35.9 \pm 3.5$  pA and  $41.1 \pm 3.4$  pA, respectively), while cells developed on suspended graphene show slightly higher values ( $59.2 \pm 5.8$  pA). Regarding, instead, spontaneous post-synaptic currents frequencies (Fig. 5.7c), a rising trend is evident in the values characterising glass controls, supported graphene and suspended graphene ( $1.72 \pm 0.26$  Hz,  $3.11 \pm 0.35$  Hz, and  $4.22 \pm 0.35$  Hz, respectively). These last results suggested that graphene itself is able to boost synaptic activity of neuronal networks developed above it but, more interestingly, suspended graphene seems more prone to accentuate this effect.

The morphological studies based on electro-microscopy and cell passive properties determined by electrophysiological analysis indicate that graphene substrates are usable in the development of healthy and functional networks, in a way comparable to glass controls. This is a good indication of the fact that graphene can provide a direct interface to living cells and tissues. Moreover, the functional studies performed via patch-clamping technique, indicate that graphene can increase the electrical activity of cells. This result appears particularly pronounced for suspended graphene respect to supported graphene. This first results suggest that suspended graphene could be used for the design of nano-bio hybrid systems able to govern cell-specific behaviors in cultured neuronal networks. This would pave the way to the development of a new generation of neuronal interfaces able to interact, actively, with real nerves or brain tissue for nano-bio-medical applications.

## References

- [1] Hatsopoulos, N.G., Donoghue, J.P. *The science of neural interface systems* (2009) Annual Review of Neuroscience, 32, pp. 249-266.
- [2] Silva, G.A. Neuroscience nanotechnology: Progress, opportunities and challenges (2006) Nature Reviews Neuroscience, 7 (1), pp. 65-74.
- [3] Keefer, E.W., Botterman, B.R., Romero, M.I., Rossi, A.F., Gross, G.W. *Carbon nanotube coating improves neuronal recordings* (2008) Nature Nanotechnology, 3 (7), pp. 434-439.
- [4] Patolsky, F., Timko, B.P., Yu, G., Fang, Y., Greytak, A.B., Zheng, G., Lieber, C.M. *Detection, stimulation, and inhibition of neuronal signals with high-density nanowire transistor arrays* (2006) Science, 313 (5790), pp. 1100-1104.
- [5] Suyatin, D.B., Wallman, L., Thelin, J., Prinz, C.N., Jörntell, H., Samuelson, L., Montelius, L., Schouenborg, J. *Nanowire-Based Electrode for Acute In Vivo Neural Recordings in the Brain* (2013) PLoS ONE, 8 (2), art. no. e56673.
- [6] Abidian, M.R., Martin, D.C. *Experimental and theoretical characterization of implantable neural microelectrodes modified with conducting polymer nanotubes* (2008) Biomaterials, 29 (9), pp. 1273-1283.
- [7] Cellot, G., Cilia, E., Cipollone, S., Rancic, V., Sucapane, A., Giordani, S., Gambazzi, L., Markram, H., Grandolfo, M., Scaini, D., Gelain, F., Casalis, L., Prato, M., Giugliano, M., Ballerini, L. *Carbon nanotubes might improve neuronal performance by favouring electrical shortcuts* (2009) Nature Nanotechnology, 4 (2), pp. 126-133.
- [8] Bendali, A., Hess, L.H., Seifert, M., Forster, V., Stephan, A.-F., Garrido, J.A., Picaud, S. *Purified Neurons can Survive on Peptide-Free Graphene Layers* (2013) Advanced Healthcare Materials, 2 (7), pp. 929-933.
- [9] Li, N., Zhang, X., Song, Q., Su, R., Zhang, Q., Kong, T., Liu, L., Jin, G., Tang, M., Cheng, G. *The promotion of neurite sprouting and outgrowth of mouse hippocampal cells in culture by graphene substrates* (2011) Biomaterials, 32 (35), pp. 9374-9382.
- [10] Sahni, D., Jea, A., Mata, J.A., Marcano, D.C., Sivaganesan, A., Berlin, J.M., Tatsui, C.E., Sun, Z., Luerssen, T.G., Meng, S., Kent, T.A., Tour, J.M. *Biocompatibility of pristine graphene for neuronal interface: Laboratory investigation* (2013) Journal of Neurosurgery: Pediatrics, 11 (5), pp. 575-583.



- [11] Bolotin, K.I., Sikes, K.J., Jiang, Z., Klima, M., Fudenberg, G., Hone, J., Kim, P., Stormer, H.L. *Ultrahigh electron mobility in suspended graphene* (2008) *Solid State Communications*, 146 (9-10), pp. 351-355.
- [12] Hwang, E.H., Adam, S., Sarma, S.D. *Carrier transport in two-dimensional graphene layers* (2007) *Physical Review Letters*, 98 (18), art. no. 186806.
- [13] Ishigami, M., Chen, J.H., Cullen, W.G., Fuhrer, M.S., Williams, E.D. *Atomic structure of graphene on SiO<sub>2</sub>* (2007) *Nano Letters*, 7 (6), pp. 1643-1648.
- [14] [www.graphenea.com](http://www.graphenea.com)
- [15] Malgaroli, A., Tsien, R.W. *Glutamate-induced long-term potentiation of the frequency of miniature synaptic currents in cultured hippocampal neurons* (1992) *Nature*, 357 (6374), pp. 134-139.
- [16] Lovat, V., Pantarotto, D., Lagostena, L., Cacciari, B., Grandolfo, M., Righi, M., Spalluto, G., Prato, M., Ballerini, L. *Carbon nanotube substrates boost neuronal electrical signaling* (2005) *Nano Letters*, 5 (6), pp. 1107-1110.
- [17] Bosi, S., Rauti, R., Laishram, J., Turco, A., Lonardoni, D., Nieuws, T., Prato, M., Scaini, D., Ballerini, L. *From 2D to 3D: Novel nanostructured scaffolds to investigate signalling in reconstructed neuronal networks* (2015) *Scientific Reports*, 5, art. no. 9562.
- [18] Neher, E., Sakmann, B. *Single-channel currents recorded from membrane of denervated frog muscle fibres* (1976) *Nature*, 260 (5554), pp. 799-802.
- [19] Cole K.S., Moore J.W. *Ionic current measurements in the squid giant axon membrane* (1960). *Journal of General Physiology*, 44. 123-67.



# Conclusions and Outlook

In this thesis, I exploited several single layer graphene transfer protocols that I developed for applications in different research area, in particular chemistry and neurobiology. A brief description of graphene properties, which are at the base of its use, was presented in the first part of the thesis. The most used synthesis methods are described, followed by the existent transfer methods which are reported in literature. Graphene grown by CVD is largely used and its transfer from the metallic growth substrates to the final device surface is still an open issue, in spite of its wide application. In fact, the residual associate to PMMA removal, which is the most common polymer used to support graphene during the transfer, are very hard to eliminate, despite the adopted thermal treatments which are necessary at the end of the procedure. For this reason, in the first stage of my experimental activity, I addressed in particular graphene cleanliness, and I developed a novel transfer method which does not involve the use of any polymer. Instead of PMMA, a thin layer of titanium is used as graphene support, then removed in HF solution after graphene transfer. This method was compared with the transfer obtained using a thin layer of mr-I 7020, which is a common polymer used for nanoimprint lithography. I observed that mr-I 7020 is easier to remove respect to PMMA and I decided to compare the best polymer performance with the novel method. The results are showed in the Chapter 2 and demonstrate that the titanium transfer is a cleaner approach respect to the polymer one. XPS and Raman spectroscopy showed a cleaner graphene, with less contaminants and that preserve its high-quality after the transfer. XAS measurements showed a very low quantity of titanium after its removal ( $2.3 \times 10^{12}$  atoms/cm<sup>2</sup>), confirming the success of the new transfer method.

In the Chapter 3, the study was focused on transferred graphene applications. Because graphene is transparent to electrons, it can be used as membrane for electron microscopy or x-rays analysis. In the last years, the researchers' attention is moving to the use of graphene as transparent membrane for liquid studies. This goal was achieved with the use of graphene oxide and multilayer graphene, but there were very few works which showed the use of single-layer graphene. Graphene monolayer is prone to break and is very difficult to realize membranes or cells avoiding defects or breaks. The Chapter 3 presented graphene

nanobubbles (GNBs) filled with water fabricated on a TiO<sub>2</sub> substrate; the liquid is trapped between the graphene single-layer and the substrate and the presence of the liquid is demonstrated by XPS, XAS, AFM and Raman spectroscopy. These measurements demonstrated that the GNBs can be used as sealed cells for liquid investigation and that can be applied at different techniques. A thermal annealing allowed us to study the behavior of the GNBs, which collapse followed by a stronger graphene substrate interaction.

Thanks to the interesting results obtained with the use of GNBs in water, we used the GNB as a tool to investigate a chemical reaction *in situ* using electron spectroscopy which usually require ultra-high vacuum condition and thus cannot be used to follow water-based reactions. These results are described in the Chapter 4. First, the reduction of iron in a FeCl<sub>3</sub> solution, which was expected to be promoted by the temperature, was analyzed with XAS and Raman measurements. Secondly, the reduction of iron in Prussian Blue is obtained with UV irradiation and analyzed with both XAS and Raman techniques. GNBs allow to follow the dynamic of both the reaction *in situ*, demonstrating for the first time the use of GNBs as sealed cells for the investigation of chemical dynamic processes in ultra-high vacuum conditions.

The Chapter 5 touches a different yet equally actual field, i.e. the use of graphene for the growth of neuronal cells. The growth of rat hippocampal cells is not taken for granted, because primary cells need a biocompatible and clean material on which grow. For the first time, we analyzed not only the compatibility of single layer graphene with such cells and cells morphology (already demonstrated in literature), but also the study of electrical neuronal activity on both supported and suspended graphene, which is something absolutely new. And interestingly, we observed that the synaptic activity of neuronal networks seems to increase in case of suspended graphene.

The thesis ends with an appendix which reports on a secondary activity that I carried out during these years. This activity shares with my main thesis project the lithographic techniques and the work in cleanroom environments. Thanks to my expertises I was asked to help in the developments of those activities, and since I found them either stimulating and successful I dedicated part of my efforts in that direction. It consisted in the fabrications of two detectors for the free-electron laser (FEL) beam; one is obtained fabricating holes in bulk silicon filled with phosphors. This configuration allowed the estimation of the real focused beam shape and size just observing and counting the number of illuminated pixels after the FEL irradiation. The second one uses the previous pixelated configuration integrated with a material which can change its optical properties when hit from the FEL beam. In this

way, monitoring this properties changes, it is possible to determine the spatial and temporal overlapping of FEL and a second beam in pump and probe experiments in just few seconds, which is very impressive, especially if compared to hours or days needed with the actual procedures.

Is my opinion that the results presented in this thesis represent an encouraging starting point. GNBs can be fabricated on different materials controlling substrates hydrophilicity, in order to have a precise control on the number and size of the bubbles. Bigger bubbles and smaller incident beams could allow the real analysis of a phenomenon and not an average of GNBs in a large area. Moreover, the GNBs could be used for the study not only chemical reactions but also different phenomenon, such as physical processes in liquid phase or at the solid/liquid interface.

On the other hand, what I obtained with neuronal growth could be the door for a new generation of neuronal interfaces. The results have to be confirmed by further experiments that we have already in program, but if the statistic will confirm the obtained, positive trend we really can develop a new class of brain-tissue interfaces. The next step will be to identify which parameters effectively increase the neuronal activity and this could be performed with a characterization of the substrate and with a mechanical and electrical characterization of the suspended graphene.



# Appendix

This appendix presents two works carried out in the design and microfabrication of detectors for x-ray free electron laser (FEL) beams. The works derives from a collaboration with FERMI at Elettra which I had the possibility to carry on during all my PhD period. From this collaboration, two works which involve the characterization of the FEL beam were published so far.

In our laboratory at IOM-CNR, I designed and fabricated two detectors which were both tested on the EIS-TIMEX beamline at Fermi. The first is characterized by an array of micrometric holes filled with phosphors fabricated in a bulk silicon substrate. We called it pixelated phosphor detector (PPD). When the beam hit the detector, the cross-talk of the light between separated pixels is minimized and it is possible to estimate the real size and shape of the focused FEL beam just observing the number of illuminated pixels. The geometry of the array (diameter and period of the holes) was studied to obtain the maximum resolution possible achievable on the beamline.

The second detector is an evolution of the first one. In pump and probe experiments, the temporal alignment of pump and probe beams is a fundamental requirement to perform measurements and usually requires very long times (hours or days). An evolution of the PPD was developed introducing in some areas a material (i.e.  $\text{Al}_2\text{O}_3$ ) which can change its optical properties when hit from the FEL beam. In this way, in few seconds the temporal overlaps of the two lasers can be detected and, in the same time, the characterization given by the PPD can be obtained. This new detector allows the spatiotemporal overlapping with only one detector in few seconds. We called it PPD 2.0.

In next sections, the published papers will be presented.

## **A novel approach in the free-electron laser diagnosis based on a pixelated phosphor detector**

Alessia Matruggio,<sup>a,b</sup> Simone Dal Zilio,<sup>a\*</sup> Rudi Sergo,<sup>c</sup> Riccardo Mincigrucci,<sup>d,e</sup> Cristian Svetina,<sup>b,f</sup> Emiliano Principi,<sup>d</sup> Nicola Mahne,<sup>f</sup> Lorenzo Raimondi,<sup>f</sup> Alessio Turchet,<sup>g</sup> Claudio Masciovecchio,<sup>d</sup> Marco Lazzarino,<sup>a</sup> Giuseppe Cautero<sup>c</sup> and Marco Zangrando<sup>a,f</sup>

<sup>a</sup>IOM Laboratorio Nazionale TASC, CNR, AREA Science Park Basovizza, SS 14, Km 163.5, Trieste 34149, Italy, <sup>b</sup>Graduate School in Nanotechnology, University of Trieste, Piazzale Europa 1, Trieste 34127, Italy, <sup>c</sup>Detector and Instrumentation Laboratory, Elettra Sincrotrone Trieste, AREA Science Park Basovizza, SS 14, Km 163.5, Trieste 34149, Italy, <sup>d</sup>Beamlines Spectroscopy/Scattering, Elettra Sincrotrone Trieste, Area Science Park Basovizza, SS 14, Km 163.5, Trieste 34149, Italy, <sup>e</sup>Dipartimento di Fisica e Geologia, Università degli Studi di Perugia, Via Alessandro Pascoli, Perugia 06123, Italy, <sup>f</sup>Mechanical, Vacuum and Optical Engineering, Elettra Sincrotrone Trieste, Area Science Park Basovizza, SS 14, Km 163.5, Trieste 34149, Italy, and <sup>g</sup>Beamlines Microscopy/Diffraction, Elettra Sincrotrone Trieste, Area Science Park Basovizza, SS 14, Km 163.5, Trieste 34149, Italy. \*corresponding author.

A new high-performance method for the free-electron laser (FEL) focused beam diagnosis has been successfully tested at the FERMI FEL in Trieste, Italy. The novel pixelated phosphor detector (PPD) consists of micrometric pixels produced by classical UV lithography and dry etching technique, fabricated on a silicon substrate, arranged in a hexagonal geometry and filled with suitable phosphors. It has been demonstrated that the overall resolution of the system has increased by reducing the diffusion of the light in the phosphors. Various types of PPD have been produced and tested, demonstrating a high resolution in the beam profile and the ability to measure the actual spot size shot-to-shot with an unprecedented resolution. For these reasons, the proposed detector could become a reference technique in the FEL diagnosis field.

### 1. Introduction

An essential prerequisite for experimental research using state-of-the-art free-electron laser (FEL) light sources is the proper characterization of the beam quality. Actually, the proper diagnosis in the field of pulsed high-power vacuum ultraviolet (VUV) and soft X-ray (SXR) sources is still an open issue. Up to now, several methods for determining

transverse and longitudinal coherence (Allaria et al., 2012), spectra (Ayvazyan et al., 2002) and wavefront properties (Flöter et al., 2010) have been reported. However, only a few methods have been satisfactorily employed for the spatial profile of the beam characterization, such as: direct imaging at focus, employing YAG scintillators or phosphors screens (Tiedtke et al., 2009), ablative imprint over PMMA or silicon (Chalupský et al.,



2007), or wavefront reconstruction by means of a wavefront sensor in the far field (Mimura et al., 2010). Each technique presents undeniable features for specific investigation. However, all of the techniques are also limited in other aspects (Chalupský et al., 2011): indentation provides the real spot size but is an ex situ technique and its analysis is very time consuming, even though some preliminary results show that this method could be extended in situ (Gerasimova et al., 2013); in contrast, the wavefront sensor provides real-time measurements but it works in a limited wavelength range and is an expensive technique; the application of screen scintillators allows real time in situ imaging of the focused beam spot, making it one of the most diffused techniques; unfortunately they are easily saturated and the collected signal is degraded by the light spreading phenomenon of emitted light, affecting the beam-shape analysis due to distortion of the collected image.

In the SXR and VUV fields, indirect digital imaging is needed and it is commonly obtained by coupling a scintillator film with a two-dimensional imaging sensor (CCD or CMOS devices). The problem in resolution and contrast derived from light spreading induced the implementation of a large variety of different strategies for performance enhancement: the logical improvement is the confinement of phosphors in individual neighbouring pixels reducing the optical cross-talk. For commercial screens, increased performance has been achieved by columnar or needle-like growth structures of CsI:Tl through thermal evaporation; however, their use in high-resolution imaging is limited for the not perfect guiding and confinement of light, resulting in 'cross-talk' between pixels (Nagarkar et al., 1998).

In our pixelated phosphor detector (PPD) devices, an array of micrometric phosphor pixels has been obtained by filling micrometric silicon pores arranged in a

hexagonal geometry with suitable phosphor powders. Absorption studies on silicon (Green & Keevers, 1995) confirm that, in the visible range, light diffusion is limited in the micrometre range; for this reason, bulk silicon seems an excellent material for our purpose. A similar approach has already been proposed in the literature: Svenonius et al. (2009) fabricated a structured scintillator filled by melting thallium-doped caesium iodide into a silicon pore array; the scintillator has been directly coupled to a CMOS detector allowing improved spatial resolution by exploiting the guiding effect of the SiO<sub>2</sub>/Si pore walls. Cha et al. (2011) employed evaporated CsI:Tl or Gd<sub>2</sub>O<sub>3</sub>:Eu deposited by a screen printing technique and obtained a similar pixelated screen. Coupling the device to a lens-coupled CCD imaging device, they demonstrated the effectiveness of the microstructured scintillators for high spatial resolution and improved contrast imaging.

Starting from similar concepts, we implemented a suitable pixelated phosphors technology for application in VUV and SXR FEL focused beam diagnosis. The proposed detector has been developed by a collaboration of IOM-CNR and FERMI@Elettra in the Italian Sincrotrone. The aim of the proposed PPD is to preserve the advantages of the scintillators (such as in situ and real-time detection), increasing their spatial resolution to achieve a reference technique for spatial quality diagnosis. In our setup, the direct coupling of the phosphors screen with the CCD camera was not possible due to the limits imposed by the geometries of the experimental vacuum chamber. Moreover, due to the high energy involved, the FEL beam is able to damage instantly every exposed material. For these reasons, uncoupled devices have been preferred: the beam imaging was achieved through a tele-microscope coupled with a CCD camera installed in the exterior of the vacuum chamber. Another aspect we considered for the

design of our PPD is related to the requirement of higher resolution, closer to the beam size, of the order of a few micrometers; by reducing the pixels size in the range of a few micrometers or lower, the focused beam can be traced through the simple detection of the illuminated pixel phosphors in each cavity. At the moment, the focused beam size can then be determined by simply considering the pitch of the array and the lateral dimension of the cavity from where the light is emitted, which also defines the limit in the resolution of the system. The final result is a high-performance detector, able to measure the shot-to-shot actual spot size with unprecedented resolution for a classical phosphor screen. An interesting improvement of the PPD detector has been accomplished by coating the surface of the device with a thin film of indium tin oxide (ITO) and the first results obtained are presented in this article. Moreover, thanks to the simple design and fabrication process, the system can be easily modified and improved following the requirement of the FEL users.

## 2. Materials and methods

### 2.1. PPD fabrication processes

An array of micrometric holes arranged in a honeycomb geometry is fabricated in a clean silicon bulk substrate (500  $\mu\text{m}$  thick) using a classical optical UV lithography technique. MEGAPOSIT1 SPR 220 1.2 (SHIPLEY) photoresist has been patterned with holes with a diameter of 4  $\mu\text{m}$  and a distance between the pixels of 6  $\mu\text{m}$ , with a total fill factor of active area of 70%. A scheme of the array with its dimensions is shown in Fig. 1. The single device is 12 mm 12 mm and the patterned area is 10 mm 10 mm.

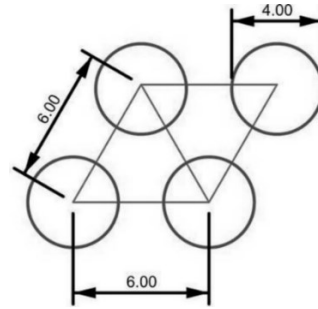


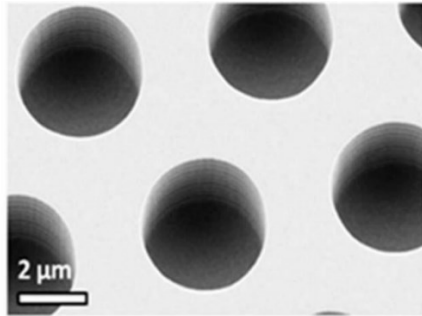
Fig. 1: Scheme of the proposed array of micrometric holes arranged in a honeycomb geometry. The lengths are given in  $\mu\text{m}$ .

Dry etching in inductively coupled plasma-reactive ion etching has been performed exploiting the resist as the mask in order to transfer the pattern in the bulk silicon; an inductively coupled plasma Bosch-like process (Chang et al., 2005) (gases:  $\text{SF}_6$ ,  $\text{C}_4\text{H}_8$ , Ar) has been set in order to obtain a depth of 5  $\mu\text{m}$ , followed by  $\text{O}_2$  plasma so as to remove the resist mask. A scanning electron microscopy (SEM) image of the array of holes is shown in Fig. 2(a). The deposition of four different types of commercially available phosphors (Phosphor Technology Company) has been achieved; the list of the powders and their corresponding characteristics are shown in Table 1. The process of deposition of the phosphor powders has been accomplished by mechanical filling of the holes using a custom-developed piezoelectric vibrating plate; the vibration induces the alignment of the phosphor grains and helps the powder enter the micrometric holes. The dry technique allows the uniform and complete filling of the pores and avoids the trapping of air bubbles in the presence of solvent due to the surface tension of the liquid. A Teflon tip can be used during the process in order to help with the filling of the cavities. The excess of phosphor, in particular the grains with size larger than the pore size, is removed from the surface by the doctor blade technique (Yen et al., 2007) using a thick (1 mm) Teflon foil. As shown in Fig. 2(b), no significant damage

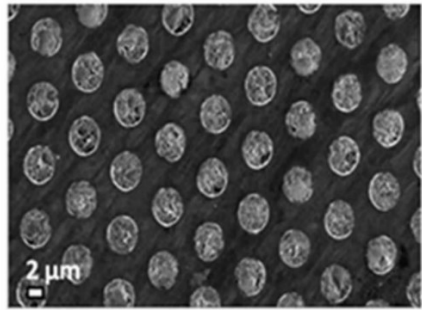
has been observed on the silicon substrate after the followed protocol.

Type	Composition	Maximum Light Emission at:	Colour	Average grain size of powder	
				Min	Max
P20	(Zn,Cd)S:Ag	560 nm	Yellow, green	1.2 $\mu\text{m}$	6 $\mu\text{m}$
P43	Gd <sub>2</sub> O <sub>2</sub> S	560 nm	Green	1.2 $\mu\text{m}$	6 $\mu\text{m}$
P46	Y <sub>3</sub> Al <sub>5</sub> O <sub>12</sub> :Ce	544 nm	Blue, white	1.2 $\mu\text{m}$	6 $\mu\text{m}$
P47	Y <sub>3</sub> SiO <sub>5</sub> :Ce,Tb	400 nm	Blue	1.2 $\mu\text{m}$	6 $\mu\text{m}$

Table 1: phosphors deposited and principal characteristics. All phosphors were purchased from the Phosphor Technology Company.



(a)



(b)

Fig.2: SEM images of (a) patterned silicon substrate and (b) holes filled with P46 phosphors. No significant damage has been observed on the silicon substrate after the fabrication process.

A scheme of the process of phosphor deposition is shown in Fig. 3:

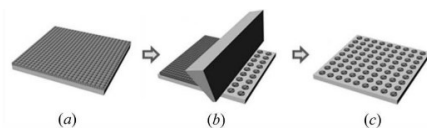


Fig. 3: scheme of the process of phosphor deposition: (a) sample coated with phosphors

after the mechanical filling: phosphors are aligned in the cavities and are also present on the surface of the sample; (b) removal of excess phosphor by the doctor blade technique; (c) final PPD with holes completely filled with phosphors.

Half of the samples have been processed in order to coat the PPD surface with a 100 nm-thick film of ITO. The ITO film was deposited to prevent leakage of the phosphors powder from the holes and to limit the absorption of water and contaminants on the powders. A suitable magnetron sputtering process was implemented (power: 300 W; pressure: 0.012 mbar; Ar flux: 25 sccm; sample temperature: 473 K) in order not to damage the phosphors. A SEM image of the cross section obtained by a focused ion beam (FIB) of two pixels filled with P46 phosphors and coated with an ITO layer is shown in Fig. 4.

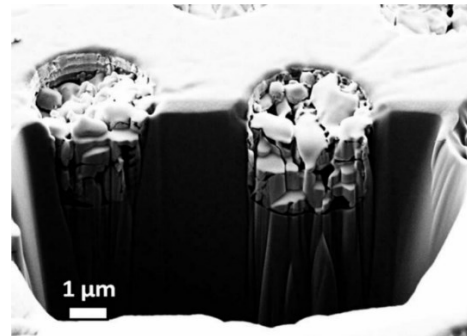


Fig. 4: SEM image of the FIB cross section of two pixels covered with 100 nm of ITO layer.

The homogeneity of the pixelated device has been investigated. Fig. 5 shows SEM images of two PPDs with P46 phosphors after FEL characterization, in the presence (Fig. 5a) and in the absence of an ITO film (Fig. 5b). A larger number of dark pixels can be observed in the second device. Higher magnification (insert in Fig. 5b) reveals a partial filling of the cavities, probably generated by a leak of phosphors; in contrast, the ITO-coated pixels look unaffected, in accordance with the hypothesis that the ITO coating acts as

a barrier to the leakage of the phosphors from the silicon cavities.

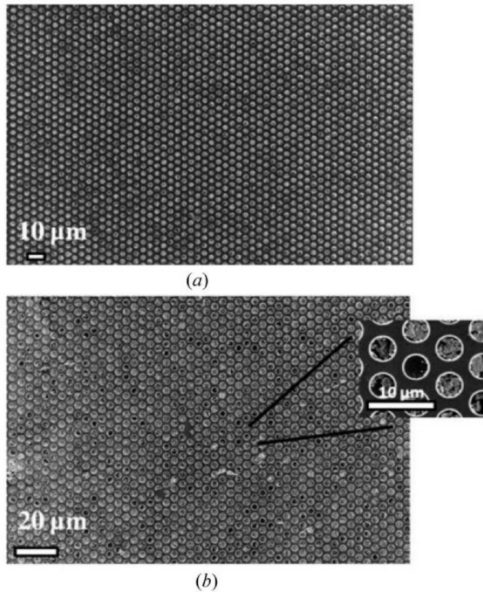


Fig. 5: SEM images of PPD P46 filled after FEL measurements: (a) with ITO coating; (b) without ITO coating; the insert in (b) shows a magnification of the indicated area: partial filled cavities are visible.

## 2.2. Experimental setup

The experimental tests were performed at the EIS-TIMEX beamline (Masciovecchio et al., 2015) at the FERMI FEL in Trieste (Zangrando et al., 2014). The beamline optical design is characterized by an ellipsoidal focusing mirror of 1.4 m focal length. Phosphors fluorescence was detected with a telemicroscope, the Questar QM 100 long distance microscope, coupled to a visible CCD camera: Basler Scout scA640-74gm, monochromatic, 12-bit depth and dynamic range of 10.7 bit. The telemicroscope was placed 350 mm from the PPD at an angle of about  $20^\circ$  with respect to the direction of the incoming FEL light. In this configuration, the resolution is better than 5  $\mu\text{m}$ , the focal depth is a few tens of micrometers with a field of view about 600  $\mu\text{m}$ . A scheme of the experimental setup is shown in Fig. 6.

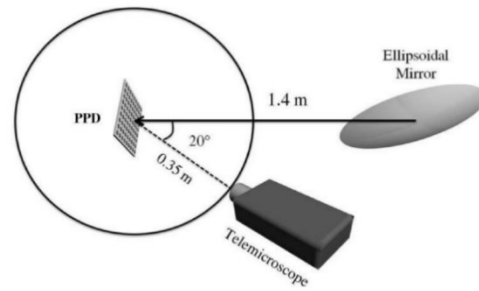


Fig. 6: scheme of the experimental setup of the EIS-TIMEX beamline.

The telemicroscope calibration was performed before each measurement through the use of a micrometric scale, so the magnification is taken into account in every acquisition. A typical calibration achieved with the current set-up is of the order of 1000 pixels per  $\mu\text{m}$ , which yields a resolution of 1  $\mu\text{m}$  per pixel, near to the optical resolution dictated by the telemicroscope itself.

## 3. Results and discussion

For the first set of measurements a PPD filled with P46 phosphors was used. For the present measurement campaign, the FEL was characterized by a pulse energy of 7  $\mu\text{J}$  and the wavelength used was 30.5 nm (40.7 eV). The intensity of the even harmonics is zero for the in-axis emission, while the intensity of the third harmonic is below 1% (Schmüser et al., 2008). Fig. 7(a) shows a CCD image of the PPD irradiated by ten shots of the photon beam; the CCD camera was operated at a frame rate of 10 Hz, so the integration of ten shots was achieved by an exposure of 1 s. Fig. 7(b) shows the same PPD after 10 s of exposure to the FEL radiation. Indeed, after 10 s of exposure, pixels lose intensity due to radiation damage, which causes ablation both of the substrate and of the phosphor pixels; studies on the damage threshold of the phosphors must be made to understand how many shots the phosphors are able to withstand. The

direct observation of the light emitted by the illuminated pixels allows the size of the central spot to be estimated due to the fundamental harmonic: knowing the period of the lattice ( $6\ \mu\text{m}$ ), supposing a single PPD pixel becomes illuminated, allows us to estimate that the central spot will be completely included in an area with a diameter of  $8\ \mu\text{m}$  maximum. At the moment, a higher precision in the beam estimation cannot be provided due to the PPD resolution which is related to the size of the pixels and the characteristics of the telemicroscope. According to the specification, we know that the beam divergence is  $50\ \mu\text{rad}$  and the expected spot size is  $4.4\ \mu\text{m}$  FWHM (Masciovecchio et al., 2015), in agreement with our measurements. In Figs. 7(c) and 7(d) measurements of ITO-coated PPDs are shown: it has been observed that the halo is weaker than in the case of the PPD without an ITO layer.

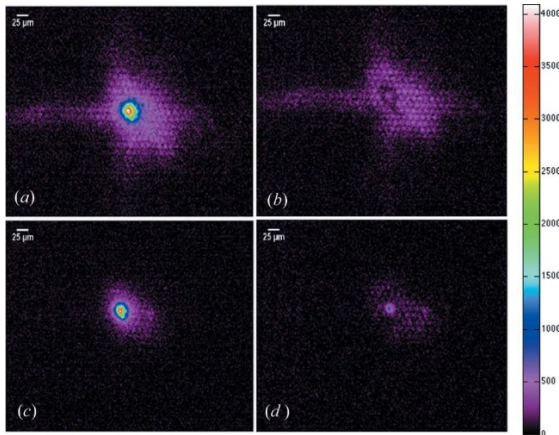


Fig. 7: CCD camera image of the PPD with P46 phosphors hit with a pulse energy of  $7\ \mu\text{J}$  at  $30.5\ \text{nm}$  wavelength; (a) integration of 10 FEL shots (1 s of integration) on not coated PPD; (b) PPD after 10 s of exposure to the FEL beam; (c) integration of 10 FEL shots (1 s of integration) on PPD ITO coated; (d) PPD ITO coated after 10 s of exposure to the FEL beam.

In the second set of measurements, a P47-phosphors-based PPD has been used. The experiment was performed on PPD coated and not coated with ITO. Fig. 8(a) shows

measurements on a PPD with P47 phosphors without an ITO layer after 1 s of exposure to the photon beam, and Fig. 8(b) shows a PPD after 10 s of exposure; Fig. 8(c) shows a PPD with P47 phosphors ITO coated after 1 s of exposure and Fig. 8(d) shows it after 10 s. Even the use of P47 allows the measurement of the size of the central beam spot (the limit in resolution is again  $8\ \mu\text{m}$ ). As previously shown, the layer of ITO leads to a reduction of the halo.

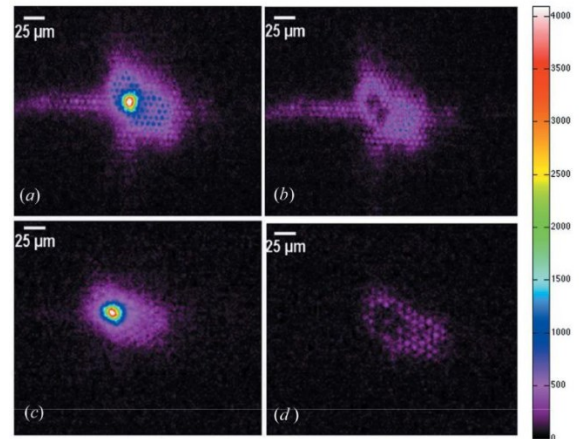


Fig. 8: CCD camera image of the PPD with P47 phosphors hit with a pulse energy of  $7\ \mu\text{J}$  and  $30.5\ \text{nm}$  wavelength; (a) integration of 10 FEL shots (1 s of integration) on not coated PPD; (b) PPD after 10 s of exposure to the FEL beam; (c) integration of 10 FEL shots (1 s of integration) on PPD ITO coated; (d) PPD ITO coated after 10 s of exposure to the FEL beam.

In order to understand the absorption effect of the ITO layer, we have performed a characterization of the UV–Vis absorption of a film deposited under the same conditions of the capping layer on the PPDs. The measurements were carried out with a UV–Vis spectrometer on a  $100\ \text{nm}$ -thick ITO film deposited on a glass slide. The spectrum (Fig. 9) shows that at the maximum emission wavelength of the P46 ( $544\ \text{nm}$ ) phosphor the transmission of the ITO is around 90%, while for P47 ( $400\ \text{nm}$ ) phosphor it is almost 70%. If the layer of ITO absorbs part of the radiation emitted by the phosphor, the halo on P46-

filled PPD should be greater than that of the P47-filled PPD; because a slight dimming of the light is observed in the case of P46, we can conclude that the ITO cannot act as a filter for the light emitted by the phosphors. We can assume that the ITO could filter some components of the FEL beam, opening up the possibility of generating a selective filter directly in the screen detector just by changing the capping layer. Additional studies on ITO are essential in order to understand what harmonics are filtered and the mechanism of the process.

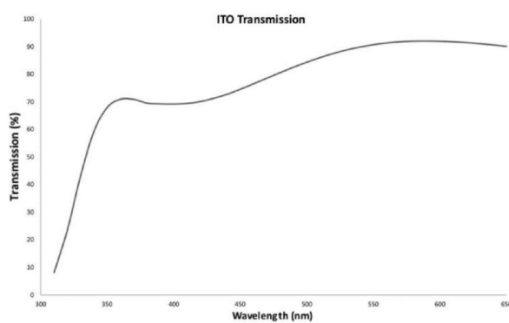


Fig. 9: UV-Vis spectrum of a 100 nm-thick ITO layer deposited on glass.

The last set of measurements has been performed to compare frosted P46 phosphor with a P46 phosphors PPD. Exposures were performed at a pulse energy of 1  $\mu$ J and a wavelength of 17 nm (energy 72.94 eV); the beam profile imaging is shown in Fig. 10. The difference in wavelength with respect to the previous measurements is due to a different tune of the machine, yet Fig. 10 suggests that the harmonic content is preserved. The present measurements were collected ‘out of focus’, but still allow us to derive important information such as the shape of the halo due to the other harmonics. The imaging with frosted P46 (Fig. 10a) is affected by the diffusion of emitted light in the phosphors: from the result it is impossible to clearly recognize the outlines of the halo due to higher-order harmonics. Indeed the PPD (Fig. 10b) allows us to accurately track the shape of

the beam and to distinguish the fundamental harmonic from the other components. After 30 s of exposure to the beam (Fig. 10c) the radiation damage became evident, as in the previous experiments; nevertheless, the spatial imaging of the beam can still be acquired and characterized.

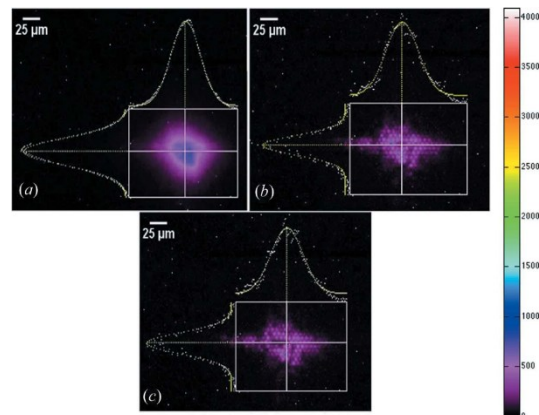


Fig. 10: CCD camera images at 1  $\mu$ J pulse energy and 17 nm wavelength of: (a) frosted P46 phosphor after 1 s of exposure to the photon beam; measured spot size of horizontal r.m.s.: 46  $\mu$ m; vertical r.m.s.: 37  $\mu$ m; (b) PPD P46 filled after 1 s of exposure to the photon beam; horizontal r.m.s.: 41  $\mu$ m; vertical r.m.s.: 25  $\mu$ m; (c) PPD P46 filled after 30 s of exposure to the photon beam; horizontal r.m.s.: 46  $\mu$ m; vertical r.m.s.: 28  $\mu$ m.

#### 4. Conclusions and outlooks

A new beam detector has been produced and tested. A suitable and up-scalable fabrication process has produced a cost-effective and customizable device for FEL beam diagnosis through indirect imaging. Our devices demonstrated clear advantages when employed in high-flux beamlines (such as the EIS-TIMEX beamline in FERMI@ELETTRA FEL) that require the precise characterization of the focal spot to evaluate critical quantities such as the fluence on the sample. The PPD has demonstrated to be a powerful online tool for the beam diagnosis allowing superior spatial resolution in the

imaging of the beam spot with respect to the YAG scintillators, remaining, at the same time, a real-time and in situ technique. Moreover, the regular structure will allow the implementation of an automatic focusing system for CCD cameras capable of moving the PPD in the optical axis of the focusing optics and measuring the spot size counting the number of the illuminated pixels. Every limitation owing to an incorrect visualization of the surface can be easily corrected due to the well known periodicity of the PPD surface itself.

We demonstrated that our system can be easily customized to use different phosphors in order to match the requirements of FEL wavelengths and decay time. Future development of the present work includes the tailoring of the composition and mixing of the phosphors deposited into the PPD. Higher resolution in the spot size measurement can be reached by changing the size of the holes (pixels), while by increasing the periodicity of the lattice it will be possible to improve the quality of the beam-shape evaluation.

The present measurement campaign suggests that the ITO coating could effectively work as a filter for some radiation components. A complete and detailed study of the role of the ITO coating has to be carried out to fully determine the spectral response of the coating itself. We plan to conduct absorption and transmission studies on the ITO layers with synchrotron radiation over a wide range of energy useful for FEL analysis.

A possible development of this kind of detector consists of making holes in a reflecting metal: this will direct all the phosphor-produced light toward the surface increasing the efficiency of PPD itself and making it more sensitive to weaker beams. For this reason, it could be possible to extend this imaging technique to other types of source such as synchrotron radiation.

## Acknowledgements

The authors want to thank all colleagues of FERMI who made this work possible, in particular all the staff of EIS-TIMEX and DiProi and the FERMI Commissioning Team. A sincere thanks also to the Detectors & Instrumentation laboratory staff and to the people of Istituto Officina dei Materiali. Thanks also to B. Marmiroli for help in the microfabrication. The work has partially been funded by Italian Ministry of Education MIUR (FIRB RBAP11ETKA\_003).

## References

- Allaria, E. et al. (2012). *Nat. Photon.* 6, 699–704.
- Ayvazyan, V. et al. (2002). *Phys. Rev. Lett.* 88, 104802.
- Cha, B. K., Lee, S. J., Muralidharan, P., Kim, D. K., Kim, J. Y., Cho, G., Jeon, S. & Huh, Y. (2011). *Nucl. Instrum. Methods Phys. Res. A*, 652, 717–720.
- Chalupský, J., Bohacek, P., Hajkova, V., Hau-Riege, S. P., Heimann, P. A., Juha, L., Krzywinski, J., Messerschmidt, M., Moeller, S. P., Nagler, B., Rowen, M., Schlotter, W. F., Swiggers, M. L. & Turner, J. J. (2011). *Nucl. Instrum. Methods Phys. Res. A*, 631, 130–133.
- Chalupský, J. et al. (2007). *Opt. Express*, 15, 6036–6043.
- Chang, C., Wang, Y.-F., Kanamori, Y., Shih, J.-J., Kawai, Y., Lee, C.-K., Wu, K.-C. & Esashi, M. (2005). *J. Micromech. Microeng.* 15, 580–585.
- Flöter, B., Juranic, P., Kapitzki, S., Keitel, B., Mann, K., Ploñjes, E., Schäfer, B. & Tiedtke, K. (2010). *New J. Phys.* 12, 083015.
- Gerasimova, N., Dzierzhytski, S., Weigelt, H., Chalupský, J., Hájková, V., Vysin, L. & Juha, L. (2013). *Rev. Sci. Instrum.* 84, 065104.
- Green, M. A. & Keevers, M. J. (1995). *Prog. Photovolt.* 3, 189–192. Masciovecchio, C. et al. (2015). *J. Synchrotron Rad.* 22, 553–564.
- Mimura, H., Handa, S., Kimura, T., Yumoto, H., Yamakawa, D., Yokoyama, H., Matsuyama, S., Inagaki, K., Yamamura, K., Sano, Y., Tamasaku, K., Nishino, Y.,

- Yabashi, M., Ishikawa, T. & Yamauchi, K. (2010). *Nat. Phys.* 6, 122–125.
- Nagarkar, V. V., Gupta, T. K., Miller, S. R., Klugerman, Y., Squillante, M. R. & Entine, G. (1998). *IEEE Trans. Nucl. Sci.* 45, 492–496.
- Schmüser, P., Dohlus, M. & Rossbach, J. (2008). *Ultraviolet and Soft X-ray Free-Electron Lasers: Introduction to Physical Principles, Experimental Results, Technological Challenges*, Springer Series Tracts in Modern Physics. Berlin: Springer.
- Svenonius, O., Sahlholm, A., Wiklund, P. & Linnros, J. (2009). *Nucl. Instrum. Methods Phys. Res. A*, 607 138–140.
- Tiedtke, K. et al. (2009). *New J. Phys.* 11, 023029.
- Yen, W. M., Shionoya, S. & Yamamoto, H. (2007). *Phosphor Handbook*. Boca Raton: CRC Press/Taylor & Francis.
- Zangrando, M., Mahne, N., Raimondi, L. & Svetina, C. (2014). *Optical Technologies for Extreme Ultraviolet and Soft X-ray Coherent Sources*, Springer Series in Optical Sciences, Vol. 197, edited by F. Canova and L. Poletto. Berlin: Springer.



## Toward an integrated device for spatiotemporal superposition of free-electron lasers and laser pulses

Vol. 41, No. 21/ November 1 2016/ Optics Letters 5090-5093

RICCARDO MINCIGRUCCI,<sup>1,\*</sup> ALESSIA MATRUGLIO,<sup>2,3</sup> ANDREA CALVI,<sup>4</sup> LAURA FOGLIA,<sup>1</sup> EMILIANO PRINCIPI,<sup>1</sup> ALBERTO SIMONCIG,<sup>1</sup> FILIPPO BENCIVENGA,<sup>1</sup> STEFANO DALLORTO,<sup>5,6,7</sup> ALESSANDRO GESSINI,<sup>1</sup> GABOR KURDI,<sup>1</sup> DEIRDRE OLYNICK,<sup>5</sup> SCOTT DHUEY,<sup>5</sup> RUDI SERGO,<sup>8</sup> MARCO LAZZARINO,<sup>2</sup> CLAUDIO MASCIOVECCHIO,<sup>1</sup> AND SIMONE DAL ZILIO<sup>2</sup>

<sup>1</sup>Elettra Sincrotrone Trieste, Area Science Park Basovizza S.S. 14 Km 163.5, Trieste 34149, Italy. <sup>2</sup>IOM Laboratorio Nazionale TASC, CNR, Area Science Park Basovizza S.S. 14 Km 163.5, Trieste 34149, Italy. <sup>3</sup>Graduate School in Nanotechnology, University of Trieste, Piazzale Europa 1, Trieste 34127, Italy. <sup>4</sup>Dipartimento di Fisica, Università degli Studi di Trieste, via A. Valerio 2, I-34127 Trieste, Italy. <sup>5</sup>Molecular Foundry, 1 Cyclotron Road, Berkeley, California 94720, USA. <sup>6</sup>Department of Micro- and Nanoelectronic Systems, Institute of Micro and Nanoelectronics, Faculty of Electrical Engineering and Information Technology, Ilmenau University of Technology, Gustav-Kirchhoff-Straße 1, Ilmenau 98693, Germany. <sup>7</sup>Oxford Instruments, 300 Baker Avenue, Suite 150, Concord, Massachusetts 01742, USA. <sup>8</sup>Detector and Instrumentation Laboratory, Elettra Sincrotrone Trieste, Area Science Park Basovizza S.S. 14 Km 163.5, Trieste 34149, Italy. \* corresponding author.

Free-electron lasers (FELs) currently represent a step forward on time-resolved investigations on any phase of matter through pump-probe methods involving FELs and laser beams. That class of experiments requires an accurate spatial and temporal superposition of pump and probe beams on the sample, which at present is still a critical procedure. More efficient approaches are demanded to quickly achieve the superposition and synchronization of the beams. Here, we present what we believe is a novel technique based on an integrated device allowing the simultaneous characterization and the fast spatial and temporal overlapping of

the beams, reducing the alignment procedure from hours to minutes.

Time-resolved investigations have begun a new era of chemistry and physics, enabling the monitoring in real time of the dynamics of chemical reactions and matter [1]. Generally, in such kinds of studies, one or more laser pulses acts as the pump, triggering a particular process such as ultrafast melting [2,3], demagnetization dynamics [4,5], impulsive stimulated scattering [6,7], and coherent antiStokes Raman scattering [8–10], to name a few. The particular dynamics triggered by the pump pulse is then probed by another laser pulse which, properly delayed, encodes the temporal

information of the process (e.g., in the scattered intensity). The physical information is thus contained in the temporal trace of the monitored physical quantity obtained by varying the pump-probe delay. A further step in time-resolved investigations has been achieved with the advent of free-electron lasers (FELs), which permitted the addition of chemical and elemental selectivity to the above-mentioned studies [11–13]. In general, any pump-probe study requires the spatial and temporal superposition of the pump and probe lasers, which is realized by exploiting the peculiar properties of different samples. In particular, in the FEL-optical laser class of experiments, the first step is the spatial superposition of the two beams, which is usually accomplished using a cerium-doped yttrium aluminum (Al) garnet fluorescent screen (YAG:Ce); the FEL-induced fluorescence is used to define the FEL position on the sample to which the optical laser is subsequently super-posed. We have already presented a novel pixelated phosphor detector (PPD), which allows an improvement with respect to standard YAG as far as FEL diagnostics is concerned [14]. Once the spatial superposition has been achieved, the YAG is substituted with an antenna [15] coupled with an oscilloscope and used to roughly align the two pulses in time. This super-position is conducted looking at the electrical signals generated by the FEL and the laser; the relative delay is adjusted until the rising edges of the two are overlapped. This procedure is quite inaccurate, and the delay value can be determined only with a 30 ps error, a value that is dictated by the intrinsic temporal resolution of the common oscilloscopes. The subpicosecond synchronization requires a much faster diagnostic, and the finer temporal superposition is subsequently conducted using a third sample (e.g.,  $\text{Si}_3\text{N}_4$  or  $\text{Al}_2\text{O}_3$  crystals) and monitoring the FEL-induced changes in the visible/IR optical

properties. In insulators and semiconductors, the main process, which underlies the optical property changes, is believed to be a partial depletion of the valence band, resulting in an induced absorption [16]; the imaginary part “ $k$ ” of the refractive index increases, and this should manifest in a diminished reflection and/or transmission, accompanied by a perturbation of the value of the real part of the refractive index, which can cause an interferential demagnification of the transient signal [17,18]. The overall procedure is generally time-consuming and highly complex. Each sample is employed for its peculiar characteristics, and only for a specific task of the overall alignment procedure. This is inefficient and not robust. First of all, the spatial superposition has to be preserved during the temporal alignment steps. This is commonly obtained by using as a reference the image of a CCD camera; after the spatial superposition, the CCD is put in focus and thus every sub-sequent sample has to be adjusted in order to reach the same level of focus. The quality of the focus is defined by a human user and is influenced by the quality of the sample surface, by the illumination, and by the geometry of the imaging setup. A second and more substantial problem in the alignment procedure is represented by the scarce contrast of the transient signal; since the FEL spot can be smaller than the laser spot, the valence band is depleted by the FEL radiation only in a fraction of the sample surface. Therefore, a fraction of the visible laser is reflected or transmitted by an unexcited sample, giving rise to a dominant baseline over which to detect the transient signal. We propose here a beam monitor designed to increase the contrast and to speed up the alignment procedure. The ideal sample should possess the fluorescence characteristics of a YAG screen and at the same time be suitable for the temporal overlapping procedure with an increased contrast.

This can be obtained, for example, by embedding some  $\text{Al}_2\text{O}_3$  timing zones in a modified version of the PPD previously proposed by our group [14]; we call this enhanced version PPD 2.0. This new device would permit employing adjacent portions of the same surface to spatially (using the phosphors pixels) and temporally (using the  $\text{Al}_2\text{O}_3$  islands) superpose the FEL and laser beams. A simple strategy to drastically increase the contrast is to operate in transmission (thus looking for a change in transmittivity induced by the FEL pulse) and to create a pinhole around the  $\text{Al}_2\text{O}_3$  zones. The pinhole, realized by a reflective material for the visible/IR laser, should be smaller or comparable to the FEL beam size. This permits geometrically blocking the circular crown of the laser spot that would not interact with the FEL-excited portion of the  $\text{Al}_2\text{O}_3$ , avoiding the origin of baseline contribution, as shown in the sketch in Fig. 1.

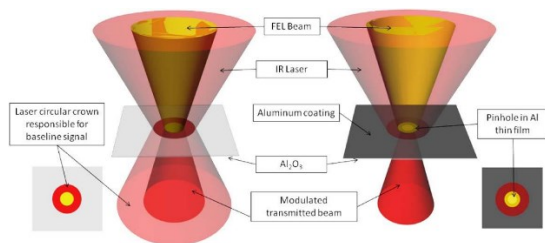


Fig. 1. Left part: sketch of usual superposition between the laser and FEL spots. The circular crown of the laser spot not excited by the FEL produces a non-negligible baseline. Right part: the introduction of a pinhole equal or smaller than the FEL spot cuts the unexcited circular crown, increasing the contrast.

A scheme of the fabrication process of such a sample is reported in Fig. 2; in detail, a fused silica wafer (250  $\mu\text{m}$  thick) is coated with 50 nm thick chromium (Cr) thin film via e-beam evaporation and with 400 nm of ZEP 520A resist for the following lithography. The micrometric honeycomb pattern is achieved by direct

e-beam lithography (EBL) at 200 kV and 1 nA using a Vistec VB-300 EBL system [Fig. 2(a)]. Cr wet etching is used for pattern transfer on a metal mask. For the transfer in the silica substrate, a plasma etching process is carried out with a multiple frequency parallel plate etching tool with 60 MHz on the top plate and 13.56 MHz on the bottom plate (Oxford Plasma lab 100 Viper). The periodic lattice of micrometric pixels is etched through 4  $\mu\text{m}$  of fused silica with a mixture of 70 sccm  $\text{CF}_4$  40%  $\text{O}_2$  at 20 mTorr of pressure, 150 W of radio-frequency power and 400 W VHF forward power [Fig. 2(b)]. The diameter and period of holes are 2  $\mu\text{m}$  and 4  $\mu\text{m}$ , respectively, with a total fill factor of an active area close to 20%. After the etching step, the surface is covered with a 250-nm-thick  $\text{Al}_2\text{O}_3$  deposited by plasma-enhanced atomic layer deposition (ALD) at 40°C (Oxford FlexAl) [Fig. 2(c)]. After that, a conformal layer of 100 nm of Al is evaporated on the sample by the Glancing Angle Deposition (GLAD) process [Fig. 2(d)]; the metal thin film is needed to re-duce the cross talk between the pixels of phosphor and to achieve the desired pinhole structures where the visible/IR laser is trans-mitted. The patterning of the Al layer is performed by selectively removing the metal layer, avoiding the damaging of  $\text{Al}_2\text{O}_3$  under the layer by the focused ion beam (FIB) process [Fig. 2(e)]. The final step is the deposition of phosphors inside the 2  $\mu\text{m}$  cavities [Fig. 2(f)]; the process is described in Ref. [14]. The P20 used phosphor is commercially available at Phosphor Technology Company.

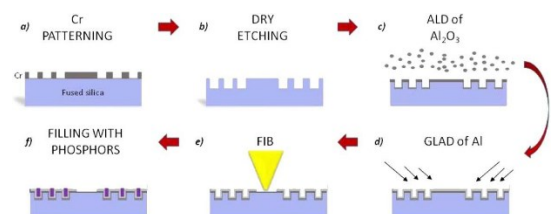


Fig. 2. Scheme of the fabrication process. (a) EBL on Cr-coated fused silica; (b) dry

etching of fused silica; (c) ALD of  $\text{Al}_2\text{O}_3$ ; (d) GLAD deposition of Al; (e) FIB process; (f) phosphor deposition.

Scanning electron microscopy (SEM) images of the sample before [Fig. 3(a)] and after the phosphors' deposition [Fig. 3(b)] are presented. The average grain size of powder ranges from a minimum of  $1.2\ \mu\text{m}$  to a maximum of  $6\ \mu\text{m}$ , as reported by the company. The  $2\ \mu\text{m}$  holes are thus fillable only with a small fraction of the available grains. This causes an incomplete filling and a decrease in the FEL-visible conversion efficiency.

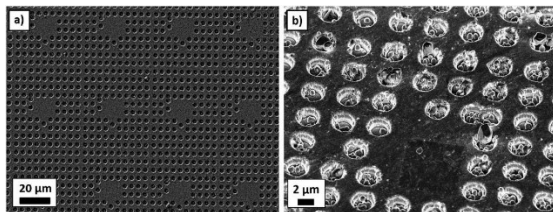


Fig. 3. SEM images of the device. (a) Before FIB and the filling with phosphors; (b) after phosphor deposition. An  $\text{Al}_2\text{O}_3$  island and the phosphor presence can be noticed in the microcavities.

After the fabrication, the sample was installed and tested at the EIS-TIMEX beam line [19], at the FERMI FEL facility. The beam line is conceived to operate pump-probe experiments in a high-fluency regime both for the FEL and IR laser. For this purpose, it is equipped on the FEL side with an ellipsoidal gold-coated mirror able to focus the FEL emission down to  $6\ \mu\text{m}$  at full width half maximum (FWHM). In such conditions, the FEL is generally destructive, an undesired feature as far as the overlapping procedure is concerned. The superposition is thus conducted out of the focal plane of the FEL, where the spot has a dimension of  $15\ \mu\text{m}$ , and decreases the intensity at the source down to  $1\ \mu\text{J}$ . In the present case, the FEL wavelength was  $32\ \text{nm}$ . The employed IR laser had a FWHM of  $50\ \mu\text{m}$  and an intensity of  $0.1\ \mu\text{J}$ . Figure 4 (upper part) reports a schematic of the

experimental setup. The sample was rotated by  $20^\circ$  with respect to the FEL beam, due to a mechanical constraint of the manipulator. The spatial overlap was conducted in such rotated geometry. The bottom part of Fig. 4 shows the images of the spots acquired for the FEL and the IR on the above described sample. The images have been acquired using a Questar QM 100 telemicroscope, operated in air and coupled to a Basler ACE CCD camera.

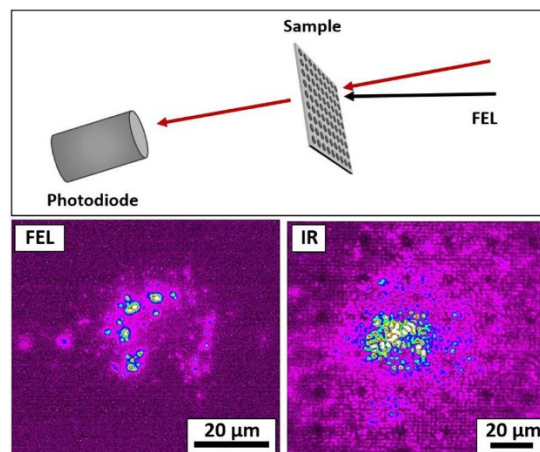


Fig. 4. Upper part: sketch of the experimental apparatus. Lower part: FEL spot (on the left) and IR laser spot (on the right). A lack of luminosity in the lower right part of both the spots identifies the presence of an  $\text{Al}_2\text{O}_3$  timing zone (represented also in the SEM image in the inset). The images were obtained using a Questar QM100 telemicroscope operated in air and coupled to a CCD camera.

By comparing the images, it is easy to observe that the laser spot is roughly twice as large as the FEL spot. The inhomogeneous readout of the FEL spot intensity is due to the incomplete filling of the phosphor holes: it is also possible to recognize on the lower/right part the lack of intensity of the spot that corresponds to the unpatterned area of the  $\text{Al}_2\text{O}_3$  timing island. The fine-timing procedure was subsequently conducted monitoring the time evolution of the transmittivity of the  $\text{Al}_2\text{O}_3$ -excited island. An UVG100 (OptoDiode) photo-diode was employed

to detect the transmitted IR intensity. Figure 5 reports the relative change of transmittivity of our device (red trace) and, for comparison, the one recorded on the bulk  $\text{Al}_2\text{O}_3$  (black trace) and on a 100 nm Ni-coated bulk  $\text{Al}_2\text{O}_3$  (blue trace). All the measurements were conducted under the same FEL and laser conditions. To obtain the traces shown in Fig. 5, the delay between the IR and FEL laser was continuously increased and the shot-to-shot transmitted intensity was recorded. This procedure was repeated three times for each sample, and the single traces have been averaged and binned with 20 fs steps. The error bars are one standard error.

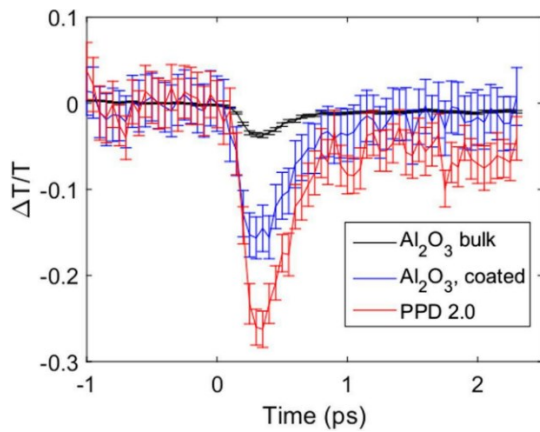


Fig. 5. Fine-timing traces acquired on the same FEL/IR laser condition on three different samples: bulk  $\text{Al}_2\text{O}_3$  (black trace), Ni-coated bulk  $\text{Al}_2\text{O}_3$  (blue trace), and our sample (red trace).

The bulk  $\text{Al}_2\text{O}_3$  exhibits a change of the transmittivity in the order of a few percent, comparable with the standard timing traces generally reported in the literature [18,20].

In contrast, on our device the transmittivity change is amplified by cutting the fraction of the IR that does not interact with the excited region of the sample. As expected, this increases the intensity of the effect up to  $\sim 25\%$ . The blue trace is instead obtained on a nominally identical  $\text{Al}_2\text{O}_3$  sample coated with 100 nm of Ni. The coating is removed by exposing the sample to an unattenuated

FEL. The high-intensity FEL drills a hole of its dimensions, which can subsequently be used as an  $\text{Al}_2\text{O}_3$  island to perform the fine timing with an attenuated FEL. Such a procedure is a valid alternative that also produces a contrast increase with respect to the uncoated bulk sample, but does not possess the capabilities for the spatial alignment offered by the PPD approach.

In conclusion, we have determined two different procedures to solve the identified common problems responsible for the scarce contrast in the temporal overlapping procedure of the FEL and laser pulses: the introduction of a metallic coating, subsequently removed by a high-intensity FEL, and the creation of a purposely designed sample with well-defined pinholes. The PPD 2.0 permits an increase in the contrast by a factor  $\sim 7$  with respect to the bulk  $\text{Al}_2\text{O}_3$  crystal, being contemporarily exploitable for the spatial overlapping procedure. This allows more efficiency in the overall superposition procedure in terms of time and spatial precision, since it does not require the use of different crystals with their own characteristics. The integration of currently used tools can be pushed further with the introduction of an electric contact on the surface coating; that would allow operating our sample as the antenna described in Refs. [15,21] and also conducting the raw-timing procedure on the same spot. Specific setups exploiting high-resolution spatial detection devices can be employed to have even higher contrast in the timing signal. However, such types of setups have to be carefully designed and aligned to detect the reflected or transmitted signal [22–24]. Instead, our device can be fruitfully inserted in any existing transmission setup, achieving at the same time an increase in the available space and an augmented contrast in the timing signal. The geometrical parameters of the PPD 2.0, such as relative distances, diameters, and depths, can be easily modified to extend its use toward non-collinear

geometries, where small spatial deviations between the YAG screen and the timing sample may also become important. An increase of the cavities' diameter may also bring an efficiency increase due to an augmented filling factor. It is important to have a compromise between the filling of the cavities and their size: large diameters (tens of  $\mu\text{m}$ ) reduce the resolution in the diagnostic of the FEL beam; a diameter of 4  $\mu\text{m}$  can be a good compromise with this type of phosphors, as already demonstrated by our group. Moreover, as far as the linear absorption process holds for the timing material [22], our device can be employed with identical advantages in terms of contrast increase and speeding up the overall procedure. The only constraint is regarding the dimensions of the timing islands, which have to be rescaled according to the adopted FEL focal spot size. A study on different materials that change their optical properties when exposed to the FEL beam, such as  $\text{Si}_3\text{N}_4$ , GaAs,  $\text{MgF}_2$ , or wide bandgap insulators could be interesting to determine the best material to further increase the contrast and in principle speed up the overlapping procedure.

**Funding.** Consiglio Nazionale delle Ricerche (CNR); Ministero dell'Istruzione, dell'Università e della Ricerca (MIUR) (FIRB RBAP11ETKA 003); Office of Science (SC); Office of Basic Energy Sciences; Scientific User Facilities Division; U.S. Department of Energy (DOE) (DE-AC02-05CH11231).

**Acknowledgment.** This work was partially performed at the Molecular Foundry, Lawrence Berkeley National Laboratory. The support of the PADReS team is acknowledged.

## REFERENCES

1. A. H. Zewail, in *Nobel Lectures in Chemistry*, I. Grethe, ed. (1996 – 2000).

2. M. Beye, F. Sorgenfrei, W. F. Schlotter, W. Wurth, and A. Föhlisch, *Proc. Natl. Acad. Sci. USA* 107, 16772 (2010).
3. N. Medvedev, Z. Li, and B. Ziaja, *Phys. Rev. B* 91, 1 (2015).
4. B. Vodungbo, B. Tudu, J. Perron, R. Delaunay, L. Müller, M. H. Berntsen, G. Grübel, G. Malinowski, C. Weier, J. Gautier, G. Lambert, P. Zeitoun, C. Gutt, E. Jal, A. H. Reid, P. W. Granitzka, N. Jaouen, G. L. Dakovski, S. Moeller, M. P. Minitti, A. Mitra, S. Carron, B. Pfau, C. von Korff Schmising, M. Schneider, S. Eisebitt, and J. Lüning, *Sci. Rep.* 6, 18970 (2016).
5. C. Von Korff Schmising, M. Giovannella, D. Weder, S. Schaffert, J. L. Webb, and S. Eisebitt, *New J. Phys.* 17, 033047 (2015).
6. Y.-X. Yan, E. B. Gamble, Jr., and K. A. Nelson, *J. Chem. Phys.* 83, 5391 (1985).
7. S. Fujiyoshi, S. Takeuchi, and T. Tahara, *J. Phys. Chem. A* 107, 494 (2003).
8. F. El-Diasty, *Vib. Spectrosc.* 55, 1 (2011).
9. G. Knopp, P. Radi, M. Tulej, T. Gerber, and P. Beaud, *J. Chem. Phys.* 118, 8223 (2003).
10. H. U. Stauffer, J. D. Miller, M. N. Slipchenko, T. R. Meyer, B. D. Prince, S. Roy, and J. R. Gord, *J. Chem. Phys.* 140, 024316 (2014).
11. S. Tanaka and S. Mukamel, *J. Chem. Phys.* 116, 1877 (2002).
12. S. Tanaka and S. Mukamel, *Phys. Rev. Lett.* 89, 043001 (2002).
13. S. Mukamel and S. Tanaka, *Phys. Rev. A* 64, 032503 (2001).
14. A. Matruglio, S. Dal Zilio, R. Sergo, R. Mincigrucci, C. Svetina, E. Principi, N. Mahne, L. Raimondi, A. Turchet, C. Masciovecchio, M. Lazzarino, G. Cautero, and M. Zangrando, *J. Synchrotron Radiat.* 23, 29 (2016).
15. M. B. Danailov, F. Bencivenga, F. Capotondi, F. Casolari, P. Cinquegrana, A. Demidovich, E. Giangrisostomi, M. P. Kiskinova, G. Kurdi, M. Manfredda, C. Masciovecchio, R. Mincigrucci, I. P. Nikolov, E. Pedersoli, E. Principi, and P. Sigalotti, *Opt. Express* 22, 12869 (2014).
16. S. M. Durbin, *AIP Adv.* 2, 042151 (2012).
17. F. Casolari, F. Bencivenga, F. Capotondi, E. Giangrisostomi, M. Manfredda, R. Mincigrucci, E. Pedersoli, E. Principi, C. Masciovecchio, and M. Kiskinova, *Appl. Phys. Lett.* 104, 191104 (2014).
18. S. Eckert, M. Beye, A. Pietzsch, W. Quevedo, M. Hantschmann, M. Ochmann, M. Ross, M. P. Minitti, J. J. Turner, S. P. Moeller, W. F. Schlotter, G. L. Dakovski, M. Khalil, N. Huse, and A. Föhlisch, *Appl. Phys. Lett.* 106, 061104 (2015).
19. C. Masciovecchio, A. Battistoni, E. Giangrisostomi, F. Bencivenga, E. Principi, R. Mincigrucci, R. Cucini, A. Gessini, F. D'Amico, R. Borghes, M. Prica, V. Chenda, M.

- Scarcia, G. Gaio, G. Kurdi, A. Demidovich, M. B. Danailov, A. Di Cicco, A. Filippini, R. Gunnella, K. Hatada, N. Mahne, L. Raimondi, C. Svetina, R. Godnig, A. Abrami, and M. Zangrando, *J. Synchrotron Radiat.* 22, 553 (2015).
20. C. Gahl, A. Azima, M. Beye, M. Deppe, K. Döbrich, U. Hasslinger, F. Hennies, A. Melnikov, M. Nagasono, A. Pietzsch, M. Wolf, W. Wurth, and A. Föhlisch, *Nat. Photonics* 2, 165 (2008).
21. L. Raimondi, C. Svetina, N. Mahne, D. Cocco, A. Abrami, M. De Marco, C. Fava, S. Gerusina, R. Gobessi, F. Capotondi, E. Pedersoli, M. Kiskinova, G. De Ninno, P. Zeitoun, G. Dovillaire, G. Lambert, W. Boutu, H. Merdji, A. I. Gonzalez, D. Gauthier, and M. Zangrando, *Nucl. Instrum. Methods Phys. Res. A* 710, 131 (2013).
22. R. Riedel, A. Al-Shemmary, M. Gensch, T. Golz, M. Harmand, N. Medvedev, M. J. Prandolini, K. Sokolowski-Tinten, S. Toleikis, U. Wegner, B. Ziaja, N. Stojanovic, and F. Tavella, *Nat. Commun.* 4, 1731 (2013).
23. S. Schorb, T. Gorkhover, J. P. Cryan, J. M. Glowina, M. R. Bionta, R. N. Coffee, B. Erk, R. Boll, C. Schmidt, D. Rolles, A. Rudenko, A. Rouzee, M. Swiggers, S. Carron, J. C. Castagna, J. D. Bozek, M. Messerschmidt, W. F. Schlotter, and C. Bostedt, *Appl. Phys. Lett.* 100, 121107 (2012).
24. T. Maltezopoulos, S. Cunovic, M. Wieland, M. Beye, A. Azima, H. Redlin, M. Krikunova, R. Kalms, U. Frühling, F. Budzyn, W. Wurth, A. Föhlisch, and M. Drescher, *New J. Phys.* 10, 033026 (2008).





# Contribution to international conferences

- TRENDS, WHISHES AND DREAMS (TWD) SYMPOSIUM ON DETECTION AND IMAGING TECHNOLOGIES.  
Barcelona, Spain. July, 2016.  
Talk and poster for the presentation of the project entitled “*Implemented Pixeled Phosphor Detector for laser coupled FEL beam diagnosis*”
- 60<sup>th</sup> INTERNATIONAL CONFERENCE ON ELECTRON, ION, AND PHOTON BEAM TECHNOLOGY AND NANOFABRICATION  
Pittsburgh, Pennsylvania, USA. June, 2016.  
Talk entitled “*Contamination-free suspended graphene structures by a Titanium-based transfer method*” (**Invited talk**)
- GRAPHENE 2016  
Genoa, Italy. April, 2016.  
Poster presentation entitled “*Contamination-free suspended graphene structures by a Ti-based transfer method*”
- 41<sup>st</sup> MICRO AND NANO ENGINEERING  
The Hague, Netherlands. September, 2015.  
Poster presentations of two works entitled “*A novel approach in the free-electron laser diagnosis based on Pixeled Phosphor Detector*” and “*Use of Titanium sacrificial layer for carbon-free graphene transfer method*” (**Winner of the “Best Poster Award in the Category Micro and Nano Patterning”**).
- WORKSHOP ON FEL PHOTON DIAGNOSTICS, INSTRUMENTATION, AND BEAMLINES DESIGN  
Trieste, Italy. May, 2015.  
Talk entitled “*A novel approach in the free-electron laser (FEL) diagnosis based on Pixeled Phosphor Detector (PPD)*”.

# Accepted Beamtimes

- *XAS investigation of DNA hybridization dynamics in situ*  
BACH beamline at Elettra Sincrotrone Trieste.  
Area Science Park, Basovizza S.S. 14 Km 163.5, 34149 Trieste, Italy.  
September, 2016.
- *Functionalization of suspended graphene NEMS*  
BACH beamline at Elettra Sincrotrone Trieste.  
Area Science Park, Basovizza S.S. 14 Km 163.5, 34149 Trieste, Italy.  
June, 2015.
- *Suspended graphene on Nanospectroscopy: a preparatory study*  
NANOSPECTROSCOPY beamline at Elettra Sincrotrone Trieste.  
Area Science Park, Basovizza S.S. 14 Km 163.5, 34149 Trieste, Italy.  
April, 2015.

# List of publications

- ***Contamination-free suspended graphene structures by a Ti-based transfer method.***  
Matruglio, A., Nappini, S., Naumenko, D., Magnano, E., Bondino, F., Lazzarino, M., Dal Zilio, S. (2016) Carbon, 103, pp. 305-310.
- ***A novel approach in the free-electron laser diagnosis based on a pixelated phosphor detector.***  
Matruglio, A., Dal Zilio, S., Sergo, R., Mincigrucci, R., Svetina, C., Principi, E., Mahne, N., Raimondi, L., Turchet, A., Masciovecchio, C., Lazzarino, M., Caetero, G., Zangrando, M. (2016) Journal of Synchrotron Radiation, 23, pp. 29-34.
- ***Toward an integrated device for spatio-temporal superposition of FEL and laser pulses.***  
Mincigrucci, R., Matruglio, A., Calvi, A., Foglia, L., Principi, E., Simoncig, A., Bencivenga, F., Dallorto, S., Gessini, A., Kurdi, G., Olynick, D., Dhuey, S., Sergo, R., Lazzarino, M., Masciovecchio, C., Dal Zilio, S. (2016) Optics Letters, 41 (21), pp. 5090-5093.
- ***Graphene nanobubbles on TiO<sub>2</sub> for in-operando electron spectroscopy of liquid-phase chemistry.***  
Nappini, S., Matruglio, A., Naumenko, D., Dal Zilio, S., Bondino, F., Lazzarino, M., Magnano, E. (2017) Nanoscale. Article in press.